SEPTEMBER 2019

M.Sc. in Mechanical Engineering

CELAL NAZLI

REPUBLIC OF TURKEY
GAZİANTEP UNIVERSITY
GRADUATE SCHOOL OF NATURAL & APPLIED SCIENCES

COMPUTATIONAL STUDY OF GAS TURBINE BLADE LEADING EDGE INTERNAL COOLING USING EFFICIENT HEAT TRANSFER SURFACES

M.Sc. THESIS

IN

MECHANICAL ENGINEERING

BY

CELAL NAZLI

SEPTEMBER 2019

COMPUTATIONAL STUDY OF GAS TURBINE BLADE LEADING EDGE INTERNAL COOLING USING EFFICIENT HEAT TRANSFER SURFACES

M.Sc. Thesis

in

Mechanical Engineering

Gaziantep University

Supervisor

Asst. Prof. Dr. Fuat YILMAZ

Co- Supervisor

Assoc. Prof. Dr. Azize AKÇAYOĞLU

by

Celal NAZLI

September 2019

REPUBLIC OF TURKEY
GAZİANTEP UNIVERSITY
GRADUATE SCHOOL OF NATURAL & APPLIED SCIENCES
MECHANICAL ENGINEERING

Name of the Thesis: Computational Study of Gas Turbine Blade Leading Edge Internal Cooling Using Efficient Heat Transfer Surfaces

Name of the Student: Celal NAZLI

Exam Date: 06.09.2019

Approval of the Graduate School of Natural and Applied Sciences

Prof. Dr. A. Necmeddin YAZICI
Director

I certify that this thesis satisfies all the requirements as a thesis for the degree of Master of Science.

Prof. Dr. Melda ÇARPINLIOĞLU
Head of Department

This is to certify that we have read this thesis and that in our consensus opinion it is fully adequate, in scope and quality, as a thesis for the degree of Master of Science.

Asst. Prof. Dr. Fuat YILMAZ
Supervisor

Assoc. Prof. Dr. Azize AKÇAYOĞLU
Co-Supervisor

Examining Committee Members	Signature
Prof. Dr. M. Sait SÖYLEMEZ	....
Assoc. Prof. Dr. Kamil ARSLAN	....
Asst. Prof. Dr. Fuat YILMAZ	....

I hereby declare that all information in this document has been obtained and presented in accordance with academic rules and ethical conduct. I also declare that, as required by these rules and conduct, I have cited and referenced all material and results that are not original to this work.

Celal NAZLI

ABSTRACT

COMPUTATIONAL STUDY OF GAS TURBINE BLADE LEADING EDGE INTERNAL COOLING USING EFFICIENT HEAT TRANSFER SURFACES

NAZLI, Celal
M.Sc. in Mechanical Engineering
Supervisor: Asst. Prof. Dr. Fuat YILMAZ
Co-Supervisor: Assoc. Prof. Dr. Azize AKÇAYOĞLU
September 2019
105 pages

Gas turbine blades are one of the most critical components due to their exposure to high thermal and centrifugal loads. Today studies in this field are concentrated on the improvement of gas turbine performances in terms of higher power output. In the present numerical study, flow and heat transfer characteristics of 3-D triangular vortex generators (VGs) located in a triangular duct representing internal cooling channel of a gas turbine blade are investigated deeply to find the best VG type and the best streamwise and spanwise distances between the VGs and the duct base in the context of thermal and hydrodynamic properties. The investigated VG types are periodically located inside the triangular duct in either smooth or in alternating directions and they are oriented as CFU-CFU, CFD-CFD, CFU-CFD and CFD-CFU configurations. The flow Reynolds number is fixed to 20,000, and inlet and wall temperatures are fixed to 20°C and 1760°C, respectively. The rotation number is 0.488. According to the present numerical results, it is found that the best cooling performance for the leading edge of the gas turbine blades is obtained for the CFD-CFU configuration and for the streamwise distance between the VGs is equal to the 0.5 times to the VG length and the best spanwise distance between the VGs and the duct base is equal to 0.0222 and 0.222 times the VG length, for the CFD and CFU configurations, respectively.

Key Words: Triangular duct, Vortex generator, Gas turbine blade internal cooling.

ÖZET

VERİMLİ ISI AKTARIM YÜZEYLERİ KULLANARAK GAZ TÜRBİNİ KANADININ HÜCUM KENARININ İÇ SOĞUTMASININ HESAPLAMALI ÇALIŞMASI

NAZLI, Celal
Yüksek Lisans Tezi, Makine Mühendisliği
Danışman: Dr. Öğr. Üyesi Fuat YILMAZ
İkinci Danışman: Doç. Dr. Azize AKÇAYOĞLU
Eylül 2019
105 sayfa

Gaz türbin kanatları, çok yüksek ısıl ve merkezkaç kuvvetlere maruz kalmalarından dolayı, daha çok güç çıkışı ve performans elde etme kapsamında günümüzde üzerinde en çok durulan araştırma konularından biridir. Bu sayısal çalışmada bir gaz türbininin iç soğutma pasajı olarak modellenen bir üçgen kanalın yüzeylerine yerleştirilen 3-boyutlu kanatçıklar çevresinde meydana gelen akım ve ısıl alan etkileri ayrıntılı bir şekilde araştırışmış, en iyi kanatçık tipi, bu kanatçıklar arasında akım yönündeki en iyi uzaklık, ve kanatçıklar ile kanal tabanı arasındaki akıma dik yöndeki en iyi uzaklık parametreleri, optimum ısıl ve hidrolik performansın elde edilmesi kapsamında belirlenmiştir. Araştırılan kanatçık tipleri kanal içerisine CFU-CFU, CFD-CFD, CFU-CFD ve CFD-CFU olarak isimlendirilen değişik konfigürasyonlarda periyodik olarak yerleştirilmiştir. Araştırma, Reynolds sayısının 20,000, giriş ve yüzey sıcaklıklarının sırasıyla 20°C ve 1760°C ve dönme sayısının 0.488 değerleri için gerçekleştirilmiştir. Sonuç olarak en iyi soğutma performansının; CFD-CFU tipi kanatçık ile, kanatçıklar arasındaki akım yönündeki uzaklığın kanatçık boyunun yarısı olması durumunda ve kanatçıklar ile kanalın tabanı arasındaki akıma dik yöndeki mesafenin CFD tipi kanatçık için kanatçık uzunluğunun 0.0222 katı, CFU tipi kanatçık için kanatçık uzunluğunun 0.22 katı koşullarında sağlandığı belirlenmiştir.

Anahtar Kelimeler: Üçgen kanal, Kanatçık, Gaz türbin kanatlarının iç soğutma pasajı.

To My Father and My Maternal Grandmother

ACKNOWLEDGEMENTS

First of all, I would like to express my deepest gratitude to my thesis co-supervisor, Assoc. Prof. Dr. Azize AKÇAYOĞLU, for her guidance, continual encouragement, endless support, invaluable understanding and patience throughout the study.

I would like to express my most sincere gratitude to Asst. Prof. Dr. Fuat YILMAZ, who introduced me to the subject of Computational Fluid Dynamics. His constructive comments, criticism, invaluable remarks, and expertise have greatly contributed to this study. I would like to thank him for his helping me to develop new insights in my study.

At the beginning of my thesis, I know a debt to Halil CEBECİ who transfers his knowledge of Computational Fluid Dynamics without any self-interest. Thanks to her knowledge and friendship was able to grasp my thesis more easily.

My mother, who has always been with me since I was born. She is the owner of my whole career and thesis. I thank her so much for everything she did.

I would like to thank my wife Bahar NAZLI, who convinced me that I could achieve this job when I was the most desperate.

This thesis has been performed in Mersin and Gaziantep Universities and is financially sponsored by the Scientific and Technological Council of Turkey (TUBITAK) under the project number of 111M726.

TABLE OF CONTENTS

LIST OF TABLES

Page

LIST OF FIGURES

Page

LIST OF ABREVIATIONS

3-D	Three dimensional
A	Area
AR	Aspect ratios
Bu	Buoyancy number
CAD	Computer aided drawing
CFD	Computational fluid dynamics
CFD-CFD	Common flow down to common flow down
CFD-CFU	Respectively common flow down to common flow up
CFU-CFU	Common flow up to common flow up
CFU-CFD	Respectively common flow up to common flow down
D	Hydraulic diameter
DES	Detached Eddy Simulation
d/Lw	Ratio of distance of winglet to length of winglet
EWT	Enhanced wall treatment
f	Friction factor
h	Convective heat transfer coefficient
Hw	Height of vortex generator
k	Thermal conductivity
k	Kinetic energy

L	Length
LDV	Laser doppler velocimetry
Lw	Length of winglet
Nu	Nusselt number
p	Pressure
Re	Reynolds number
Ro	Rotational number
Pr	Prandtl number
RNG	Renormalization group
SWF	Standard wall function
T	Temperature
THP	Thermal hydraulic performance
TKE	Turbulence kinetic energy
TLC	Thermochromics liquid crystal
TPF	Thermal performance factors
VG	Vortex generator

LIST OF SYMBOLS

$\boldsymbol{C}$	Circulation
$\boldsymbol{D_\omega}$	Diffusion modification constant
$\boldsymbol{\widetilde{G}_k}$	Production of turbulence kinetic energy
$\boldsymbol{\varepsilon}$	Dissipation rate
$\dot{\boldsymbol{m}}$	Mass average flow rate
$\boldsymbol{\eta}$	Shear rate
$\boldsymbol{\Gamma}$	Diffusivity
$\mathbf{u}$	Velocity
$\vec{\boldsymbol{V}}$	Instantaneous velocity vector
$\vec{\boldsymbol{w}}$	Vorticity
$\boldsymbol{\tau_w}$	Wall shear stress
$\boldsymbol{\mu}$	Viscosity
$\boldsymbol{\phi}$	Scalar variables

CHAPTER 1

INTRODUCTION

High energy prices and the energy crises that have been experienced in the past cause to government support for energy efficiency and energy saving works. Therefore; industrial and academic works concentrate to energy efficiency and high performance heat transfer devicesin that reason researchers intensely investigate geometrical optimization, using winglets or ribs and material enhancement.

A gas turbine is an internal combustion engine that uses air as the working fluid, in which chemical energy is extracted from the fuel and is converted into mechanical work on the rotating shaft after expanding in the turbine blades, to drive the engine and propeller, which, in turn, propel the airplane. The process of expansion of the gas in the turbine blades involves several stages. Each stage of the turbine consists of a row of stationary vanes followed by a row of rotating blades. A modern gas turbine rotor blade consists of complex air cooling passages (Figure 1.1) to avoid hot spots and maintain the material temperatures at the sustainable levels since turbine inlet temperature has already been far beyond the material acceptable level. Figure 1.1 illustrates the arrangements and leading and trailing edges of cooling channels, in a modern turbine rotor blade. The coordinate system, direction and center of rotation, cooling air entrance, angular velocity, etc. are also shown in this figure. As shown in the Figure 1.1, the cooling channels contain repeated ribs. Nowadays, generally triangular channel is preferred, that used for heat and mass transfer application in electronic, mechanic, biomechanical, nuclear, marine, aerospace and space, to suitable and effective features. Triangular channel is more efficient to other types of channel for easily produced and have high mechanical strength etc. properties. The best convective heat transfer obtains in equilateral triangle channels.

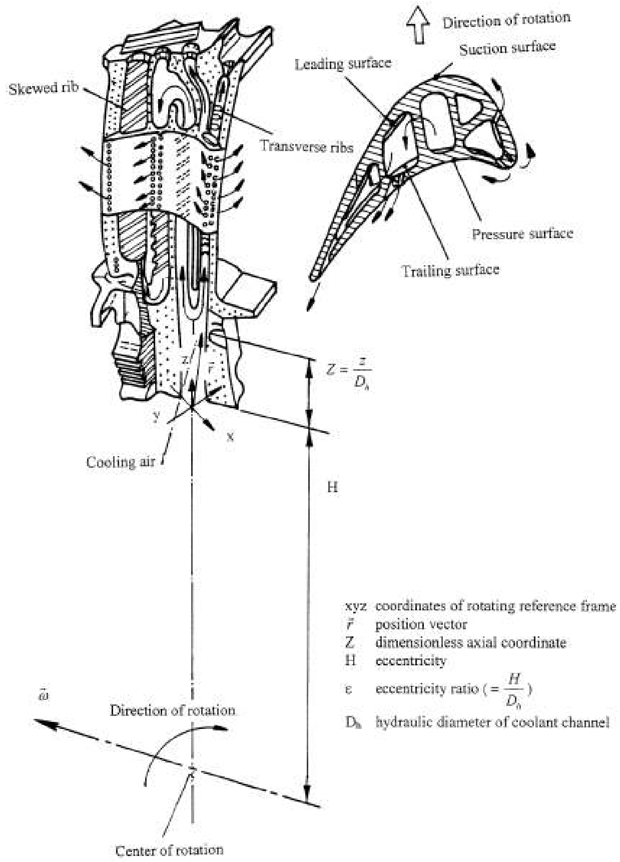

Figure 1.1 Modern gas turbine rotor blade cooling channel network [1].

The internal cooling channels generally take various shapes from the trapezoidal/triangular section at the leading edge; the square, rectangular and parallelogram section in mid-chord region to the narrow triangular section in the trailing edge. The leading edge area of gas turbine blade (Figure 1.2) has a higher heat and mechanical loads as it is exposed to high rotor inlet temperatures. Today's advanced gas turbines involve higher and higher rotor inlet temperatures and this temperature is far higher than the melting point (approximately 1700 °C) of the blade material. Therefore, turbine blades have to be efficiently cooled since the allowable metal temperature is much less than the hot gas temperature. For effective cooling the turbine blades, it is very common to introduce extended surfaces into the internal cooling channels and/or forcing a coolant externally (film and jet injection cooling) through a number of passages of constant cross section. Extended surfaces include ribs, pin-fins, dimples and protrusions -known as the turbulence promoters or turbulators- used to increase the internal heat transfer. Turbulence promoters are usually located by a repeated manner for disturbing the boundary layer periodically and introducing a secondary flow to achieve a good fluid mixing, a high turbulence level and an enhanced heat transfer. Also, rotation causes a further heat transfer enhancement.

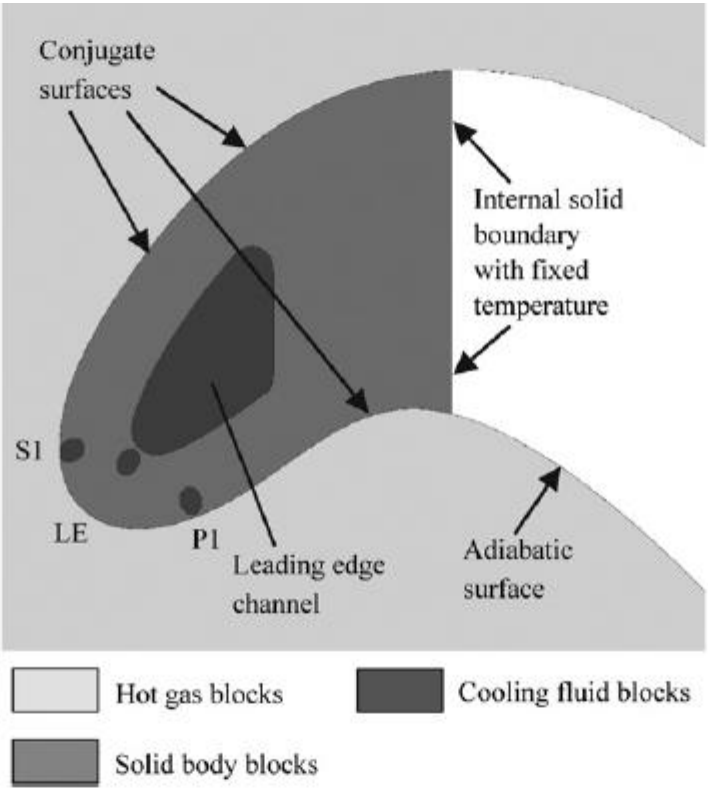

Figure 1.2 Illustration of the turbine blade leading edge [2].

Geometrical parameters of the extended surfaces are very important in terms of design, pressure drop, heat transfer and financial considerations. The most important geometrical parameters include height, pitch, angle, shape, arrangement, spacing, location and aspect ratio of the extended surfaces. The simple channel illustration can be seen in Figure 1.3. Channel shapes, lengths, aspect ratios, surface roughness and flow parameters such as Reynolds number, inlet temperature and rotation number are very important in this context.

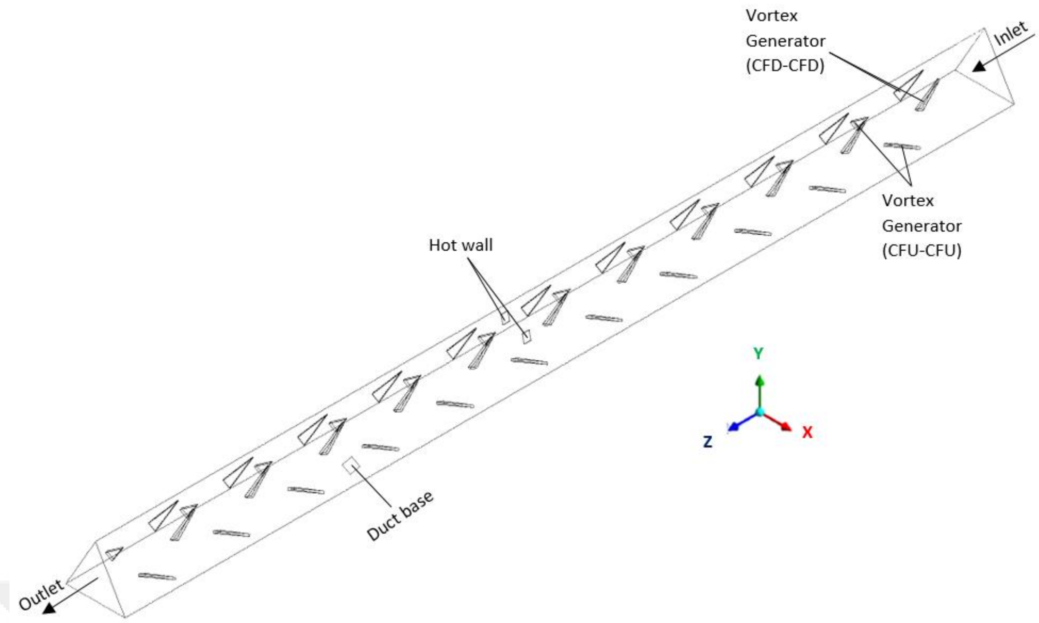

Figure 1.3 The single triangular channel with built-in delta-winglet [3].

In the gas turbine blade cooling applications, Re number and rotation number ranges from 10^4 to $2x10^5$ and 0.1 to 2, respectively. The inlet temperature is restricted by the metallurgical limit of the turbine blades. In this thesis, Re number is fixed to 20.000, inlet temperature and wall temperature are fixed to 20°C and 1760°C, respectively and the Rotation number is fixed to Ro=0.488 (400 rpm) to investigate deeply the effects of the geometrical parameters on the cooling performance as well as the pressure drop inside the channel.

In the literature, different channel geometries and vortex generators (VGs) are considered to obtain maximum heat transfer mechanism. For this purpose, different types of VGs using literature review are seen in Figure 1.4. Therefore, delta winglet type and rectangular wing type vortex generators (VGs) are compared with each other and researchers found that delta winglet type VGs have better characteristics in terms of effective cooling than rectangular VGs [4]. In this study, a pair of delta type VGs are placed on lateral surfaces of the triangular channel like in seen Figure 1.3.

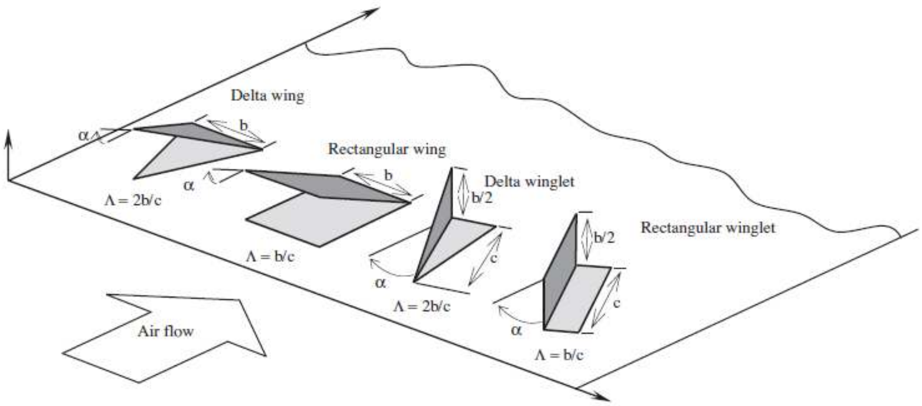

Figure 1.4 Vortex generators types, respectively delta wing, rectangular wing, delta-winglet and rectangular winglet types vortex generators [5].

CHAPTER 2

LITERATURE REVIEW

2.1 Introduction

Non-circular cross sectional channel are often preferred in industrial applications where limitations in size and volume required because of occurs turbulence and effective convections [6]. The triangular channels have larger specific surface areas and reduce the thermal resistance by reducing the film thickness of the fluid passing through them due to the sharp edges, creating the meniscus effect; in this way, can improved the heat transfer [7]. According to Gupta et al, triangular cross-section channels have superior heat transfer performance compared to circular, semi-circular and square section channels [8]. In the case of triangular section, the best convection heat transfer and high Nusselt number can be obtained equilateral triangular channel, in other words if the peak angle of the isosceles triangle is 60° [9-11].

Heating / cooling of non-circular channels is possible by various techniques. These techniques include the creation of electric or magnetic fields, film cooling, addition of machined / rough / expanded surfaces to walls. A number of researchers have stated that heat transfer can be improved very successfully by a passive method by creating irregularity, instability, turbulence, loop, vortex in the flow area [12, 13]. With this passive methods, structures that disrupt the flow, such as winglets, protrusions and obstructions, can be mounted on heat transfer surfaces by creating vortices which will positively affect the heat transfer in the flow area. These structures, which are called vortex producers, can be composed of rectangular, square, circular or triangular fin or fins. Vortex generators (VGs) are structures that are capable of creating latitudinal and longitudinal vortices. Latitudinal vortices are perpendicular to the direction of flow, occurs two dimensional flow structures. However, longitudinal vortices are same direction with flow, occurs three dimensional flow structures [14]. The longitudinal vortex generators can produce a continuous irregularity in the viscous sub-layer and can substantially increase the heat transfer [15]. Wang et al, Jacobi and Shah was examined in-depth investigation review of the literature [16, 17]. Research has shown that triangular winglets can provide more efficient heat transfer in a specific area by creating longitudinal vortices [14, 18].

2.2 Numerical Studies

Ahn et al. performed an LES simulation to predict the internal cooling passage of a rotating internally ribbed turbine blade for Re=30,000 and for rotation numbers of 0, 0.1 and 0.3. The rib pitch and height was equal to 10 and 0.1 times the channel height, respectively. Authors compared the smooth and ribbed channel and found that ribs induced strong wall-normal motions resulting from the vortex shedding from the ribs and thus the heat transfer is augmented on the trailing wall side [19].

Aroon et al. presented their numerical study results of detached eddy simulation (DES) for a stationary duct with square ribs aligned normal to the main flow direction for Re=20,000. The rib height to channel hydraulic diameter ratio was 0.1 and the rib pitch to rib height ratio was 10. Their conclusion was concentrated on the ability to predict flow and heat transfer with DES and they obtained good quantitative results for the flow which was dominated by separation and reattachment of shear layers, unsteady vortex induced secondary motions, and strong streamline curvature [20].

Aroon et al. performed DES simulations to capture the turbulent energy in the resolved scales in a rotating duct with square ribs aligned normal to the main flow direction for Re=20,000. The tested three rotation numbers were Ro = 0.18, 0.35 and 0.67. The rib height to channel hydraulic diameter ratio was 0.1 and the rib pitch to rib height ratio was number of 10. They concluded that DES showed much better fidelity in calculating critical components of the turbulent flow field and heat transfer than URANS [21].

Dhanasekaran et al. studied numerically the concept of injection of mist to the coolant fluid in a two-pass internal cooling passage comprised of rectangular rotating channel with 45° angled rib turbulators. With 2% mist injection, they obtained 30% and about 20% cooling enhancement at the trailing and at the leading surface of the first passage, respectively. The predicted 20% enhancement in the second passage for both the surfaces [22].

Promvonge et al. conducted a numerical work to examine turbulent periodic flow and heat transfer in a square-duct with inline 60° V-shaped discrete ribs placed on two opposite heated walls representing internal duct of a gas turbine cooling passage. They investigated effects of different rib height to duct diameter ratios, on thermal characteristics for the Reynolds numbers ranging from10,000 to 25,000. Based on their conclusion, a pair of counter-rotating vortices caused by the rib can induce impingement/attachment flows on the walls leading to greater increase in heat transfer. They found a maximum thermal performance around 1.8 for the rib height to duct diameter ratio of 0.0725 [23].

Wang et al. determined 3-D flow and heat transfer characteristics in rotating two-pass channels with 45° ribbed walls under stationary and rotating conditions using ANSYS CFX solver with Reynolds stress turbulence model. The investigated rotation numbers were 0 and 0.24 and Reynolds number was 25,000. They concluded that skewed ribs and 180° sharp turn created a very complex secondary flow pattern leading to strong anisotropic turbulence and high level of anisotropy of Reynolds stresses, which have a significant impact on the local heat transfer coefficient distributions [4].

Xie et al. determined influences of 6 kinds of guide ribs/vanes on enhanced heat transfer of a turbine blade tip-wall for Re between 100,000 and 600,000 using FLUENT software. They suggested that that the usage of proper guide ribs/vanes is a suitable way to augment the blade tip heat transfer and to improve the flow structure, but is not the most effective way compared to the augmentation by surface modifications imposed on the tip-wall directly [24].

Xie et al. determined flow structure and heat transfer in a square passage with six different types of offset mid-truncated ribs for the Re ranging from 10,000 to 50,000 using FLUENT solver. According to the their results, staggered arrangement for 90° mid-truncated ribs can enhance heat transfer efficiently and makes a good overall performance at low Reynolds numbers and they selected the best case that can be used in practical operation because of reduced weight and good thermal performance at high Reynolds numbers [25].

2.3 Experimental Studies

Amro et al. used a transient liquid crystal method to measure the heat transfer for cooling the first stage of turbine blades. The channel was in rounded triangular shape included 3D rectangular ribs. Re number was between 50,000-200,000. They found that 60° ribs provide higher heat transfer enhancements than 45° ribs but 3D rib with 45° angle and a double-sided fully overlapped ribs in the arc area was the best promising rib arrangement for the leading edge cooling in terms of friction factor considerations [26].

Armellini et al. made a 2D and Stereo-PIV measurements in a wedge-shaped gas turbine exit channel portion for Re=20,000 and a rotation number of Ro=0 and 0.23 to investigate the rotational effects inside the cooling channel and have seen that rotational effects altered mainly the heat transfer field at the exit of the channel portion [27].

Chang et al. measured local heat transfer for a radially rotating rectangular channel fitted with staggered V-shaped ribs for Re number between 10,000-24,000. Rotation number was between 0 and 1. The authors was the first to examine the heat transfer performances for a compound surface roughness of 2.8–5 and 5–7.8 times of the Dittus–Boelter values in the rotating channel with cooling applications to gas turbine rotor blades [28].

Chang et al. performed an experimental study to investigate heat transfer enhancement and pressure drop by skewed wavy sidewall for two-pass ribbed channels with different aspect ratios. The ribs were in 45° in-line arrangement and the channel aspect ratio was 0.5, 1 and 2. Reynolds number was between 5,000 and 20,000. They compared their study with the Dittus–Boelter references and found that the Nusselt number and the accompanying friction factor was considerably raised [29].

Chang et al. compared thermal performances of radially rotating ribbed parallelogram channels with and without dimples by employing an experimental work between 5,000 $\leq$ Re $\leq$ 15,000, 0 $\leq$ Ro (Rotation number) $\leq$ 0.3 and 0 $\leq$ Bu (Buoyancy number) $\leq$ 0.23. The minimum penalty of pressure drop with an amplified heat transfer enhancement was analysed in detail from dimpled and un-dimpled rib floor, rib and midrib location, influence of rotation, rotating buoyancy and the geometric features points of view [30].

Chang et al. measured Nusselt number distributions, pressure drop coefficients and overall thermal performance factors (TPF) by infrared thermography method in a rotating parallelogram channel fitted with ribbed walls. The Reynolds number, rotation number and Buoyancy number ranges were $5,000 \leq Re \leq 15,000$, $0 \leq Ro \leq 0.3$ and $0.001 \leq Bu \leq 0.23$. The authors examined Bu effects on Nu and rib locations and generated a set of empirical Nu correlations [31].

Choi et al. used the transient liquid crystal technique to measure heat transfer coefficient distribution in a channel containing both angled ribs and sand dimples for a Reynolds number of 50,000. The rib pitch, rib angle, dimple diameter, and dimple center-to-center distance were 6 mm, 60°, 6 mm, and 7.2 mm, respectively. The channel aspect ratio was 2 and 4. Based on their measurements, they concluded that the compound cooling technique with angled ribs and sand dimples should be considered as a candidate for the design of gas turbine blade internal cooling channels to improve the heat transfer performance [32].

Chyu et al. determined the local bulk mean temperature and the sensible local heat transfer coefficient using the thermochromics liquid crystal (TLC) thermography technique in the turbine blade cooling passage comprised of delta wing shaped repeated vortex generators. They found that the magnitude of heat transfer coefficient may differ as much as 40%, depending on the method of evaluation and choice of reference temperature [33].

Davide Lengani et al. presented results of their experimental study performed with Laser Doppler Velocimetry (LDV) on vortex generators used to control the turbulent boundary layer separation used in turbine intermediate ducts. They located one pressure loss core at the vortex center and another one close to the plate surface and then compared their results on controlled and uncontrolled boundary layer basis. They observed a steep pressure loss increase where the flow was detached for the uncontrolled condition. They also found a strong reduction in the aerodynamic losses when the boundary layer control was applied. Losses for the controlled condition were reduced by 50% with respect to the uncontrolled condition [34].

Gupta et al. measured Local heat transfer distribution in a square channel with 3 different rib profiles including 90° continuous, 90° saw tooth profiled and 60° broken for Re between 10,000≤ Re ≤30,000. They found that 60° broken ribs caused higher heat transfer enhancement than 90° continuous ribs and 90° continuous, 90° saw tooth profiled showed the same enhancement [35].

Chang et al. used infrared thermography method to measure the pressure drop coefficients and Nusselt number (Nu) distributions of a rotating channel fitted with inclined rectangular slender pin–fins through leading and trailing end-walls roughened by skewed ribs with radially outward flow for the conditions of 5,000≤Re≤15,000, 0≤Ro≤0.4 and 0.0007≤Bu≤0.31. They reported different heat transfer augmentations and pressure drop reductions obtained for the configurations studied [36].

Lawson et al. conducted an experimental study and used low aspect ratio pin fins for a range of Reynolds numbers between 5,000 and 30,000. They determined the effects of pin spacing on heat transfer and pressure loss through pin fin arrays. According to the results they obtained, spanwise pin spacing had a larger effect than streamwise spacing on array pressure loss while streamwise spacing had a larger effect than spanwise spacing on array heat transfer [37].

Liou et al. investigated experimentally to show influence of channel aspect ratio on heat transfer in rotating rectangular ducts with skewed ribs. The rectangular ducts were roughened by 45° staggered ribs with channel aspect ratios (AR) of 1:1, 2:1 and 4:1. Reynolds (Re), rotation (Ro) and buoyancy (Bu) number ranges were in the ranges of 5,000–30,000, 0–2, and 0.005–8.879, respectively. They found that Nu/Nu_0 ratios in the rotating channels of AR = 1, 2, and 4 fall in the ranges of 0.6–2.2, 0.5–2.7, and 0.5–2.1, respectively [38].

Liu et al. determined heat transfer characteristics in steam-cooled rectangular channels with two opposite rib-roughened walls for Re in the range of 10,000-80,000 experimentally. The pitch-to-rib height ratio was 10 and the channel length was 1000 mm. They tested 3 channel aspect ratios of 0.25, 0.5 and 1. They found that the average Nusselt number for the channel with α=45° was about 15-25% higher than that for the channel with α=30°[39].

2.4 Vortex Generators

Plain triangular passages are one of the most common fin configurations used in plate heat exchangers, gas turbines, electronics cooling, automotive radiators and intercoolers, nuclear reactors, solar receivers, etc. to obtain the lowest energy consumption. To achieve a better thermo-hydraulic performance, longitudinal VGs are widely used in order to increase the efficiency, to reduce the weight, cost, fuel consumption and to protect the environment. Longitudinal VGs are superior to disturb the viscous sub-layer and to thin the thermal boundary layer along the main flow direction continuously. Inside a duct channel, vortices can be generated by flow separation that makes the fluid rotate continuously around their rotation axis. This phenomenon can be used to enhance convective heat transfer as indicated by Ferrouillat et al [14]. Huisseune et al. highlighted that VG geometry had a significant contribution to the heat transfer enhancement at lower inlet velocities [40]. Joardar and Jacobi performed wind tunnel experiments and found that VGs provided an improved thermal-hydraulic performance in compact heat exchangers for automotive systems [41, 42]. They also indicated that the relationships between vortex flow, heat transfer enhancement, and sensible heat ratio are not very well understood and recommended further works to be done in this area. Fiebig indicated that heat transfer is strongly influenced by the interaction of the vortices created by the winglets and winglets cause higher heat transfer enhancement than wings [43]. Sanders and Thole [34] placed VGs on the louvers of a compact heat exchanger and found that both heat transfer and friction factor augmented as the Re was increased with an alternating direction of VGs were used [44]. A larger vortex formation area and a greater induced vorticity field between vortex pairs are observed when VGs are located with alternating direction in a triangular heat exchanger channel, compared with VGs were located in the same direction [45]. In this study author stated that it is expected to obtain better heat transfer characteristics when VGs are located with alternating direction.

Above literature survey reveals that there exists some conflict between the investigators in terms of geometrical parameters and the VG types used to improve the performance of the systems under consideration. Some of the investigators found completely different results from their experimental and/or numerical studies.

Therefore, in this thesis the geometrical parameters and the VG types are investigated in detail to find the best cooling performance that can be obtained from the gas turbine blade leading edge cooling applications.

Vortex generators can be placed the flow area in two different ways. These are "Common Flow Up (CFU)" and "Common Flow Down (CFD)" can be shown as Figure 2.1. Torii et al , Allison and Dally are compared the two winglet pairs with each other and the result of the CFU is the better in terms of heat transfer properties [46, 47]. However, Kim and Yang and Biswas et al. found that CFD has better heat transfer performance. In these study, CFU or CFD configurations and CFU-CFD or CFD-CFU configurations are examined for obtaining effective heat transfer, respectively [15, 48].

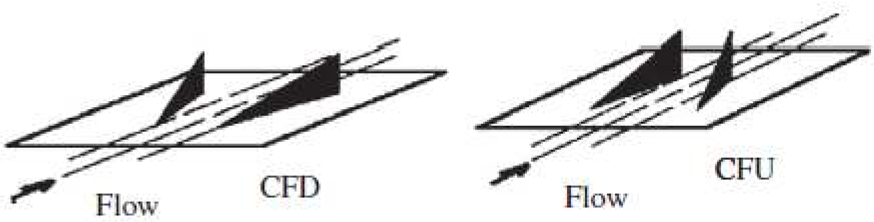

Figure 2.1 "Common Flow Up-CFU" and "Common Flow Down-CFD" configurations.

There are number of experimental and numerical studies have been performed to achieve the best geometry of the extended surfaces for the leading-edge internal cooling of gas turbines. In these studies, the influences of angles, heights, arrangements, and spacing between the extended surfaces have been investigated as indicated in the above numerical and experimental studies.

The difference of this thesis from other studies; To investigate which CFU and CFD vortex generators are better and to examine which of the different views is correct. Also understand whether CFU and CFD type vortex producers are combined using more or less effective than single type used vortex generators. In thesis, examined characteristic of heat transfer enhancement of gas turbine blade leading edge internal cooling used by equilateral triangular channel with delta type vortex generators.

CHAPTER 3

MATERIAL AND METHODS

3.1 Streamline

A streamline is a path traced out by a massless particle as it moves with the flow, in other words; Streamlines are a family of curves that are instantaneously tangent to the velocity vector of the flow. These show the direction a fluid element will travel in at any point in time. Formula is given that;

$$\vec{V} \; x \; d\vec{S} = 0 \tag{3.1}$$

In equation 3.1; $d\vec{S}$ is the length of an infinitesimal small line segment along a streamline at a point, $\vec{V}$ is the instantaneous velocity vector. Three-dimensional fluid flow in seen Figure 3.1.

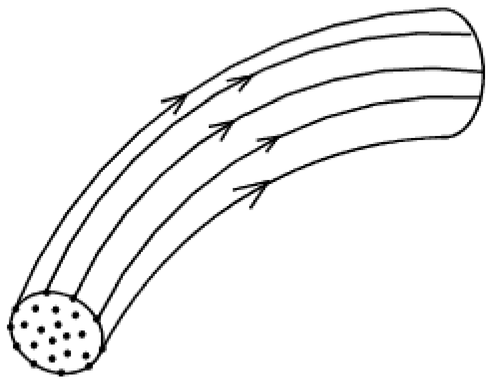

Figure 3.1 Three dimensional flow of fluids [49].

3.2 Vorticity

Vorticity is a kinematic property of fluid particle that angular velocity. It is a vector quantity, having three scalar components. Vorticity symbol is w, it is defined by;

$$\vec{w} = \nabla \; x \; \vec{V} \tag{3.2}$$

$$\vec{w} = i_x\left(\frac{\partial w}{\partial y} - \frac{\partial v}{\partial z}\right) + i_y\left(\frac{\partial u}{\partial z} - \frac{\partial w}{\partial x}\right) + i_z\left(\frac{\partial v}{\partial x} - \frac{\partial u}{\partial y}\right) \tag{3.3}$$

$$\vec{w} = i_r\left(\frac{1}{r}\frac{\partial V_z}{\partial \theta} - \frac{\partial V_\theta}{\partial z}\right) + i_\theta\left(\frac{\partial V_r}{\partial z} - \frac{\partial V_z}{\partial r}\right) + i_z\left(\frac{1}{r}\frac{\partial}{\partial r}(rV_\theta) - \frac{1}{r}\frac{\partial V_r}{\partial \theta}\right) \tag{3.4}$$

In equation 3.3 and equation 3.4 express the vorticity w in Cartesian and Cylindrical coordinates, respectively [50].

3.3 Boundary Layer Vorticity

In the viscous boundary layer that develops next to a solid wall past which fluid flows, vorticity is created by an unbalanced viscous force that rotates the fluid particles. The amount of vorticity at the wall, w , can be related to the magnitude of the wall shear stress τ_w by noting that, if x is the stream direction and y the normal direction at the wall, then by equation 3.3:

$$w = i_z\left(-\frac{\partial u}{\partial y}\right) = -\frac{\tau_w}{\mu} i_z \tag{3.5}$$

3.4 Circulation

The circulation around C is the integration of the tangential velocity around C.

$$\Gamma = \oint u\,.\,dl \tag{3.6}$$

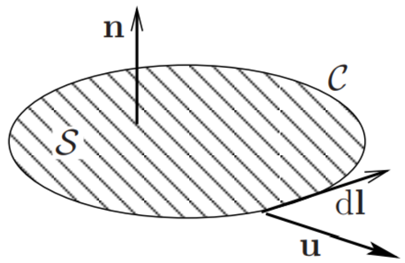

Figure 3.2 Circulation schematics.

By Stokes theorem, for any surface S spanning the curve C,

$$\Gamma = \oint_C u\,.\,dl = \int_S (\nabla\ x\, u)\,.\,n\, dS = \int_S w\,.\,n\, dS \tag{3.7}$$

So, the circulation around C is equal to the vorticity flux through the surface S: it is the strength of the vortex tube. Vortices examples are seen following Figure 3.3-Figure 3.4.

Figure 3.3 Bath-plug vortex, Vortices behind aeroplanes, horse vortex, respectively.

Bath-plug vortex is the shape of the free surface of water can be modelled using the Rankin vortex. Aero planes behind vortices decay very slowly and are a danger for small aircraft flying behind large ones. Horse vortex results in a downwards flow behind chimneys etc.

Figure 3.4 Vortex rings, von Karman vortex street, respectively

Smoke rings and underwater bubble rings are examples of vortex rings, a flow past an obstacle (e.g. a cylinder) produces a series of line vortices [51].

3.5 Phase Plane Analysis

A graphical method described by equations of the type;

$$\frac{dx}{dt} = P\ (x, y) \tag{3.8}$$

$$\frac{dy}{dt} = Q\ (x, y) \tag{3.9}$$

Where y and x are state variables, *P(x, y)* and *Q(x, y)* are the function which satisfy the conditions, and t is time-independent perimeters. The behavior of such a system may be represented geometrically in a plane in rectangular Cartesian coordinates. The plane Oxy is called the phase plane. Some phase trajectories in the neighborhood example in seen Figure 3.5 [52].

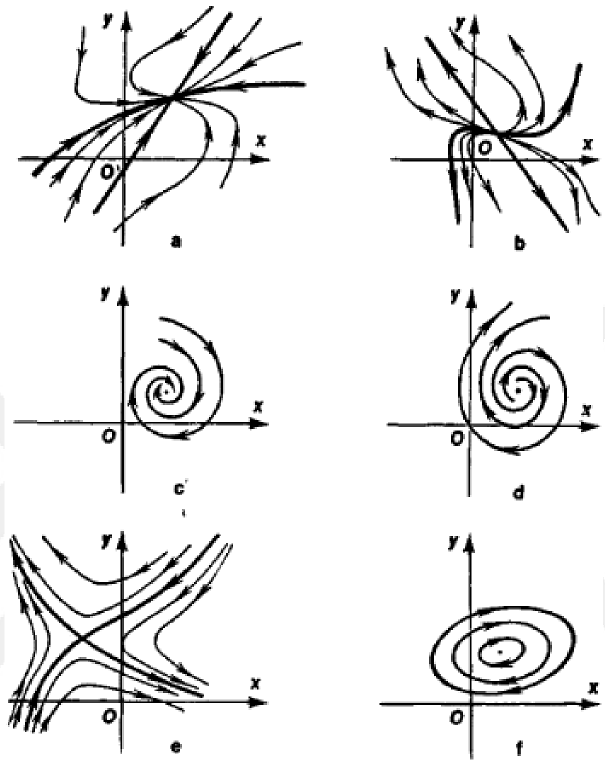

Figure 3.5 Phase trajectories in the neighborhood of the following types of singular points: (a) a stable node, (b) an unstable node, (c) a stable focus, (d) an unstable focus, (e) a saddle point, (f) a center computational

3.6 Introduction to Analysis

Computational Fluid Dynamics are used to solve system in this study. According to the literature review, the most effective heat transfer properties occur when the channel cross-section is equilateral triangular. The delta-winglets are located in different configurations to the triangular channel to constriction/expand the flow. The optimization studies were carried out with respect to the dimensions, numbers and positions within the channel placed on the inclined surfaces of the triangular channel. Drawing of geometric models was done by SOLID WORKS computer aided drawing program. The meshes of the models was created with ANSYS MESH PLATFORM. ANSYS FLUENT (V.14.5) solvent under ANSYS CFD package was used for numerical analysis.

Determination of the mesh structure, wall function and numerical model that best performs to the experiment; velocity vectors, velocity profiles, vortex distributions, flow lines distribution and turbulence statistics were obtained in various sections of triangular channel. Within the best of the results obtained, the flow field-heat transfer relations in the triangular channel were investigated extensively and the resulting from the interaction of these two properties were evaluated and the conditions under which the best thermo-hydraulic performance were realized. In this way, very useful information was obtained in the heat transfer enhancement.

The time averaged turbulence models and transition models are used in this study are listed below:

- Standard k- ε Model
- RNG k- ε Model
- Realizable k- ε Model
- Standard k- ω Model
- SST k- ω Model

3.7 Time Averaged Models

The time (Reynolds) average (RANS- Reynolds Averaged Navier Stokes) can be defined as using instantaneously flow characteristics to obtain flow features. In the Reynolds average process, the exact solution variables in the Navier-Stokes equations are decomposed into two components: mean (time average) and turbulence components. For velocity components;

$$u_i = \bar{u}_i + u'_i \qquad (3.10)$$

Where $\bar{u}_i$ and u'_i averaged and turbulence velocity components (i=1, 2, 3).

For other scalar variables, such as pressure and energy, the same expression applies:

$$\phi = \overline{\phi} + \phi' \qquad (3.11)$$

In there, ϕ represents scalar magnitudes such as pressure, energy etc. If these expressions are inserted into the continuity and momentum equations, evaluated time averaged the Reynolds averaged continuity and momentum equations shown below are obtained;

$$\frac{\partial \rho u_i}{\partial x_i} = 0 \tag{3.12}$$

$$\frac{\partial}{\partial x_j}\left(\rho u_\iota u_j\right) = -\frac{\partial p}{\partial x_i} + \frac{\partial}{\partial x_j}\left[\mu\left(\frac{\partial u_i}{\partial x_j} + \frac{\partial u_j}{\partial x_i} - \frac{2}{3}\delta_{ij}\frac{\partial u_i}{\partial x_i}\right)\right] + \frac{\partial}{\partial x_j}\left(\rho\overline{u'_\iota u'_j}\right) \tag{3.13}$$

In these equations, u_i is the velocity components, $(\rho\overline{u_\iota' u_j'})$ is turbulence stresses. Turbulence models are used to calculate the turbulence stresses arising from the time-average process and the momentum equation, and to bring the system of equations into a closed (soluble) form. Obtaining the closed equation system can be performed in two different ways. One of them is Eddy Viscosity (Boussinesq Hypothesis) model and the other is Reynols Stress model. Boussinesq Hypothesis Spalart-Allmaras model is used in k-ε models and k-ω models, while the Reynols Stress model is used in Reynolds Stress Models. In Eddy viscosity models, turbulence stresses are modeled by calculating the Eddy (turbulence) viscosity (μ_t) and using the following equation.

$$-\rho\overline{u'_\iota u'_J} = \mu_t\left(\frac{\partial u_i}{\partial x_j} + \frac{\partial u_j}{\partial x_i}\right) - \frac{2}{3}\left(\rho k + \mu_t\frac{\partial u_k}{\partial x_k}\right)\delta_{ij} \tag{3.14}$$

Turbulence kinetic energy is the help of the find turbulence dissipation rate and specific dissipation rate expressions, μ_t is calculated by using the turbulence time scale (or speed scale) and length scale. In each turbulence model μ_t calculates in a different way. These models are briefly mentioned below [53, 54].

3.7.1 Standard k-ε Turbulence Model

It is a semi-empirical model which is widely used and having acceptable accuracy in terms of economics and various flow models in between two-equation turbulence models. However, since the equation ε contains an unpredictable term in the wall, this model uses wall functions as in other k-ε models. In addition, it is not a successful model in the case of large pressure gradients and large discharges. The turbulence involves the solution of the two transport equations for kinetic energy (k) and dissipation rate (ε) and the calculation of turbulence viscosity. When the forces of lifting are neglected, these transport equations are respectively in order for k and ε;

$$\boldsymbol{\rho}\frac{D\,k}{D\,t} = \frac{\partial}{\partial x_i}\left(\Gamma_k \frac{\partial k}{\partial x_i}\right) + G_k - \rho\varepsilon \tag{3.15}$$

$$\rho\frac{D\,\varepsilon}{D\,t} = \frac{\partial}{\partial x_i}\left(\Gamma_\varepsilon \frac{\partial \varepsilon}{\partial x_i}\right) + C_{1\varepsilon}\frac{\varepsilon}{k}G_k - C_{2\varepsilon}\frac{\varepsilon^2}{k} - R \tag{3.16}$$

Diffusivity terms in this model can be written by

$$\Gamma_k = \mu + \mu_t \,/\, \sigma_k \quad, \Gamma_\varepsilon = \mu + \mu_t \,/\, \sigma_\varepsilon \tag{3.17}$$

and term for turbulence kinetic energy generation from velocity gradient is

$$G_k = \mu_t \left(\frac{\partial u_i}{\partial x_j} + \frac{\partial u_j}{\partial x_i}\right)\frac{\partial u_i}{\partial x_j} \tag{3.18}$$

where turbulence viscosity is calculated as follows.

$$\mu_t = \rho\, C_\mu \frac{k^2}{\varepsilon} \tag{3.19}$$

R= 0 in this models, other empirical constants; $C_{1\varepsilon}$ = 1.44, $C_{2\varepsilon}$ = 1.92, C_μ= 0.09, Prandtl numbers are σ_k= 1.0, σ_ε= 1.3 for *k* and ε [53, 54].

3.7.2 RNG (Renormalization group) k-ε Turbulence Model

The RNG k-ε turbulence model was considered by Yakhot and Orszag, and developed by Yakhot et al. for vortexed flows. It is a model with two equations and it is obtained by using renormalization group theory from Navier-Stokes equations [55], [56]. This model more suitable than Standard k-ε Turbulence Model for complex flow, high rate vortex flow and diverge flows. That model has same k and ε equations with Standard k-ε Turbulence Model. Main differences are related using of different constants and additional terms. The terms diffusivity in the RNG k-ε turbulence model is given as

$$\Gamma_k = \mu_e\, \alpha_k \quad, \Gamma_\varepsilon = \mu_e\, \alpha_e \tag{3.20}$$

The effective viscosity is expressed in the form of the sum of the fluid viscosity and turbulence viscosity;

$$\mu_e = \mu + \mu_t \tag{3.21}$$

It is obtained from the solution of the following ordinary differential equation.

$$d\left(\frac{\rho^2 k}{\sqrt{\varepsilon\mu}}\right) = 1.72\frac{\mu_e/\mu}{\sqrt{(\mu_e/\mu)^3 - 1 + C_v}}\; d\,(\mu_e/\mu) \tag{3.22}$$

This equation also calculates the effects of low Re number. On the other hand, this equations limits are given same results of turbulence viscosity for equation 3.19 for high Re numbers.

In the RNG k-ε model, the additional term in the ε equation;

$$R = \frac{C_\mu \rho \eta^3 (1-\frac{\eta}{\eta_0})}{1+\beta\eta^3} \frac{\varepsilon^2}{k} \tag{3.23}$$

This additional term is important to consider the effects of high shear rates and streamline curvatures, which are not in the standard k-ε model. In cases where the shear rate is high (high η), the dissipation rate increases, thus reducing the turbulence viscosity and k value, which leads to less energy withdrawal. Thus, the size of the circulation zones is closer to the experimental data. These model constants are; $C_{1\varepsilon}$=1.42, $C_{2\varepsilon}$=1.68, C_v=100, η_0=4.38, β =0.012, C_μ=0.0845.

The α_k and α_ε parameters in Equation 3.20 show the inverse of the effective Prandtl numbers for k and ε, and are derived analytically from the RNG theory;

$$\frac{\mu}{\mu_k} = \left|\frac{\alpha-1.3929}{\alpha_k-1.3929}\right|^{0.6321} \left|\frac{\alpha-2.3929}{\alpha_k-2.3929}\right|^{0.3679} \tag{3.24}$$

is calculated from. Where α_0 = 1. In high Reynolds numbers (μ / μ_e <<1) $\alpha_k = \alpha_\varepsilon \cong 1.393$.

The RNG model permits to consider rotation and vortex effects by properly correcting the turbulence viscosity. For improved turbulence viscosity, given function is used (ANSYS FLUENT Help 2013).

$$\mu_t = \mu_{t0} f\left(\alpha_s, \Omega, \frac{k}{\varepsilon}\right) \tag{3.25}$$

Here, vortex constant can take different values according to the vortex number and the characteristic vortex number. For low-vortex flows, α_s = 0.05 is taken. However, high α_s values are used in strong vortices [53, 54].

3.7.3 Realizable k-ε Turbulence Model

This model is successful in flows involving rotation, reverse pressure gradients boundary layers and separation flows. In this model, the following transport equations are used.

$$\frac{\partial}{\partial t}(k\rho) + \frac{\partial}{\partial x_j}(k\rho u_j) = \frac{\partial}{\partial x_j}\left[\left(\mu + \frac{\mu_t}{\sigma_k}\right)\frac{\partial k}{\partial x_j}\right] + G_k + G_b + \rho\varepsilon - Y_M + S_k \quad (3.26)$$

$$\frac{\partial}{\partial t}(\varepsilon\rho) + \frac{\partial}{\partial x_j}(\varepsilon\rho u_j) = \frac{\partial}{\partial x_j}\left[\left(\mu + \frac{\mu_t}{\sigma_\varepsilon}\right)\frac{\partial \epsilon}{\partial x_j}\right] + \rho C_1 S_\varepsilon - \rho C_2 \frac{\varepsilon^2}{k + \sqrt{\varepsilon\nu}} +$$

$$C_{1\varepsilon}\frac{\varepsilon}{k}\, C_3 G_b + S_\varepsilon \quad (3.27)$$

where

$$C_1 = max\left[0.43, \frac{\eta}{\eta+5}\right], \eta = S\frac{k}{\varepsilon}, S = \sqrt{2S_{ij}S_{ij}} \quad (3.28)$$

The turbulence viscosity is calculated as in other k- ε models. The difference in other k- ε models is that $C\mu$ is not fixed, but is as follows:

$$C_\mu = \frac{1}{A_0 + A_S\frac{kU^*}{\varepsilon}} \quad (3.29)$$

where U^* is given as

$$U^* = \sqrt{S_{ij}S_{ij} + \tilde{\Omega}_{ij}\,\tilde{\Omega}_{ij}} \quad (3.30)$$

and

$$\tilde{\Omega}_{ij} = \Omega_{ij} - 2\varepsilon_{ijk}\omega_k \quad (3.31)$$

$$\Omega_{ij} = \overline{\Omega_{ij}} - \varepsilon_{ijk}\omega_k \quad (3.32)$$

Following terms are given in equation 3.29;

$$A_0 = 4.04, A_s = \sqrt{6} + cos\,\theta \quad (3.33)$$

The model constants in transport equations are;

$C_{1\varepsilon}$=1.44, C_2=1.9, σ_k= 1.0, σ_ε= 1.2 [53, 54]

3.7.4 Standard k-ω Turbulence Model

This model gives more accurate results especially in low Reynolds numbers. Since the model constants do not contain undefined values on the wall without any wall function, correct solutions can be obtained in boundary layer currents. Transport equations are solved using the following formulas;

$$\frac{\partial}{\partial t}(k\rho) + \frac{\partial}{\partial x_i}(k\rho u_i) = \frac{\partial}{\partial x_j}\left(\Gamma_k \frac{\partial k}{\partial x_j}\right) + G_k - Y_K + S_k \tag{3.34}$$

$$\frac{\partial}{\partial t}(k\omega) + \frac{\partial}{\partial x_i}(\omega\rho u_i) = \frac{\partial}{\partial x_j}\left(\Gamma_\omega \frac{\partial \omega}{\partial x_j}\right) + G_\omega - Y_\omega + S_\omega \tag{3.35}$$

The terms diffusivities are calculated as follows:

$$\Gamma_k = \mu + \frac{\mu_t}{\sigma_k} \quad , \Gamma_\omega = \mu + \frac{\mu_t}{\sigma_\omega} \tag{3.36}$$

The turbulence viscosity is calculated as follows:

$$\mu_t = \alpha^* \frac{\rho k}{\omega} \tag{3.37}$$

and

$$\alpha^* = \alpha_\infty^* \left(\frac{\alpha_0^* + Re_t/R_k}{1 + Re_t/R_k}\right) \tag{3.38}$$

$$Re_t = \frac{\rho k}{\mu\omega} \tag{3.39}$$

$$\alpha_0^* = \frac{\beta_i}{3} \tag{3.40}$$

Where $\beta_i = 0.072$ and $R_k = 6$. Model constants can be found in Fluent theory guide in 2013[53, 54].

3.7.5 Shear Stress Transport k-ω Turbulence Model

This model uses a blending function near the wall from the k-ω Standard model, which provides a slow transition from the boundary layer towards the higher Reynolds number k-ε model. It contains the modified turbulence viscosity equation containing the transport effects. Transport equations are similar to the standard k-ω model and contain additional terms. These terms are calculated as follows;

$$\tilde{G}_k = min\,(G_k, 10\rho\beta^* k\omega) \tag{3.41}$$

Here; $\tilde{G}_k$ is production of turbulence kinetic energy.

$$D_\omega = 2 - (1 - F_1)\rho \frac{1}{\sigma_{\omega,2}\omega} \frac{\partial k}{\partial x_j} \frac{\partial \omega}{\partial x_j} \tag{3.42}$$

D_ω is the diffusion modification constant.

While the diffusivity equations are the same to other ω model, the turbulence viscosity is calculated as follows;

$$\mu_t = \frac{\rho k}{\omega} \frac{1}{max\left[\frac{1}{\alpha^*}, \frac{SF_2}{a_1 \omega}\right]} \tag{3.43}$$

Model constants can be found in Fluent theory guide in 2013 [53, 54].

3.8 Wall Functions

The wall functions are a bridge that fills the gap between the wall and the first mesh cell logarithmic region, is located. In this study, as in the geometric model studied, the turbulence scale is much smaller than the boundary layer thickness in the flows where the flow is greatly influenced by the presence of the wall. As the Reynolds number increases, the boundary layer thickness decreases, so the solution variables have large gradients near the wall. A number of time-averaged turbulence models can analyze the flow in the interior rather than the flow near the wall. For this reason, the regions affected by viscosity are modeled by using quasi-experimental equations called wall functions. In this way, the areas close to the wall do not need to be equipped with a very frequent meshes. In this study, by considering the value of Reynolds number, Standard wall function and Enhanced Wall Treatment approach were used with appropriate turbulence models. In this study where turbulence and heat transfer effects are in effect, y + value is determined to be suitable for the turbulence model while the mesh is formed in the vicinity of the wall and the wall functions to be used are determined accordingly. The y+ range in ANSYS FLUENT software is generally specified as $1 < y+ < 30$. However, the problems with turbulence and heat transfer have a y + value of about 1 [53]. Since the Scalable Wall Function property can be used in situations where y + value is too high, this function is not suitable when the geometric dimensions in this study are taken into consideration. The non-equilibrium Wall Function is not recommended for high Reynolds numbers ($Re>10^6$) and is recommended for jet outflow flows, because it is recommended for systems with little vortex propagation.

3.8.1 Standard Wall Function (SWF)

The logarithmic wall law for the average velocity in the momentum equation is defined as follows:

$$U^* = \frac{1}{k} \; ln(E\, y^*) \tag{3.44}$$

Here, the dimensionless speed and the dimensionless distance to the wall are defined as follows;

$$U^* = \frac{U_p C_\mu^{1/4} k_p^{1/2}}{\tau_w/\rho} \tag{3.45}$$

$$y^* = \frac{\rho C_\mu^{1/4} k_p^{1/2} y_p}{\mu} \tag{3.46}$$

The y * value in the above equations varies depending on the Reynolds number.

The logarithmic law in ANSYS FLUENT software is applied when y *> 11.225. When y * <11.225, the laminar strain-elongation relationship is written in U * = y * in the neighboring cells of the wall.

In the ANSYS FLUENT software, the logarithmic wall law is applied for the average temperature area. The thickness of the heat transfer layer is different from the thickness of the viscous sublayer and varies according to the fluid type. The logarithmic wall law for the average temperature area is defined as follows;

$$T^* = \frac{(T_w - T_p) C_\mu^{1/4} k_p^{1/2} \rho C_p}{q} = \begin{cases} Pr\, y^* + \frac{1}{2}\rho P_r \frac{C_\mu^{1/4} k_P^{1/2}}{q} \; (y^* < y_T{}^*) \\ Pr_t \left[\frac{1}{k} ln(Ey^*) + P\right] + \frac{1}{2}\rho \frac{C_\mu^{1/4} k_p^{1/2}}{q} * \\ \{Pr_t U_P^2 + (Pr - Pr_t) U_c^2\} (y^* > y_T{}^*) \end{cases} \tag{3.47}$$

Here P is calculated as follows [57];

$$P = 9.24 \left[\left(\frac{Pr}{Pr_t}\right)^{3/4} - 1\right] \left[1 + 0.28 e^{-0.007 Pr/Pr_t}\right] \tag{3.48}$$

3.8.2 Enhanced Wall Treatment (EWT)

This wall approach is recommended for low Reynolds numbers, where y + is about 1 or for problems with complex wall effects. Therefore, this approach has been used in this study. In this approach, the inlet flow area is divided into two sublayer affected by viscosity and completely turbulent. The boundary between these two zones is determined using the Reynolds number given in terms of the distance to the wall. This Reynolds number is calculated as follows;

$$Re_y = \frac{\rho y \sqrt{k}}{\mu} \tag{3.49}$$

There, y is defined as the vertical distance between the center of the cell and the wall. In ANSYS FLUENT software, this distance is expressed as the distance to the nearest wall as follows;

$$y = \min_{\vec{r}_w \epsilon \Gamma_w} \|\vec{r} - \vec{r}_w\| \tag{3.50}$$

3.9 Heat Transfer Theory-The Energy Equation

In general energy equation defined as;

$$\frac{\partial}{\partial t}(\rho E) + \nabla.\left(\vec{V}(\rho E + p)\right) = \nabla.(k_{eff}\nabla T - \textstyle\sum_j h_j \vec{J}_j + (\bar{\tau}_{eff}.\vec{V})) + S_h \tag{3.51}$$

where k_{eff} is the effective conductivity (k+k_t , where k_t is the turbulent thermal conductivity, defined according to the turbulence model being used), and $\vec{J}_j$ is the diffusion flux of species *j*. The first three terms on the right-hand side of Equation 3.51 represent energy transfer due to conduction, species diffusion, and viscous dissipation, respectively. S_h includes the heat of chemical reaction, and any other volumetric heat sources you have defined.

CHAPTER 4

RESULTS AND DISCUSSION

4.1 Three-Dimensional Model Geometries

In this study, it was investigated that the thermal and hydrodynamic interactions in the flow consisting of delta-flip-shaped vortex generators (VGs) with different configurations placed internally to the slant surfaces of an equilateral triangular channel. In order to verify experimental study, a model geometry equivalent to the experimental model was created. The geometric parameters related to the triangular channels and the delta-winglets are described in Vasudevan et al. and Akcayoglu studies [45, 58]. Detail representation of this model are given between Figure 4.1. and Figure 4.3. This geometry consists of only two pairs of fins placed internally to the side walls of the triangular channel. The length of the channel in the z-direction is 963.7 mm, (L = 16.5D, D is hydraulic diameter). The length of one side of the channel is 100 mm, and the angle of the winglets with the flow direction (angle of attack) is 30°. The winglet dimensions are 44.891 mm x 12.826 mm (= 0.77Dx0.22D). The thickness of the fins is L_w = 3 mm. The distance of the first wing pair mounted to the triangular channel to the entrance of the channel is 89.78 mm (= 2X0.77D) and the distance to the base is 37.89 mm (= 0.67D). Drawing of geometric models was carried out with SOLID WORKS solid modeling program. After the drawing process, the flow volume was defined on DESIGN MODELER, and the any drawing errors were checked and repaired. ANSYS MESH PLATFORM was used to create the meshes.

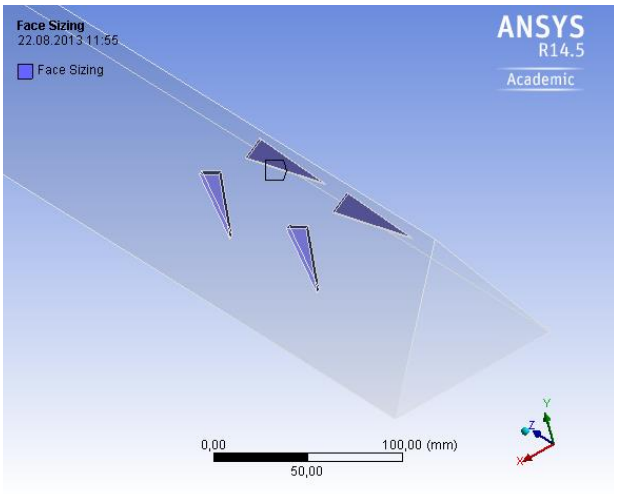

Figure 4.1 3-D view of models inlet

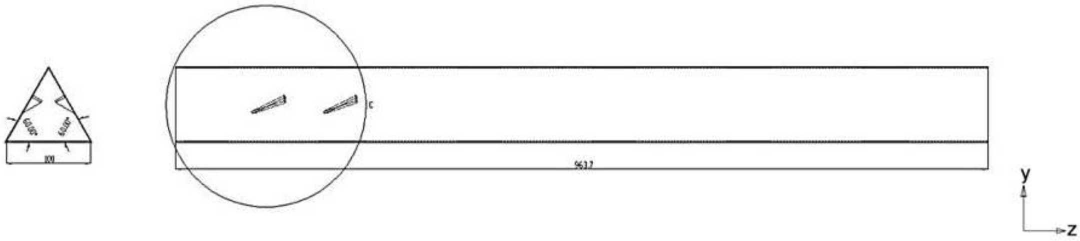

Figure 4.2 Front and side view of experimental models, all dimensions are in mm.

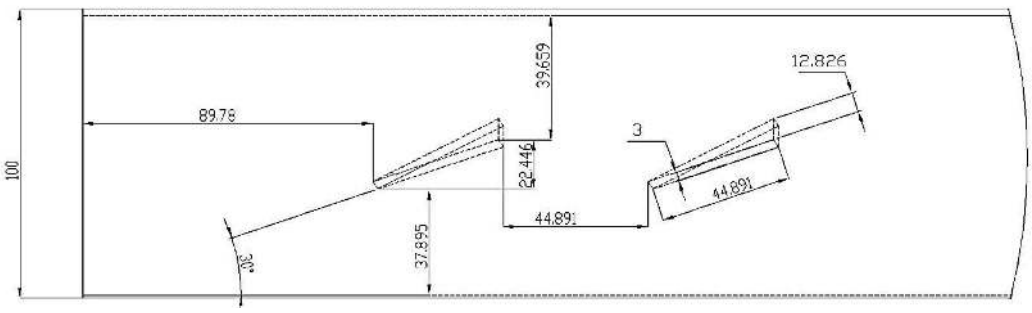

Figure 4.3 A detailed drawing of the marked area in Figure 4.2, all dimensions are in mm.

After the experimental study validation studies, the thesis model geometries used in the research were given in the form of drawings and explanations in detail in the relevant sections of this study, and some models can be drawing were shown between Figure 4.4 and Figure 4.11. These geometries are CFU-CFU (Figure 4.4 and Figure 4.5), CFD-CFD (Figure 4.6 and Figure 4.7), CFU-CFD (Figure 4.8 and Figure 4.9), and CFD- CFU (Figure 4.10 and Figure 4.11) as a type of buildings of configurations.

Several tried out for obtain best configuration that changed distance between winglets (d), winglet dimensions, distances of the winglets to the bottom of the channel, and aspect ratio of the VGs. In the following figures, d is the distance between the winglets, L_w refers to the base length of the winglets.

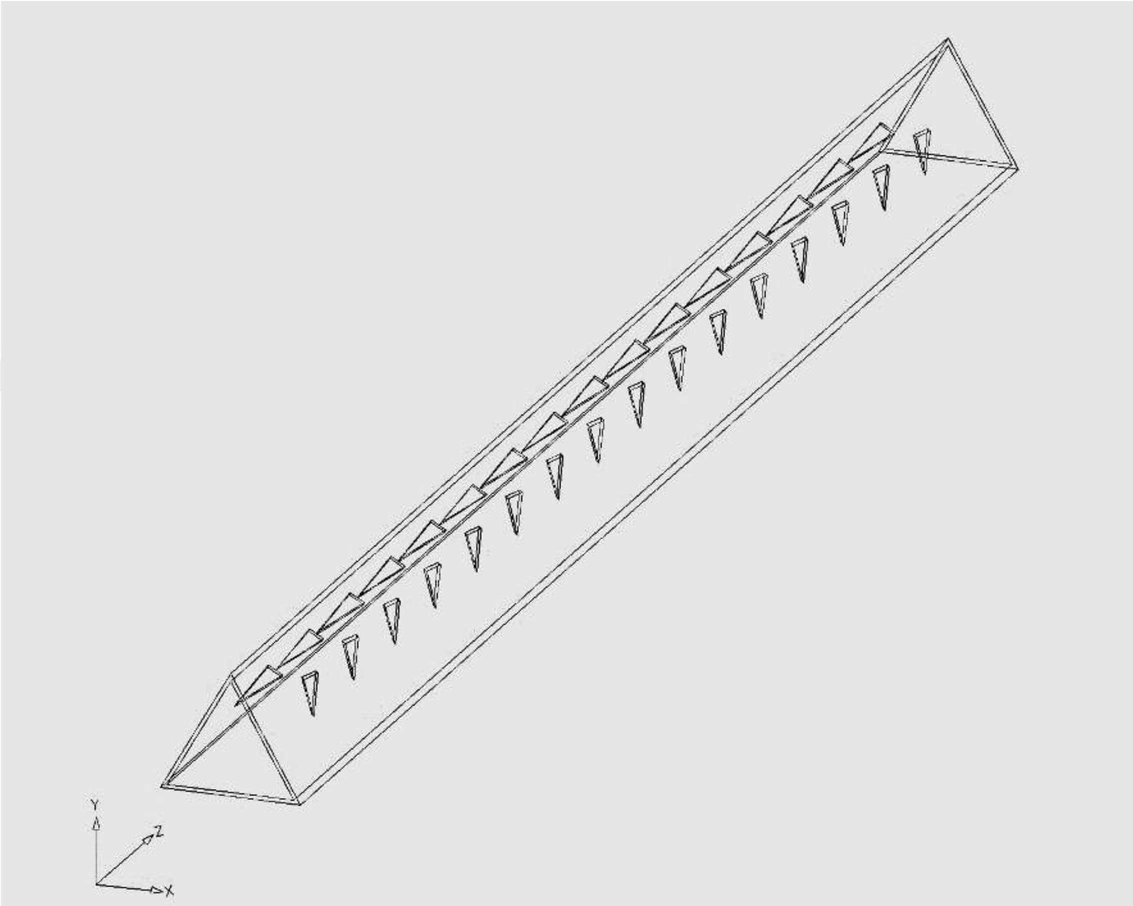

Figure 4.4 3-D view of CFU-CFU model (d/Lw=1).

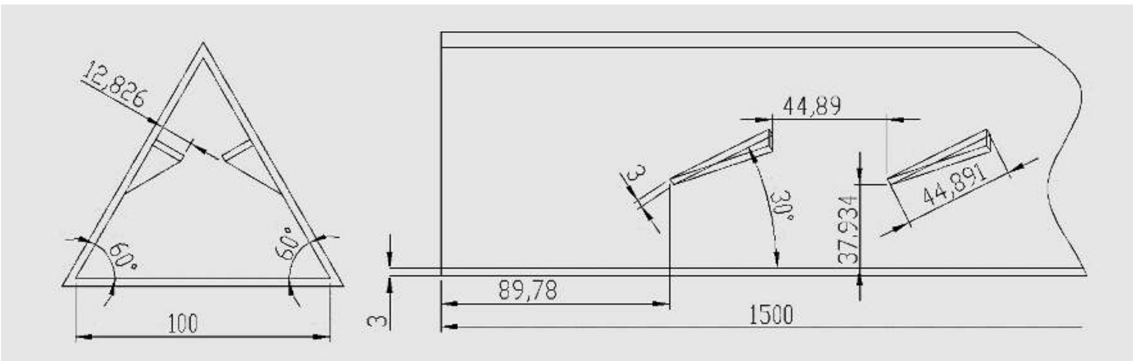

Figure 4.5 Front and side views of CFU-CFU model, all dimensions are in mm (d/Lw=1).

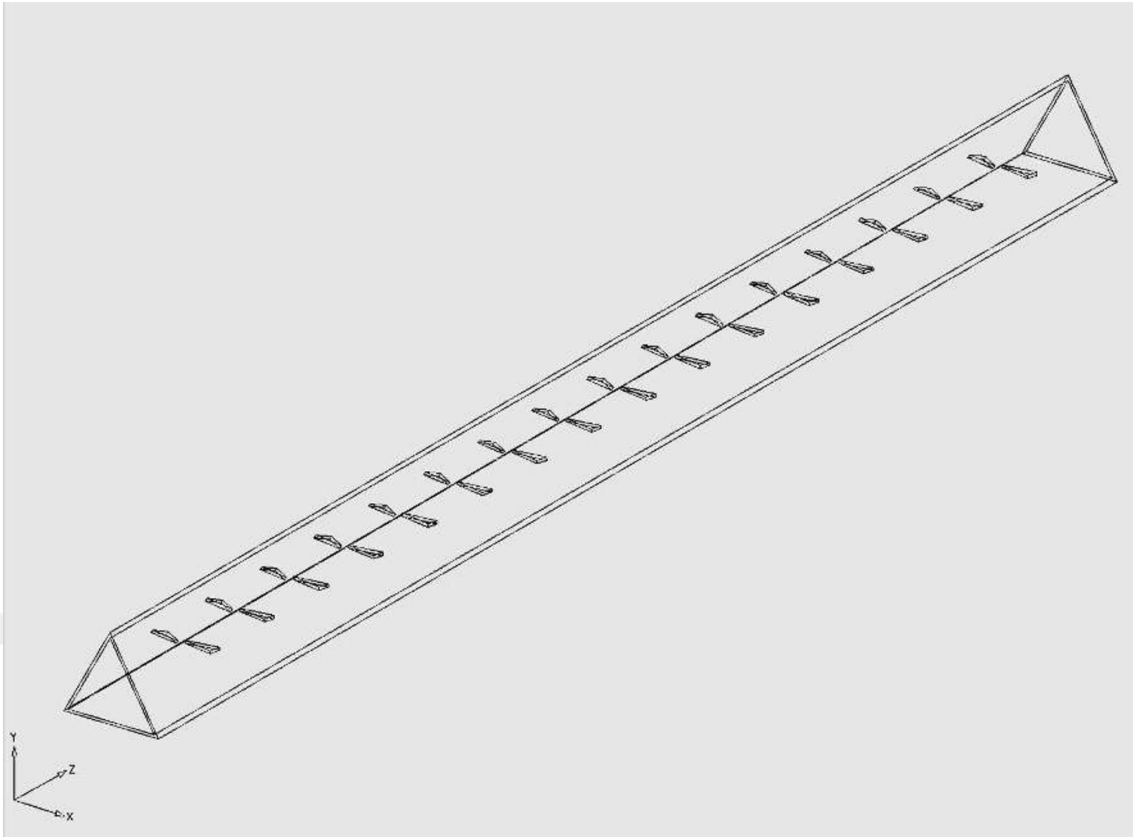

Figure 4.6 3-D view of CFD-CFD model (d/Lw=1)

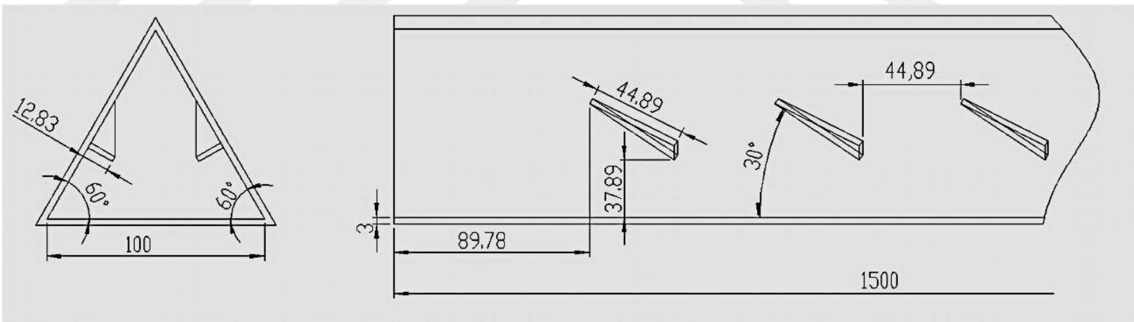

Figure 4.7 Front and side views of CFD-CFD model, all dimensions are in mm (d/Lw=1).

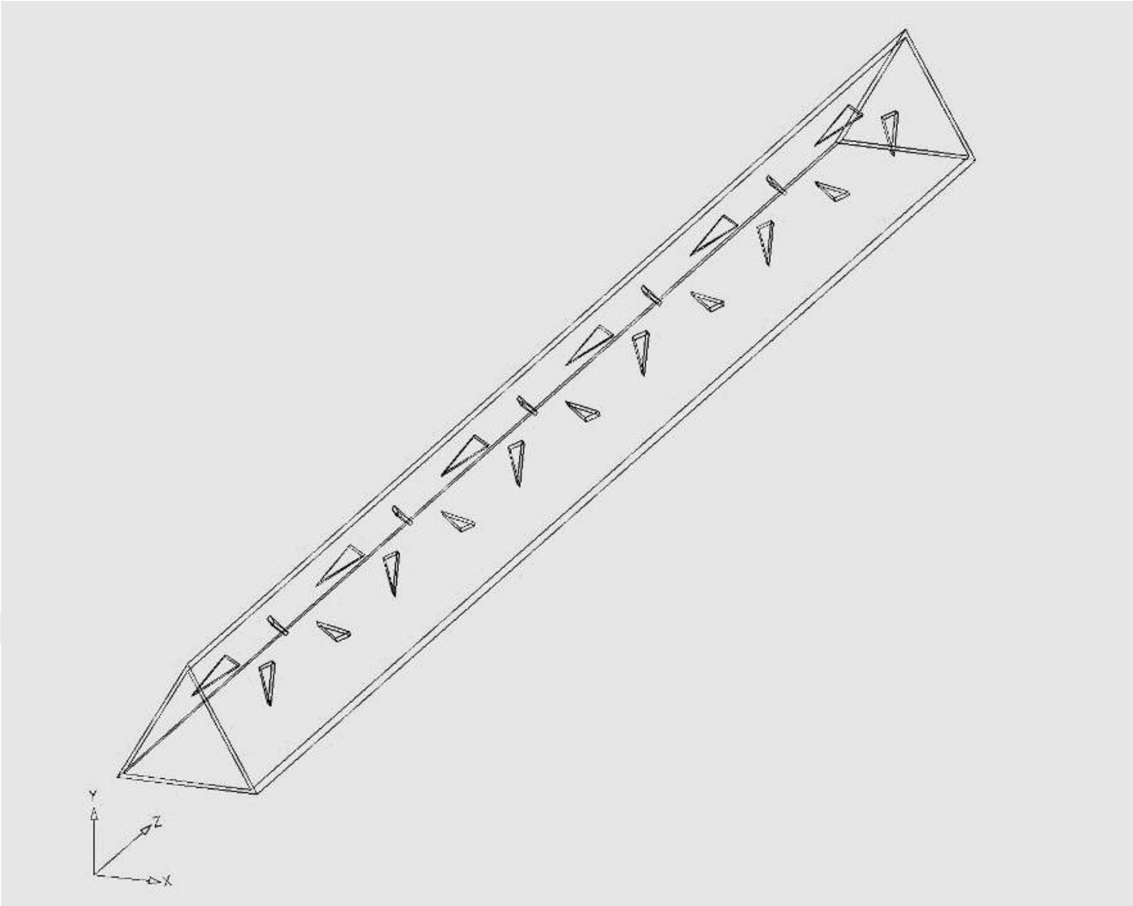

Figure 4.8 3-D view of CFU-CFD model (d/Lw=2).

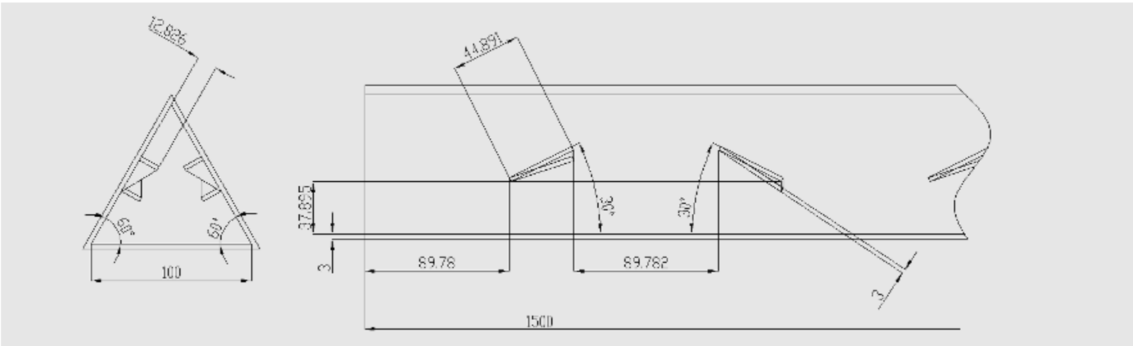

Figure 4.9 Front and side views of CFU-CFU model, all dimensions are in mm (d/Lw=2).

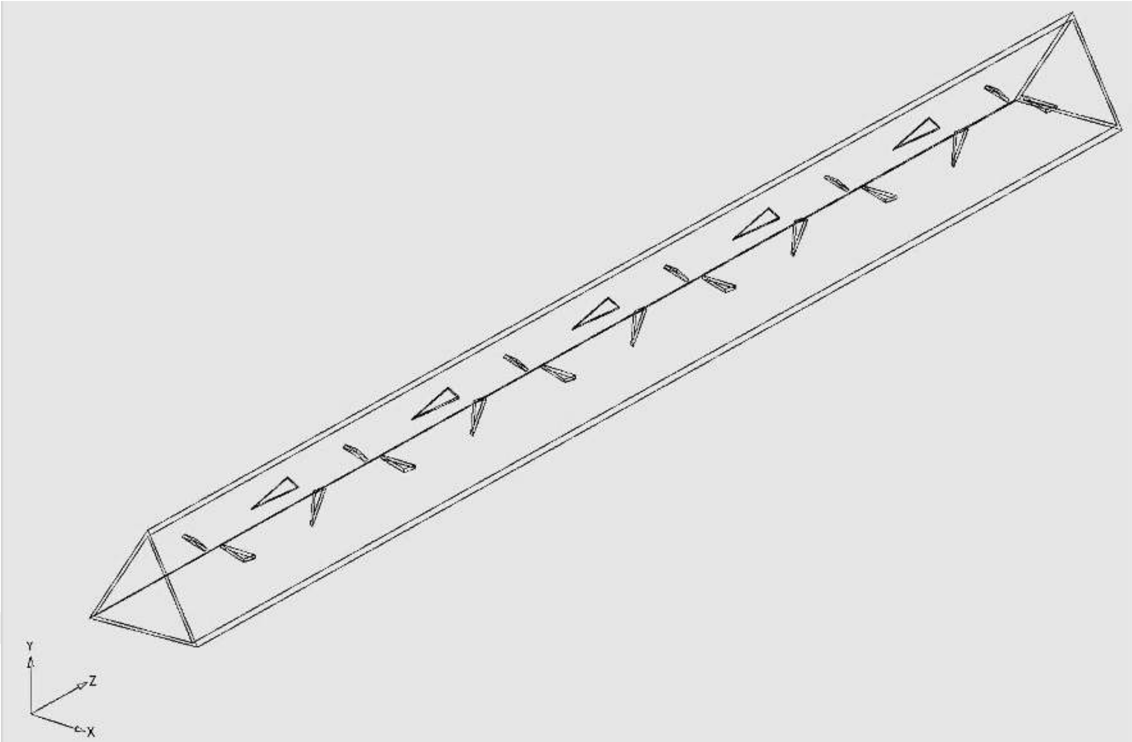

Figure 4.10 3-D view of CFD-CFU model (d/Lw=2).

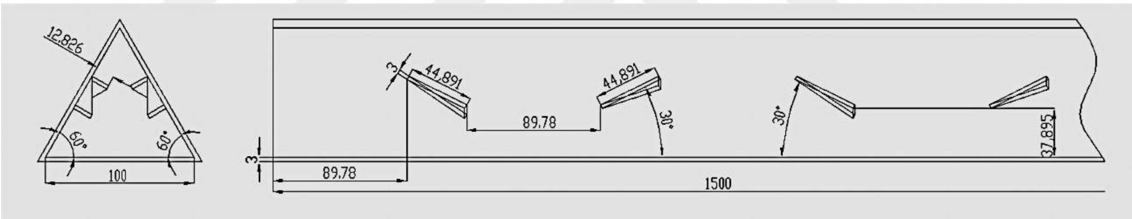

Figure 4.11 Front and side views of CFD-CFU model, all dimensions are in mm (d/Lw=2).

4.2 Detailed of Meshes

In this study, examined in detailed researches about meshes were created. Within the scope of these studies, meshes have been created by using ICEM CFD program and ANSYS MESH PLATFORM program. The ICEM CFD, a program that requires a great deal of time and effort, including the steps of forming a much more difficult meshes, seeks to equip the solution area with quadrilateral cells (Figure 4.12-Figure 4.13). Due to this feature, the ICEM CFD has automatically turned the tips of the wings which should be pointed to be original, causing the ends of the wings to turn into a frustoconical structure (Figure 4.12-Figure 4.13). Since this does not reflect the actual geometrical structure, it has also affected the solution results and has been forced to not make realistic solutions. Due to the mentioned reasons, it was decided that the use of ICEM CFD program is not suitable for this study. For this reason, all methods such as Automatic, Assembly, (Tetrahedrons and Cutcell) under ANSYS MESH PLATFORM have been used, numerous experiments have been tried and the result of the comparison with the experimental results [45], resulting in the expected meshes. The experimental data of Akçayoğlu [45] was used for shape and dimensiona of the channel.

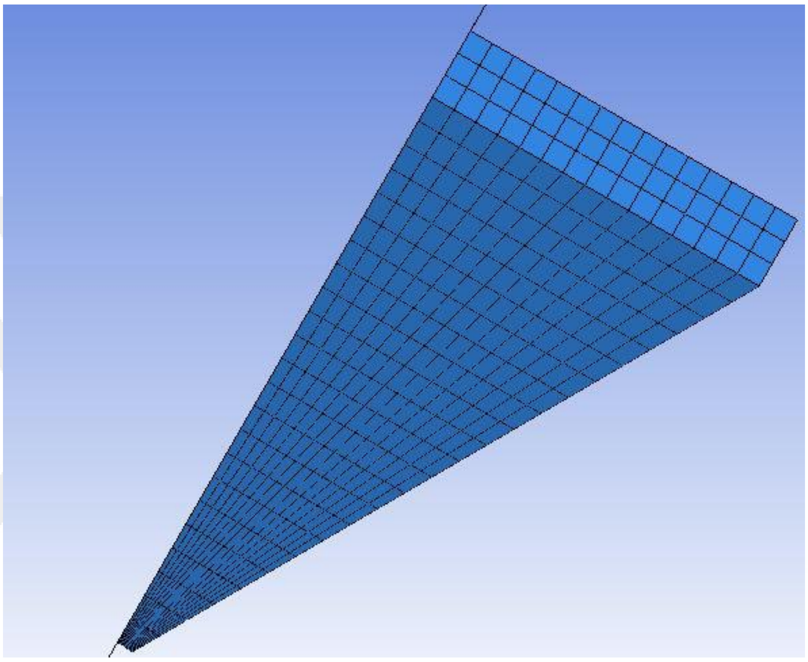

Figure 4.12 Winglet meshes structure created by ICEM CFD program.

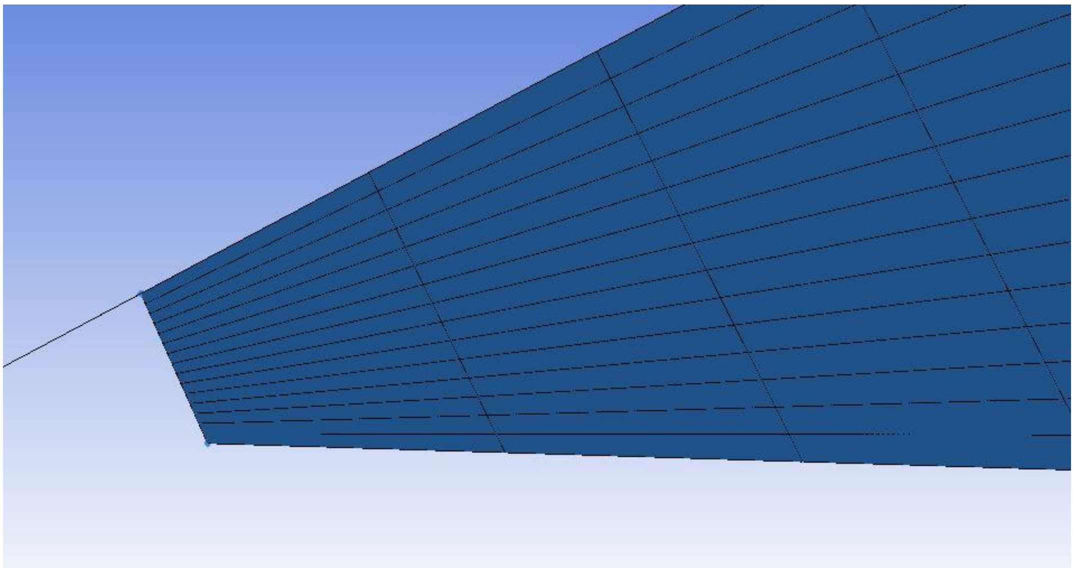

Figure 4.13 Tip of winglet replaced by the ICEM CFD program.

The models drawn obtained by the Solid Works program were transferred to ANSYS WORKBENCH using the “DESIGN MODELER” module. In the DESIGN MODELER module, firstly the faults in the model geometries are detected and repaired. After repairing process, the creation of meshes with deterioration of mesh quality and also of obtaining incorrect solutions were prevented.

There are 6 different mesh options available in the ANSYS MESH PLATFORM module. “Multizone” and “Sweep” mesh options; respectively, since it is suitable for geometries with a large number of volumes and geometries with no indentations. So that methods are not used in this study. “Automatic”, “Tetrahedrons” and “Hex-dominant” mesh options are more suitable for the geometric structure of the study geometries. The “Orthogonal Quality” values are also examined for meshes. Accordingly, the best results in terms of meshes quality are obtaining “Automatic” and “Tetrahedrons” is provided with options. When “Hex-dominant” option is used, the solution area is meshed with hexagonal and tetrahedrons elements. In “Hex-dominant” option, meshes are generally created hexagonal type. With “Tetrahedrons” option, “quadrilateral” meshes can be created. Although many methods have been tried, the quality of the meshes created with the “Hex-dominant” option has not been suitable. Because, in the solution area, Tet4, Hex8, Wed6, Pyr5 elements were formed and the meshes quality was unsuitable. However, the models having all different mesh methods were transferred to ANSYS FLUENT and solutions were obtained.

Figure 4.14 shows the meshes of the triangular channel formed by ANSYS MESH PLATFORM. The statistical data at the bottom of the figure gives information about the quality of the meshes structure. The value based on mesh quality is a parameter that allows the creation of a meshes quality structure called in Orthogonal Quality. The selection of the best mesh which comparison with experimental data and Orthogonal Quality.

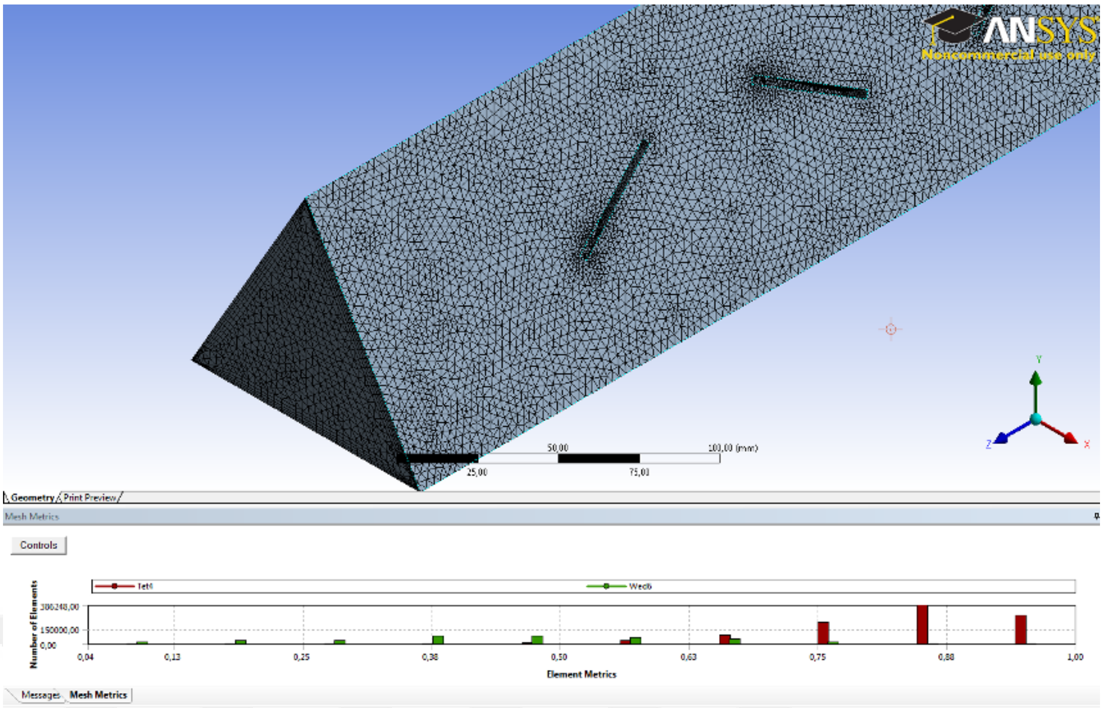

Figure 4.14 Global meshes of the equilateral triangle channel

Figure 4.15 shows some other details about the network structure. The "Proximity and Curvature" option ensures that the transitions between neighboring cells in the meshes do not create sharp corners. For all cases, y^+ value is calculated. y^+ value is approximately 1.2 or 1 for all meshes if that are includes “edge sizing” and “inflation” are used.

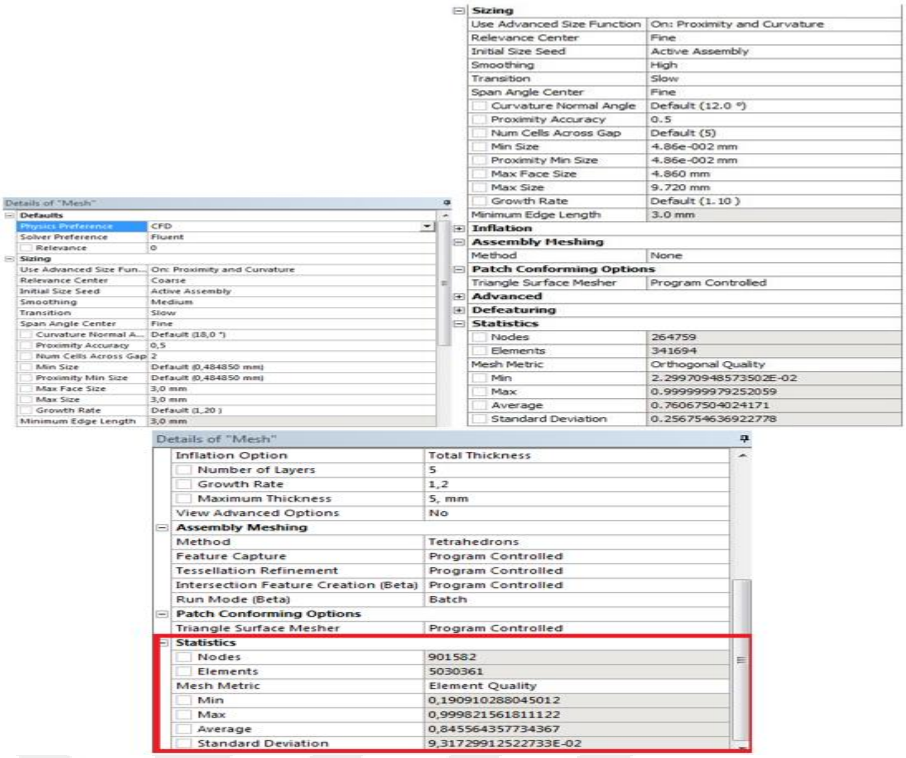

Details of "Mesh"

Defaults	
Physics Preference	CFD
Solver Preference	Fluent
Relevance	0
Sizing	
Use Advanced Size Fun...	On: Proximity and Curvature
Relevance Center	Coarse
Initial Size Seed	Active Assembly
Smoothing	Medium
Transition	Slow
Span Angle Center	Fine
Curvature Normal A...	Default (18,0 °)
Proximity Accuracy	0,5
Num Cells Across Gap	2
Min Size	Default (0,484850 mm)
Proximity Min Size	Default (0,484850 mm)
Max Face Size	3,0 mm
Max Size	3,0 mm
Growth Rate	Default (1,20)
Minimum Edge Length	3,0 mm

Sizing	
Use Advanced Size Function	On: Proximity and Curvature
Relevance Center	Fine
Initial Size Seed	Active Assembly
Smoothing	High
Transition	Slow
Span Angle Center	Fine
Curvature Normal Angle	Default (12.0 °)
Proximity Accuracy	0.5
Num Cells Across Gap	Default (5)
Min Size	4.86e-002 mm
Proximity Min Size	4.86e-002 mm
Max Face Size	4.860 mm
Max Size	9.720 mm
Growth Rate	Default (1.10)
Minimum Edge Length	3.0 mm
Inflation	
Assembly Meshing	
Method	None
Patch Conforming Options	
Triangle Surface Mesher	Program Controlled
Advanced	
Defeaturing	
Statistics	
Nodes	264759
Elements	341694
Mesh Metric	Orthogonal Quality
Min	2.29970948573502E-02
Max	0.999999979252059
Average	0.76067504024171
Standard Deviation	0.256754636922778

Details of "Mesh"

Inflation Option	Total Thickness
Number of Layers	5
Growth Rate	1,2
Maximum Thickness	5, mm
View Advanced Options	No
Assembly Meshing	
Method	Tetrahedrons
Feature Capture	Program Controlled
Tessellation Refinement	Program Controlled
Intersection Feature Creation (Beta)	Program Controlled
Run Mode (Beta)	Batch
Patch Conforming Options	
Triangle Surface Mesher	Program Controlled
Statistics	
Nodes	901582
Elements	5030361
Mesh Metric	Element Quality
Min	0,190910288045012
Max	0,999821561811122
Average	0,845564357734367
Standard Deviation	9,31729912522733E-02

Figure 4.15 Mesh details.

Figure 4.16 shows the side of the edges of the winglets by using the “edge size“ feature.

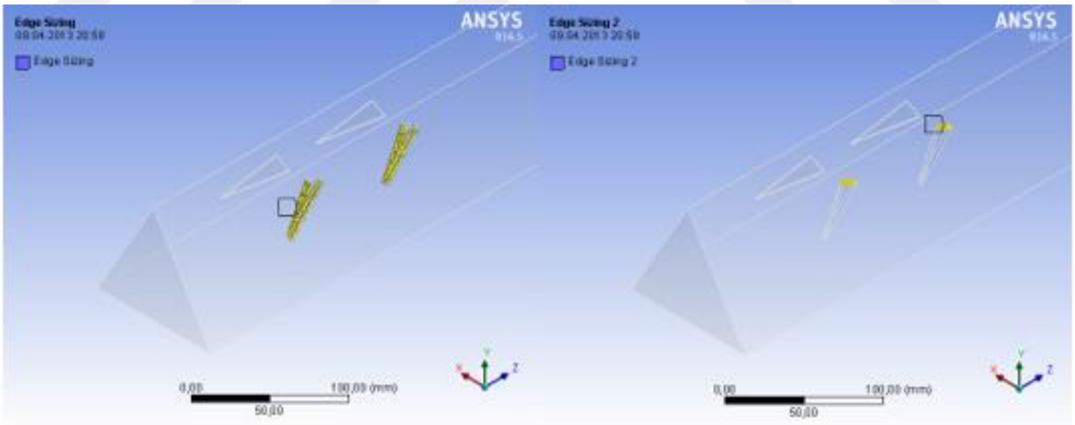

Figure 4.16 Meshed the long and short sides of the winglets by the “edge size”.

“Orthogonal quality” parameters must be optimal value, the parameter called “Edge Sizing” must be assigned an appropriate value. Through this feature, the edges of the delta-winglets are separated into a suitable number of elements and the meshes are more frequent. Figure 4.16 shows the face sizing surfaces. Meshes structures are created by using “inflation” option to obtain smooth transitions between local-global meshes and high number of meshes near wall where winglets and channel wall. Inflation feature is shown in Figure 4.17.

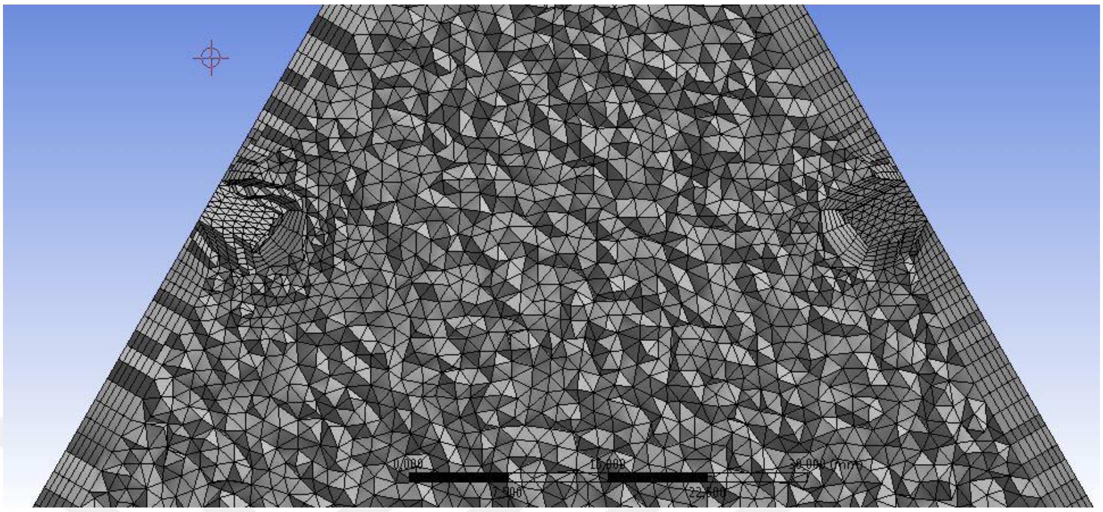

Figure 4.17 Meshes structure using “inflation” feature on the edges of the channel and winglets

Figure 4.18 shows some of the meshes created by the “Assembly Tetrahedrons” method using different number of elements. As a result of the comparisons with the experimental study, the meshes providing the best combination was determined as inflation option with the number of 3,187,501 elements (Figure 4.20). The details of this meshes are shown in Figure 4.19.

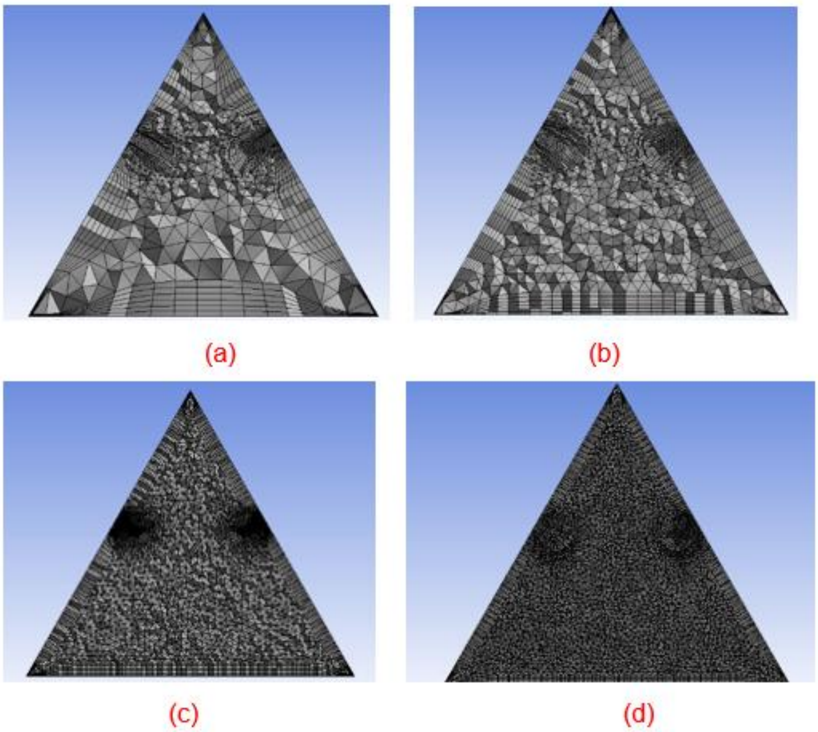

Figure 4.18 Meshes formed by the “Assembly Tetrahedrons” method; (a) Meshes numbers are 287,379 elements; (b) Meshes numbers are 907,947 elements; (c) Meshes numbers are 3,187,501 elements; (d) Meshes numbers are 5,917,839 elements.

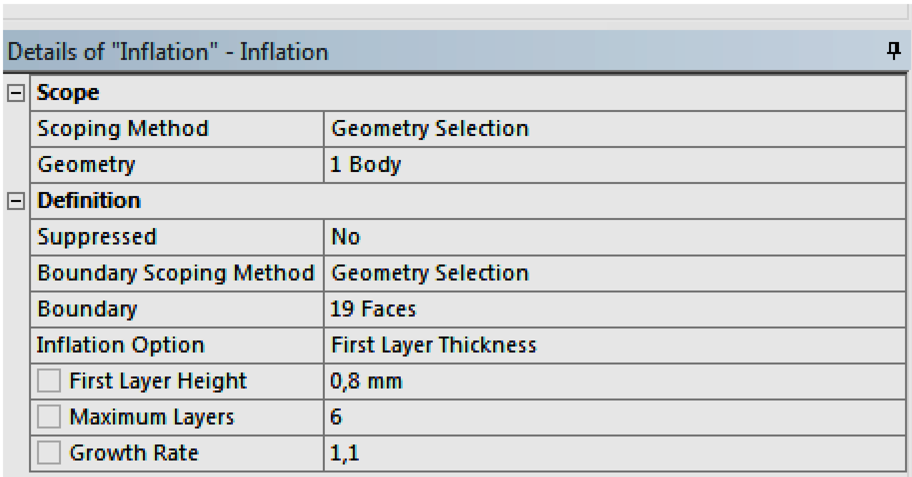
Details of "Inflation" - Inflation

Scope	
Scoping Method	Geometry Selection
Geometry	1 Body
Definition	
Suppressed	No
Boundary Scoping Method	Geometry Selection
Boundary	19 Faces
Inflation Option	First Layer Thickness
First Layer Height	0,8 mm
Maximum Layers	6
Growth Rate	1,1

Figure 4.19 Details of meshes created by inflation option for best configuration (for meshes with 3,187,501 number of elements).

4.2.1 Grid Independency

In this project, 311,875, 974,369, 3,187,501, 4,986,342 and 5,921,749 numbers of mesh elements are tested. As mesh element numbers greater than 311,875 showed invariant results in terms of predicted velocity distribution shown in Figure 4.20, then adopting 3,187,501 elements in the computational domain is regarded as the results are grid independent, since the difference between the computational time for the simulations with 974,369 and 3,187,501 element sizes are not very much. The mesh validity has also been tested in terms of refinement of mesh near the wall regions. The value of y+ is calculated as 1.17 when 3,187,501 elements are used. By using 3,187,501 mesh elements in the calculations, the deviation between the experimental results and the computed results are no more than 0.11%[59] .

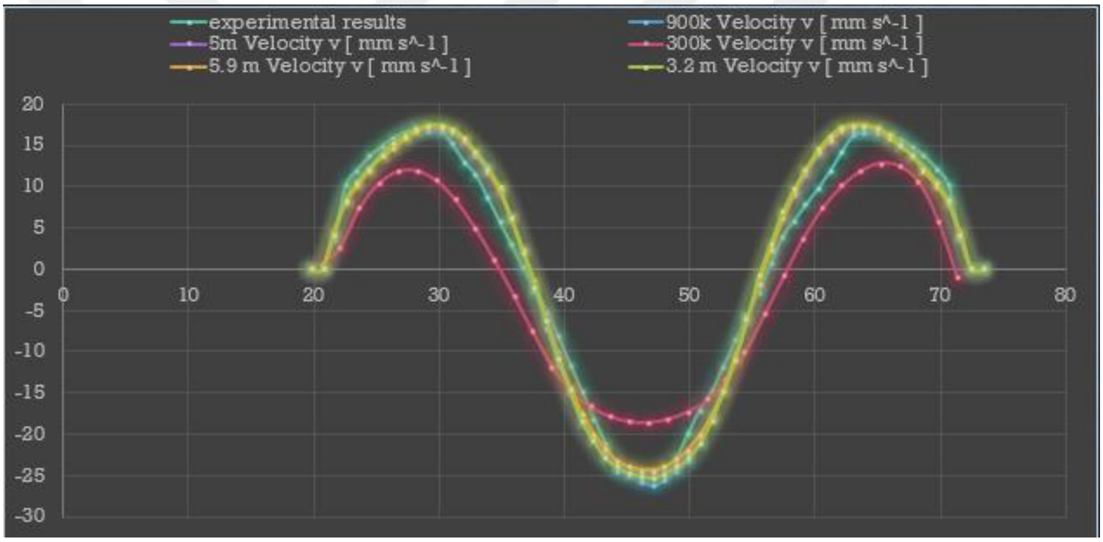

Figure 4.20 Experimental and numerical results for grid independency at mid line of channel

In Figure 4.20, it is seen the velocity distribution on a line, z=286.287 mm, y=36.56 mm. The optimum result is obtained by 3,187,501 number of mesh elements and the results revealed no difference for more than 3,187,501 mesh elements.

4.2.2 Details of Selected Best Mesh

The best mesh includes 3,187,501 elements, and created by “Assembly Tetrahedrons” method. Additionally, used face sizing is 0.7 mm for delta-winglets long and short edge and channel wall. Inflation used for like face sizing at a growth rate of 1.1. First layer height and maximum length is 0.8 and 6 mm, respectively. Front view of this model can be seen in Figure 4.21.

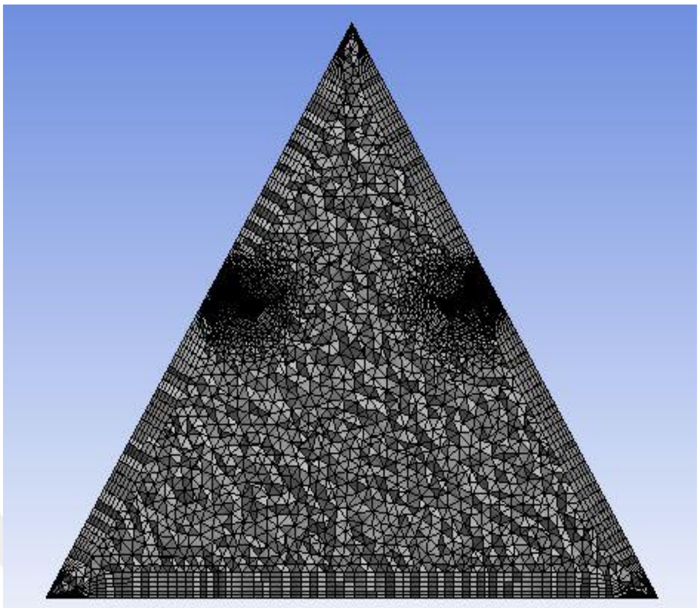

Figure 4.21 Front view of selected meshes at VGs.

4.3 Details of Numerical Solution and Boundary Conditions

After meshed models are transferred ANSYS FLUENT program, boundary condition and working fluid physical properties is needed for the software. Water and air are selected as working fluids. Water is assumed as incompressible, Newtonian, and having constant physical properties (density 998.2 kg/m^3, specific heat 4186 J/kg-K, thermal conductivity 0.6 W/m-K, and dynamic viscosity 1.003x10^{-3} kg/m-s). The properties of the air is also defined as incompressible, Newtonian, with constant physical properties (density 1.225 kg/m^3, specific heat 1006.4 J/kg-K, thermal conductivity 0.0242 W/m-K, and dynamic viscosity 1.789x10^{-5} kg/m-s). Fluid flow is in the direction of z-axis. The 3 dimensional continuity, Navier-Stokes equations, and energy equation are solved. Triangular channel and delta-winglets materials were selected as aluminum (density=2719 kg/m^3, specific heat=817 J/kg-K, thermal conductivity = 202.4 W/m-K). The dimensionless continuity, momentum and energy equations in surface forces are ignored and are described below:

$$\frac{\partial w}{\partial z} = 0 \tag{4.1}$$

$$\frac{\partial w}{\partial t} + \frac{\partial}{\partial z}\,(v\omega) \;=\; -\frac{\partial p}{\partial z} + \frac{1}{Re}\frac{\partial^2 w}{\partial y \partial y} \tag{4.2}$$

$$\frac{\partial}{\partial y}\,(v\omega)\;=\;\frac{1}{RePr}\frac{\partial^2 T}{\partial y \partial y} \tag{4.3}$$

$$Re = \frac{\rho\, w\, D}{\mu} \tag{4.4}$$

In the equations, “w” represents the mean velocity in the z-direction, “p” is pressure, “Pr” is fluid Prandtl number, the dimensionless fluid temperature represents “T”, the Reynolds number defined by the “Re”, hydraulic diameter is “D”, and the dynamic viscosity is "μ".

In all simulations, SIMPLE was used as a solution for pressure-velocity coupling scheme. “Least Square Cell Based” for gradient, “Standard” for pressure, “Second Order Upwind” for momentum and energy equation are selected in spatial discretization. Also, “Gauss-Seidel linear equation solver” and “Algebraic multigrid” methods are selected.

In the following equations, k, I, ε, ω, ℓ values in the models are given;

$$k = \frac{3}{2}\left(\frac{U_{ave}}{I}\right)^2 \tag{4.5}$$

$$I = 0.16\, Re^{-1/8} \tag{4.6}$$

$$\varepsilon = c_{\mu}{}^{\frac{3}{4}}\frac{k^{\frac{3}{2}}}{\ell} \tag{4.7}$$

$$\ell = 0.6\, D \tag{4.8}$$

$$\omega = \frac{k^{1/2}}{c_{\mu}\,\ell} \tag{4.9}$$

In addition to the convergence criteria, the velocity, pressure and turbulence data exchange at several points were selected in the flow to examine, and after the guarantees were consistently constant (Figure 4.21-Figure 4.23) the solution was stopped.

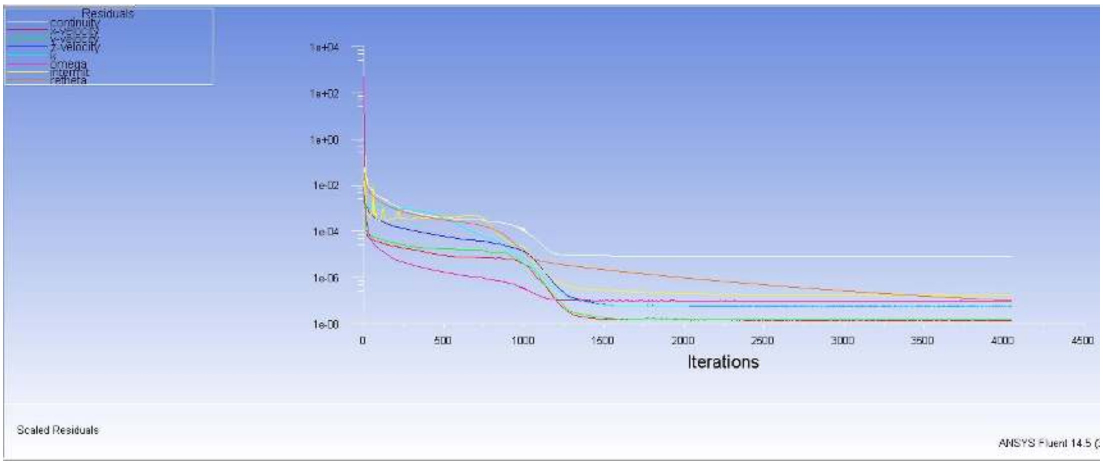

Figure 4.22 Example of convergence graph.

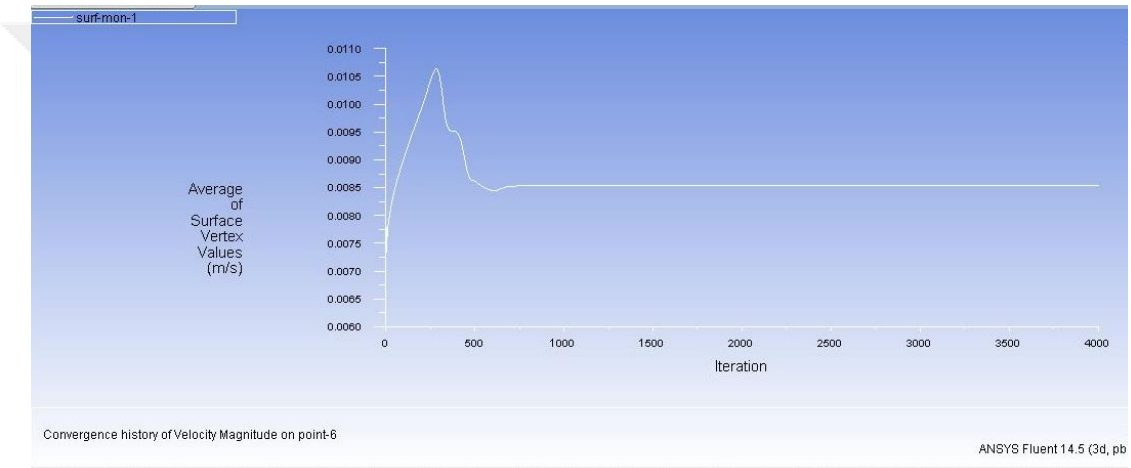

Figure 4.23 Example of velocity distribution at the center point of the channel (x = 50 mm, y = 42 mm, z = 398 mm).

4.4 Numerical Solution Verification with Experiment for Re = 5000 Value

Many different model and wall function are tested for verify the experimental results. The models shown in the Figure 4.24 only for the optimum mesh structure (z=286.287 mm and Z=36.56). The best model is Renormalization group (RNG) k–ε model with enhanced wall treatment wall approach.

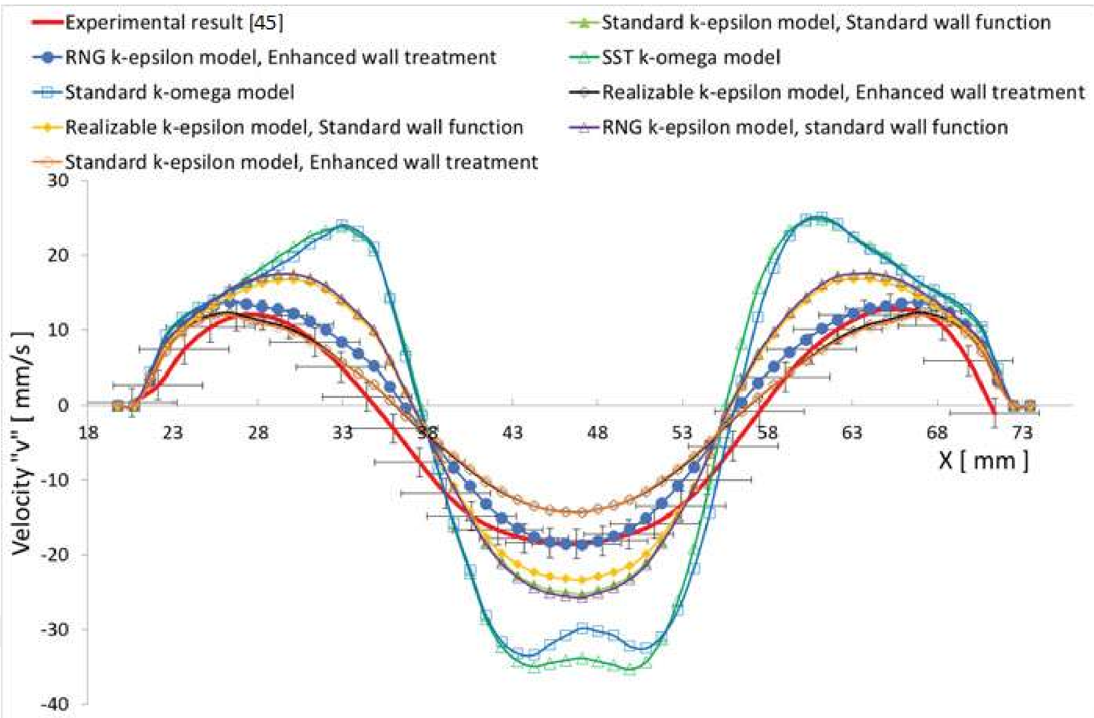

Figure 4.24 Comparison of experimental and numerical results obtained for Re= 5000 on mid-line (0.34D ≤X ≤1.29D, Y = 0.63D, Z = 4.43D) [45, 59].

A summary of the studies is performed so far under the verification of the numerical solution for the value of Re=5000. Mesh element number of this verification was 3187501 with activated “inflation” option for triangular wall and delta winglets and “face sizing” for delta-winglets. Turbulence model was “RNG k- ε” and wall function is “Enhanced Wall Treatment”. Additionally, “swirl dominated flow”, “pressure gradient effect” and “curvature correction” options were activated. The comparison of numerical and experimental results was made by comparing the streamlines, vorticity contours, and velocity profiles obtained in the flow field. After these studies, optimization studies were carried out for the limit values which were the subject of the thesis.

4.5 Introduction to CFD of Gas Turbine Blade Leading Edge

The results obtained from the present numerical study are analyzed in detail and are categorized according to effects of VG configuration, streamwise distance between the VGs, and spanwise distance between the VGs. The main purpose is to help understanding of the best VG orientation and the best geometry in terms of thermal and hydro-dynamic performance obtained for the equilateral triangular duct fitted with various types of VGs. The obtained results are analyzed in the following sections.

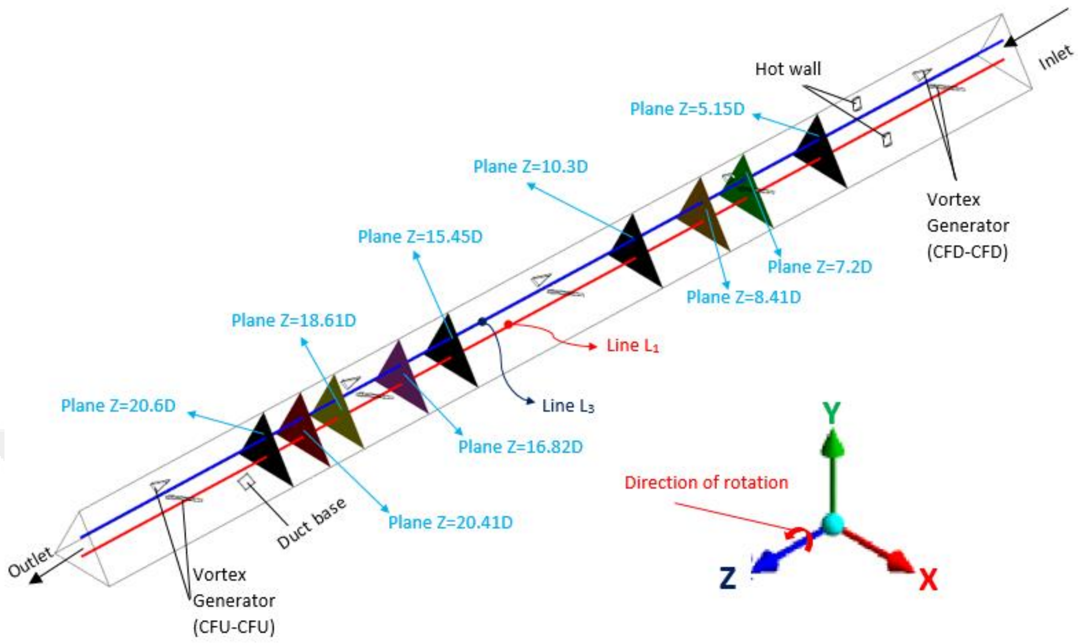

Figure 4.25 Plane, line and VGs types and direction of rotation shows in channel.

4.6 Effects of the VG Configuration and the Streamwise Distance between the VGs

VG features is given at Figure 4.36, VG mounted on the slant surfaces that features: Length of VGs (Lw) is 0.77 D, height of VGs (Hw) is 0.22 D, thickness of VGs are 3 mm and angle of attack made with the flow direction is 30°.

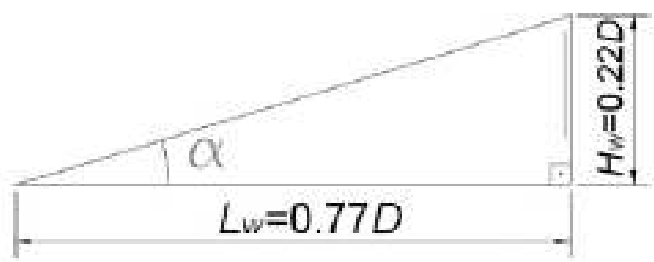

Figure 4.26 VG features

In Figure 4.27, Show the spanwise distances between winglets and, other parameters length.

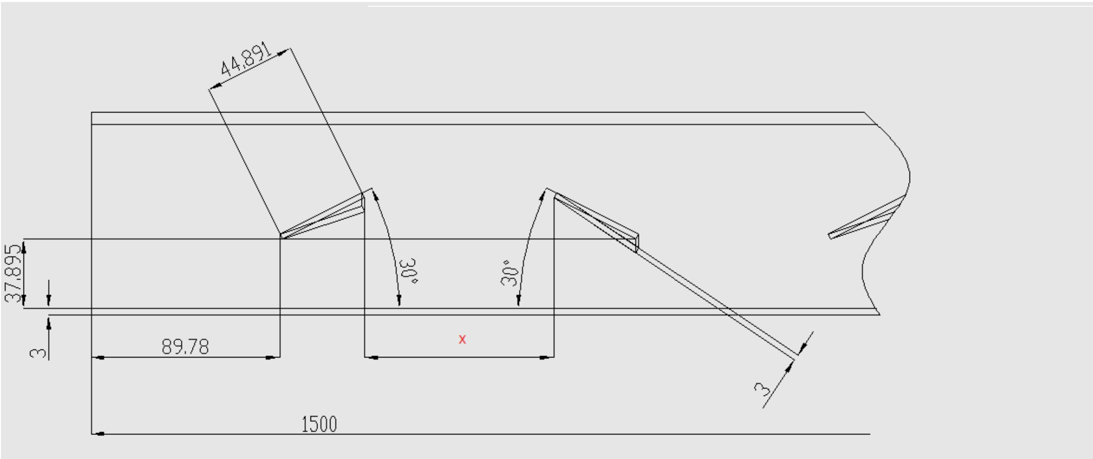

Figure 4.27 Showing spanwise direction of winglets

4.6.1 The Time Averaged Streamline Patterns

Figures between 4.28 and 4.47 show time averaged streamline patterns obtained from different streamwise location planes at Z=7.2D, Z=8.42D, Z=16.82D, Z=18.61D and Z=20.41D for the studied VG configurations. Inspection of these figures reveals that each configuration is able to generate foci in each of the specified local planes. However, there are differences in terms of impact area, location, number, strength and size of the foci as it is clearly seen in these figures. The differences in each streamline patterns obtained from the configurations and cases studied are explained in detail below.

The d/Lw is the ratio of the distance between winglets to length of the VGs. Figure 4.28 shows the time averaged streamline patterns obtained on the specified streamwise locations for the CFU-CFU configuration for d/Lw= 0 case. Note that at each downstream location the flow is separated into 2 parts. A strong focus is observed in the right part of the each plane. As the flow moves downstream, this strong focus gets smaller letting an enlargement of the area of the foci formed in the left part of the planes. Note that the foci located in the left part of the Z=7.2D and Z=8.41D planes interact only with themselves and not with the main flow. Apart from this interaction, the foci formed in each plane never interact with neither with each other nor with the main flow.

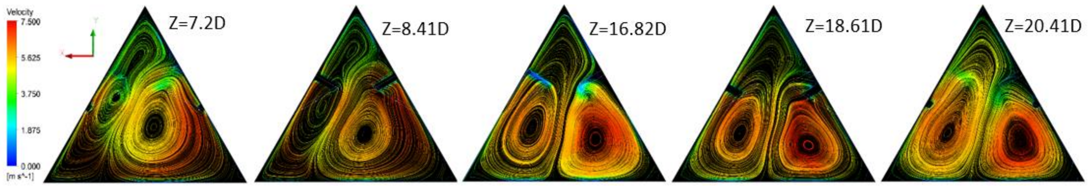

Figure 4.28 Time averaged streamline patterns of CFU-CFU configuration for d/Lw=0 case.

Figure 4.29 shows time averaged streamline patterns obtained on the specified streamwise locations for the CFD-CFD configuration for d/Lw=0 case. It is observed that the flow at the apex of the duct is engendered by the focus formed at the apex at each streamwise location. It is interesting to note that the centers of each foci remain nearly at the same position as the flow moves to the downstream. The focus centred near the left bottom side of the duct gets stronger as the flow moves to the downstream. This movement causes the flow zone to be weakened near the apex of the duct as well as prevention of the secondary flow formation in the vicinity of the left side wall of the duct. As this focus gets stronger, it squeezes the foci formed in the apex and in the left base corner of the duct by reducing their sizes. As the flow moves downstream, the interaction between the foci located on the right of the plane prevents the formation of the secondary flow in the vicinity of the right-bottom side of the wall.

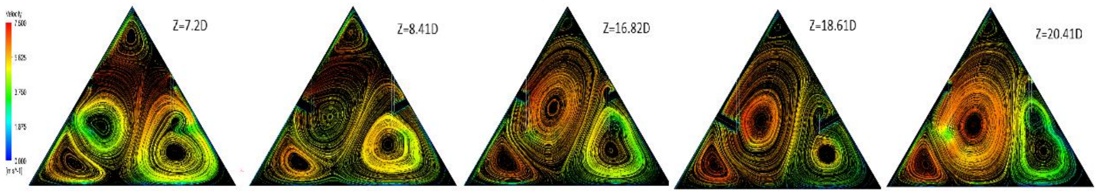

Figure 4.29 Time averaged streamline patterns of CFD-CFD configuration for d/Lw=0 case.

Figure 4.30 shows time averaged streamline patterns obtained on the specified streamwise locations for the CFU-CFD configuration for d/Lw= 0 case. For this configuration and case, the number of vortices is increased in the whole domain and the vortex interaction is good in the upper part of the y-symmetry axis near the apex of the duct at Z=7.2D, Z=8.41D and Z=16.82D planes. Some small-scale secondary flow formation is observed at Z=7.2D plane. The main and the secondary flow mixing in the upper part of the y-symmetry axis is the best at Z=16.82D and is the worst at Z=18.61D.

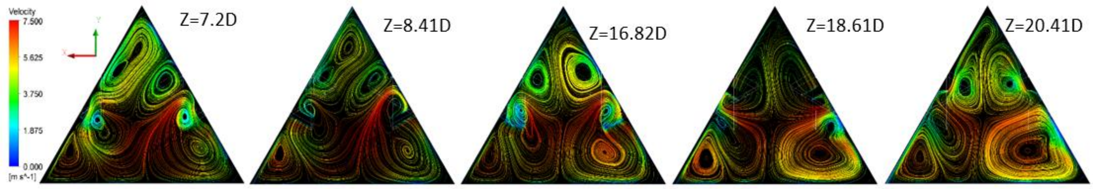

Figure 4.30 Time averaged streamline patterns of CFU-CFD configuration for d/Lw=0 case.

Figure 4.31 shows time averaged streamline patterns obtained on the specified streamwise locations for the CFD-CFU configuration for d/Lw= 0 case. The structures of the foci are found similar to the case shown in Figure 4.30. The main differences observed in Figure 4.30 and Figure 4.31 are as follows: The size of the focus formed in the lower left corner of each plane nearly remains unchanged as the flow moves to downstream and the focus located in the right corner of each plane gets stronger than its former location.

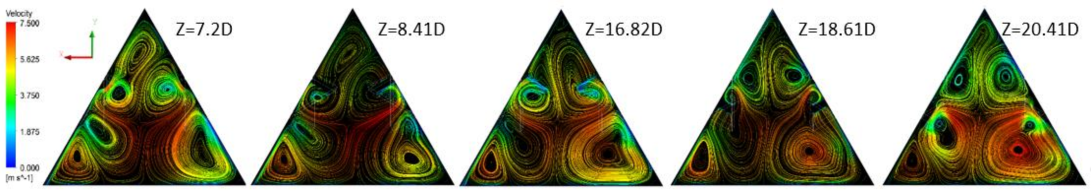

Figure 4.31 Time averaged streamline patterns of CFD-CFU configuration for d/Lw=0 case.

Figure 4.32 shows time averaged streamline patterns obtained on the specified streamwise locations for the CFU-CFU configuration for d/Lw= 0.5 case. The flow structure is found similar to the one shown in Figure 4.28. Therefore, it can be said that the flow is not affected very much by increasing the streamwise distance between the VGs for the CFU-CFU configuration.

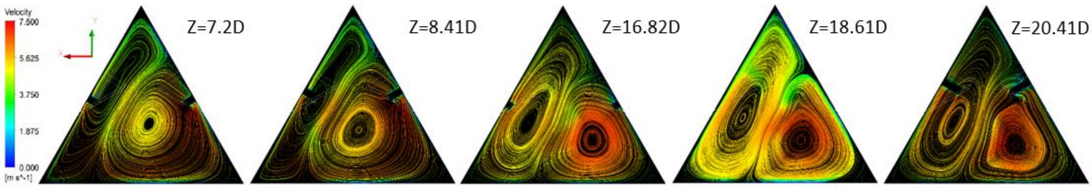

Figure 4.32 Time averaged streamline patterns of CFU-CFU configuration for d/Lw=0.5 case.

Figure 4.33 shows time averaged streamline patterns obtained on the specified streamwise locations for the CFD-CFD configuration for d/Lw= 0.5 case. Since the flow structure is similar to the one obtained for the CFD-CFD configuration for d/Lw= 0 case (Figure 4.29), therefore the similar conclusions can be made such that the flow is not effected too much as the streamwise distance between the VGs is increased from 0 to 0.5 for the CFD-CFD configuration.

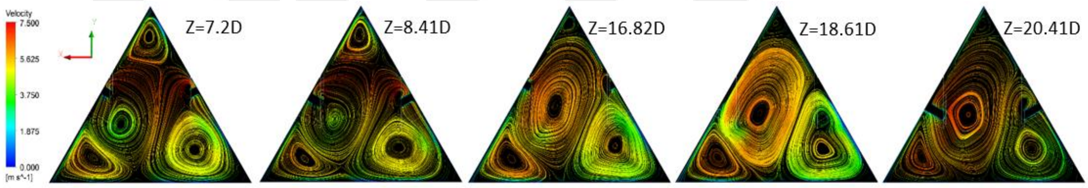

Figure 4.33 Time averaged streamline patterns of CFD-CFD configuration for d/Lw=0.5 case.

Figure 4.34 shows time averaged streamline patterns obtained on the specified streamwise locations for the CFU-CFD configuration for d/Lw= 0.5 case. The focus located in the left corner of each plane decays as the flow moves downwards. A focus located at the apex of the duct and a very strong focus formed in-between the two foci near the base of the duct are observed at Z=16.82D location. However, they weaken as the flow moves downstream, at Z=18.61D and Z=20.41D planes. It is also observed all of the 3 foci located near the base of the duct weaken as the flow moves downstream.

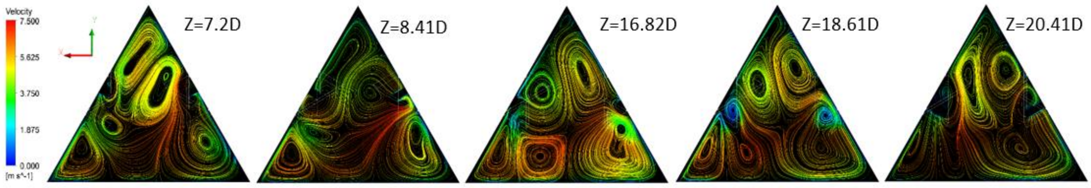

Figure 4.34 Time averaged streamline patterns of CFU-CFD configuration for d/Lw=0.5 case.

Figure 4.35 shows time averaged streamline patterns obtained on the specified streamwise locations for the CFD-CFU configuration for d/Lw=0.5 case. It is clearly seen that foci are distributed everywhere in the Z=7.2D plane. A small-scale foci pair is observed next to the side walls near the center of the duct on the Z=7.2D plane. The left one comes in contact with the focus located in the apex of the duct and the right one comes in contact with the one located next to it. This behavior of the focus is an indication of good heat transfer convection from hot side walls towards the inner section of the duct. At a further downstream location, at Z=8.41D, it is seen that the left and the right small-scale focus observed in the previous location get stronger and both of them come in contact with the flow below the y-symmetry axis. This indicates that these small-scale foci pair engender the flow mixing in the lower part of the plane. At Z=16.82D plane, very small-scale foci are also observed in the vicinity of the duct and another small-scale focus is seen to be located at the apex of the duct. Thus, the dead flow zone in the apex region is engendered by the focus located at the apex of the duct. All the focus is strengthened at a further downstream location, at Z=18.61D plane, by getting an energy from the main flow. A very strong focus is emanated from the bottom surface of the duct (see the separate focus located on the left bottom surface of the duct). The flow in the apex of the duct is still in motion at this downstream location. It is seen that at Z=20.41D plane, the emanated focus observed in the previous plane is still active, but its strength is weakened. It is interesting that even if this weakness in the strength, the focus located on the right and on the left of it conserve their strength.

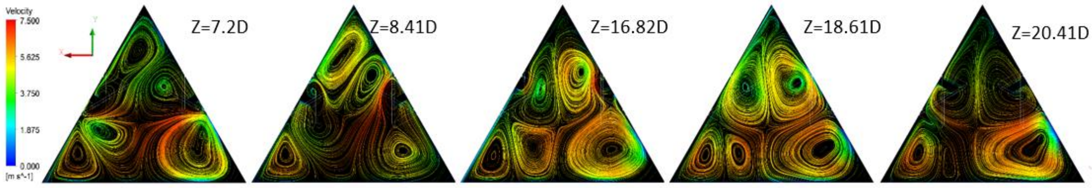

Figure 4.35 Time averaged streamline patterns of CFD-CFU configuration for d/Lw=0.5 case.

Figure 4.36 shows time averaged streamline patterns obtained on the specified streamwise locations for the CFU-CFU configuration for d/Lw=1 case. It is clearly seen that a very big twin foci pair sweeps almost whole of each stremwise plane and their centres shift towards the base of the duct as the flow moves in the downstream direction. By the help of this shift, another small-scale twin foci pair forms near the apex of the investigated planes. It is interesting that the flow character is not changed as the flow moves downstream as if there is no rotation effect.

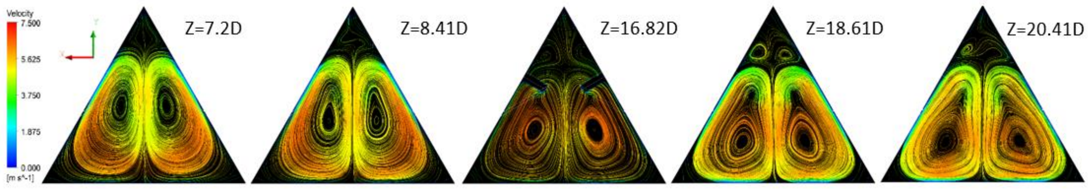

Figure 4.36 Time averaged streamline patterns of CFU-CFU configuration for d/Lw=1 case.

Figure 4.37 shows time averaged streamline patterns obtained on the specified streamwise locations for the CFD-CFD configuration for d/Lw= 1 case. Four foci are observed at each of the downstream planes. Even if their size and strength differ as the flow moves downstream, however, they do not interact with each other or with the main flow obviously. At the same time, as the flow moves to the downstream, the center of the focus located at the left part of the domain shifts towards the central region of the domain and this causes the focus formed at the apex of the duct to be weakened.

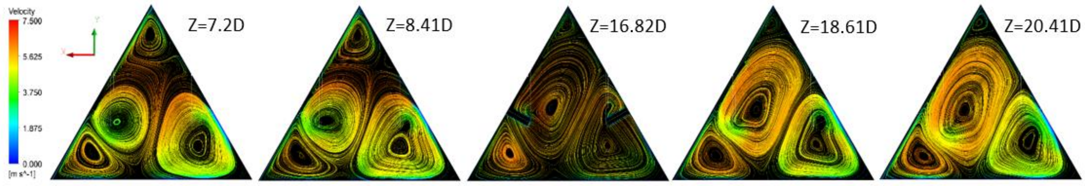

Figure 4.37 Time averaged streamline patterns of CFD-CFD configuration for d/Lw=1 case.

Figure 4.38 shows time averaged streamline patterns obtained on the specified streamwise locations for the CFU-CFD configuration for d/Lw=1 case. There are 2 twin foci centered at the lower and upper part of the y-symmetry axis at each plane. It seems that there is no rotation effect for this case as in the previous case shown in Figure 4.36.

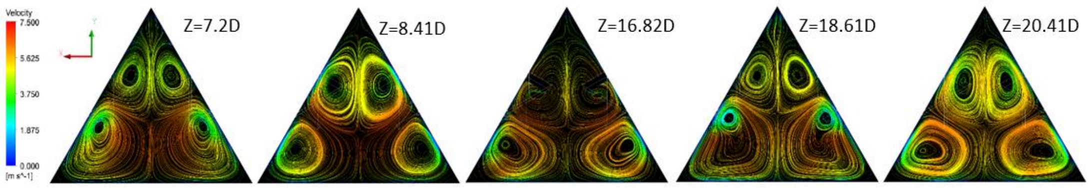

Figure 4.38 Time averaged streamline patterns of CFU-CFD configuration for d/Lw=1 case.

Figure 4.39 shows time averaged streamline patterns obtained on the specified streamwise locations for the CFD-CFU configuration for d/Lw=1 case. Note that foci are scattered throughout each streamwise plane and interaction between the foci are very strong.

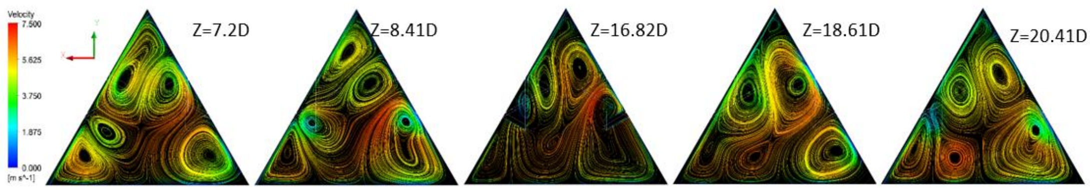

Figure 4.39 Time averaged streamline patterns of CFD-CFU configuration for d/Lw=1 case.

Figure 4.40 illustrates time averaged streamline patterns obtained on the specified streamwise locations for the CFU-CFU configuration for d/Lw= 3 case. It is clear that there is some interaction between the foci formed in the vicinity of the left inclined wall of the duct but the general structure of the foci remains the same as the flow develops to the downstream. A very small corner vortex is observed in the right base corner of the duct at Z=16.82D and Z=18.61D planes.

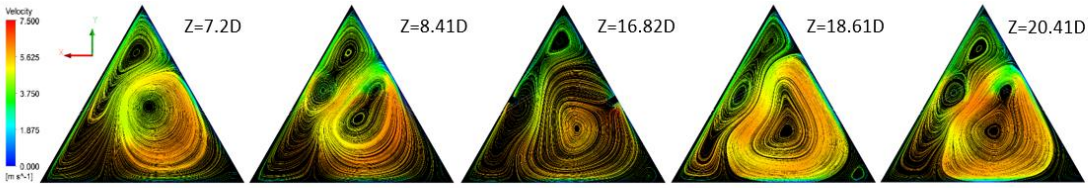

Figure 4.40 Time averaged streamline patterns of CFU-CFU configuration for d/Lw=3 case.

Figure 4.41 illustrates time averaged streamline patterns obtained on the specified streamwise locations for the CFD-CFD configuration for d/Lw=3 case. Although there is some interaction between the foci formed next to the side walls of the duct with the foci located next to them at Z=16.82D plane, generally speaking, the flow mixing is not good for this case.

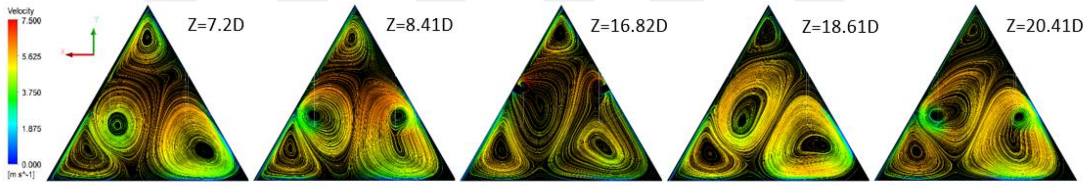

Figure 4.41 Time averaged streamline patterns of CFD-CFD configuration for d/Lw=3 case.

Figure 4.42 illustrates time averaged streamline patterns obtained on the specified streamwise locations for the CFU-CFD configuration for d/Lw=3 case. Flow interaction between the foci is found good especially near the both inclined walls of the duct but there is no interaction with the main flow. This interaction is found better for the CFD-CFU configuration for d/Lw=3 case as illustrated in Figure 4.43.

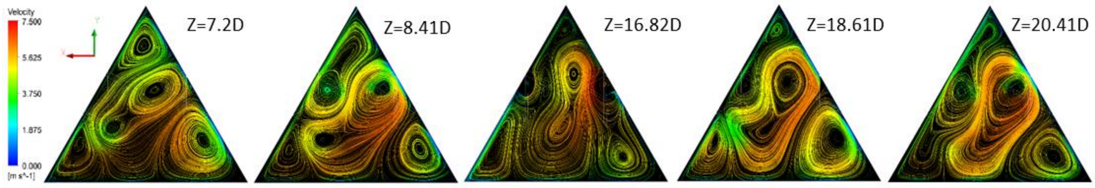

Figure 4.42 Time averaged streamline patterns of CFU-CFD configuration for d/Lw=3 case.

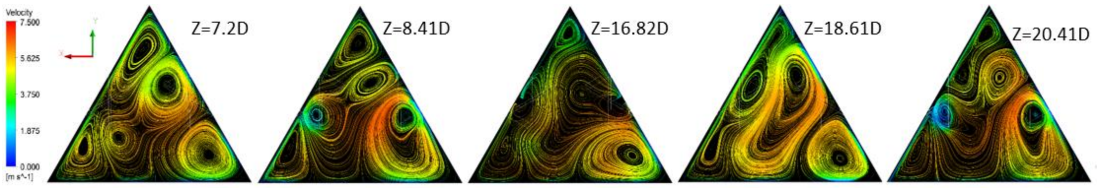

Figure 4.43 Time averaged streamline patterns of CFD-CFU configuration for d/Lw=3 case.

Figure 4.44 illustrates time averaged streamline patterns obtained on the specified streamwise locations for the CFU-CFU configuration for d/Lw=6 case. A very strong focus is located and centered in the right part of each streamwise plane and it grows as the flow moves to the downstream. In the left part of this focus the interaction between the foci is not very strong.

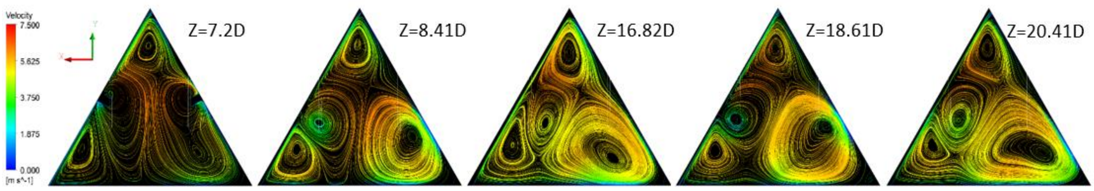

Figure 4.44 Time averaged streamline patterns of CFU-CFU configuration for d/Lw=6 case.

Figure 4.45 and Figure 4.46 illustrate time averaged streamline patterns obtained on the specified streamwise locations for d/Lw=6 case for the CFD-CFD and CFU-CFD configurations, respectively. A large scale focus is observed at each of the streamwise planes for each configuration. However, there is no interaction between this foci except a small scale interaction observed at Z=16.82D for the CFU-CFD configuration. Another interaction is observed between the focus located next to the left side wall of the duct for the CFD-CFD and for the CFU-CFD configurations.

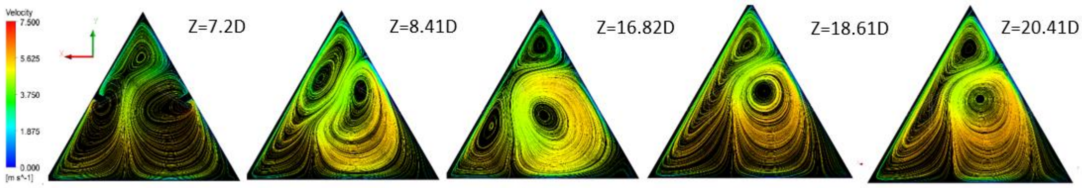

Figure 4.45 Time averaged streamline patterns of CFD-CFD configuration for d/Lw=6 case.

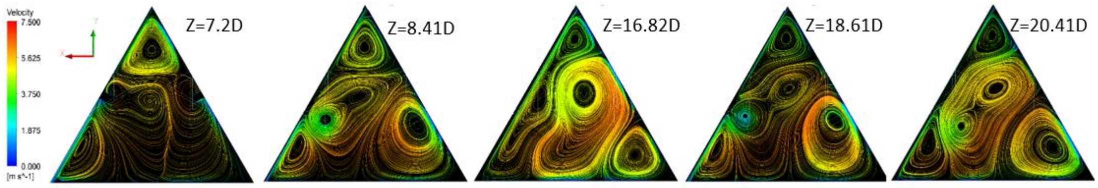

Figure 4.46 Time averaged streamline patterns of CFU-CFD configuration for d/Lw=6 case.

Figure 4.47 illustrates time averaged streamline patterns obtained on the specified streamwise locations for the CFD-CFU configuration for d/Lw=6 case. Again, the large-scale foci interact with each other and there is no interaction with the foci and the main flow.

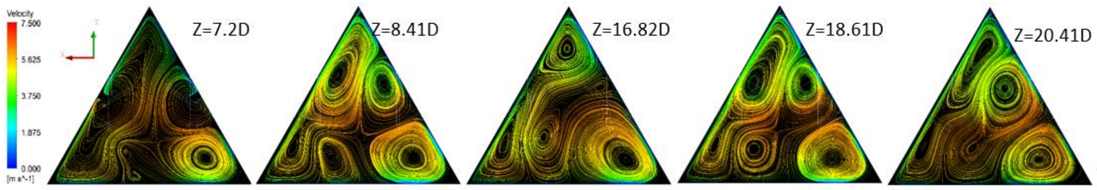

Figure 4.47 Time averaged streamline patterns of CFD-CFU configuration for d/Lw=6 case.

Overall comparison between the cases studied reveals that as the streamwise distance between the VGs (d/Lw) is increased, the flow mixing becomes worse, interaction of the foci formed at each plane weakens and the secondary flow formation almost disappears for each configuration. There is almost no interaction between the foci for the CFU-CFU configuration. CFD-CFD configuration may be better than the CFU-CFU configuration in terms of number and size of the foci formed for each d/Lw case. The strongest secondary flow formation is observed for d/Lw=0 and d/Lw=0.5 cases for both CFU-CFD and CFD-CFU configurations. The flow mixing becomes better as the distance between the VGs is increased from 0 to 0.5 for CFU-CFD and CFD-CFU configurations. If a comparison made between CFU-CFD and CFD-CFU configurations for d/Lw=0.5 case, it can be said that both cases are able to generate secondary flow which causes further enhancement in heat transfer. The fluid mixing is obviously better for the CFD-CFU configuration compared with the CFU-CFD configuration. Therefore, it can be said that more heat can be convected from the hot side walls towards the center and towards the upper corner of the duct for the CFD-CFU configuration.

4.6.2 The Time Averaged Vorticity Distribution

Due to the above considerations and following the results obtained from the previous discussion, the time averaged vorticity contours obtained on the previous streamwise locations for each d/Lw cases for the 4 configurations are illustrated in the following sections. Figure 4.48-Figure 4.51 shows the results obtained on Z=8.41D plane.

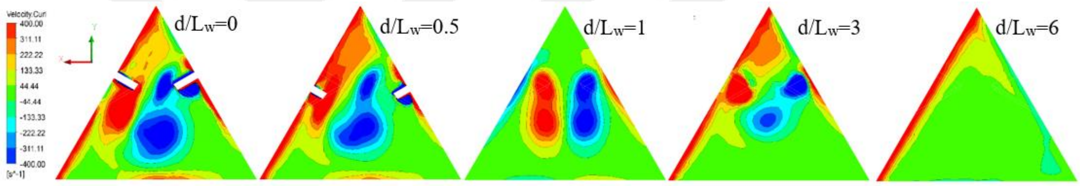

Figure 4.48 Time averaged vorticity contours obtained on Z=8.41D plane for CFU-CFU configuration.

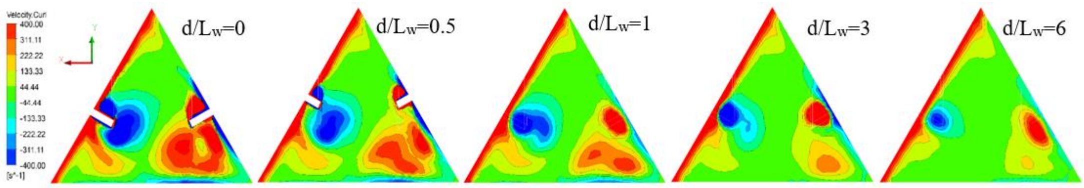

Figure 4.49 Time averaged vorticity contours obtained on Z=8.41D plane for CFD-CFD configuration.

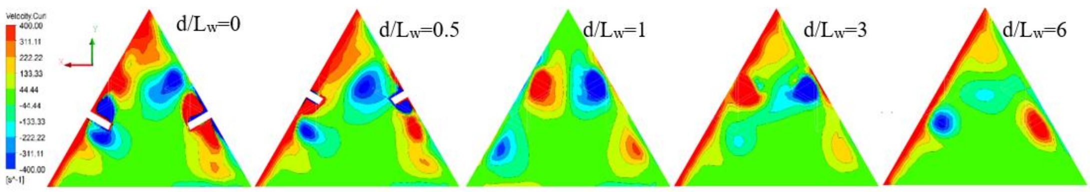

Figure 4.50 Time averaged vorticity contours obtained on Z=8.41D plane for CFU-CFD configuration.

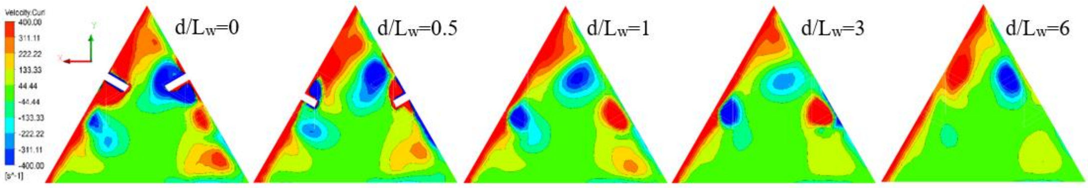

Figure 4.51 Time averaged vorticity contours obtained on Z=8.41D for CFD-CFU configuration.

The vortices are rotating in the counter-clockwise (red colour) and clockwise senses (blue colour). Contour levels are depicted in the legends located in the left part of each figure. It is clear from the figures that the vorticity concentration decreases as d/Lw increases for each configuration as shown in Figure 4.48-Figure 4.51. Due to the direction of rotation, the vorticity concentration becomes maximum on the left side wall of the duct for each configuration except for the CFU-CFU and CFU-CFD configurations for d/Lw=1 case.

For the specified 2 configurations, vortices are found stable as if they are not affected from the rotation of the duct. The vorticity concentration is higher in the left part of the y-symmetry axis and concentrated vortices are connected from the upper side towards the bottom wall of the duct for the CFU-CFU configuration for d/Lw=0 and 0.5 cases as shown in Figure 4.48. The vorticity concentration is stronger in the lower part of the y-symmetry axis compared with the upper part for the CFD-CFD configuration for d/Lw cases (Figure 4.49). However, the vorticity concentration is stronger in the upper part of the y-symmetry axis and in the vicinity of the side walls of the duct for the CFU-CFD and CFD-CFU configurations for each d/Lw cases and convection is from the upper part towards the lower part (Figure 4.50-Figure 4.51). The main conclusion driven from Figure 4.48-Figure 4.51 is that since the flow mixing is the best at the locations where the vortices are mostly concentrated then it can be said that d/Lw=0 and 0.5 cases has more advantages.

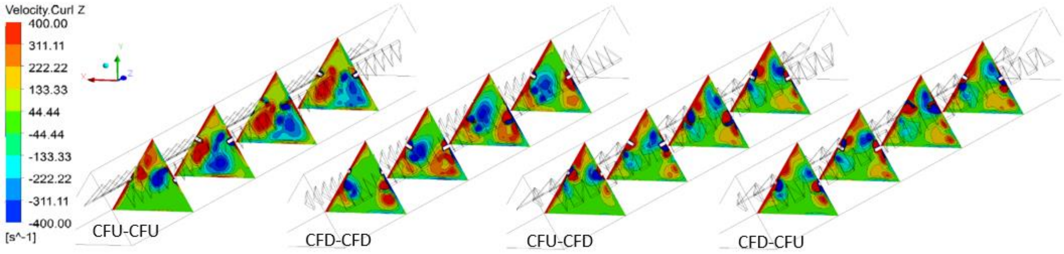

Figure 4.52 Time averaged vorticity contours obtained on Z=5.15D, Z=10.3D, Z=15.45D and Z=20.6 planes d/Lw=0 case.

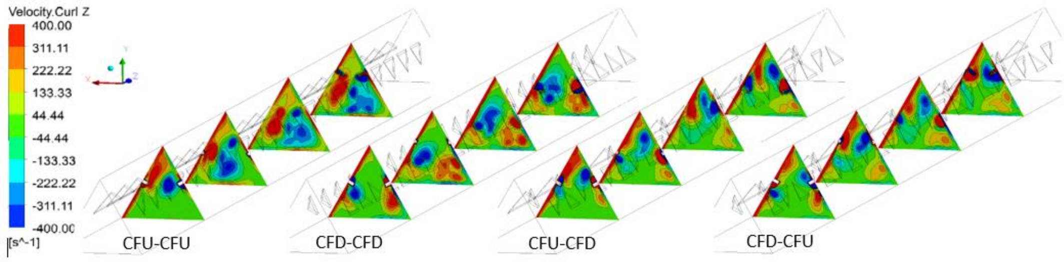

Figure 4.53 Time averaged vorticity contours obtained on Z=5.15D, Z=10.3D, Z=15.45D and Z=20.6 planes d/Lw=0.5 case.

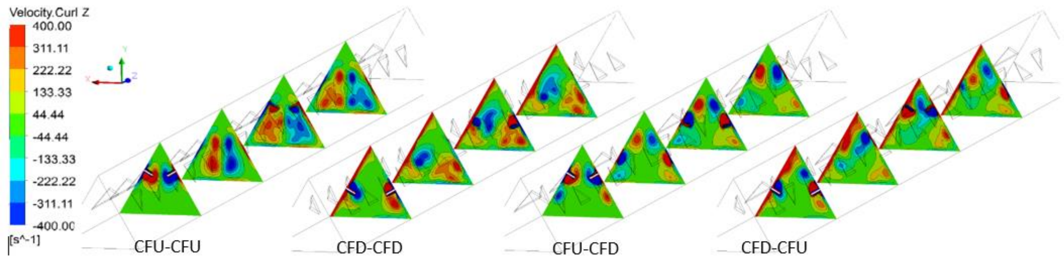

Figure 4.54 Time averaged vorticity contours obtained on Z=5.15D, Z=10.3D, Z=15.45D and Z=20.6 planes d/Lw=1 case.

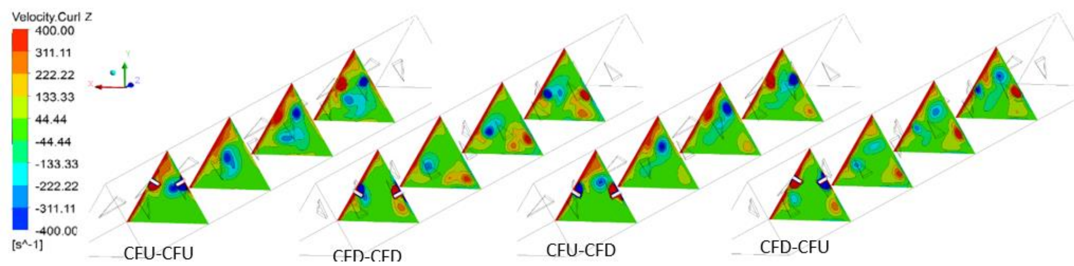

Figure 4.55 Time averaged vorticity contours obtained on Z=5.15D, Z=10.3D, Z=15.45D and Z=20.6 planes d/Lw=3 case.

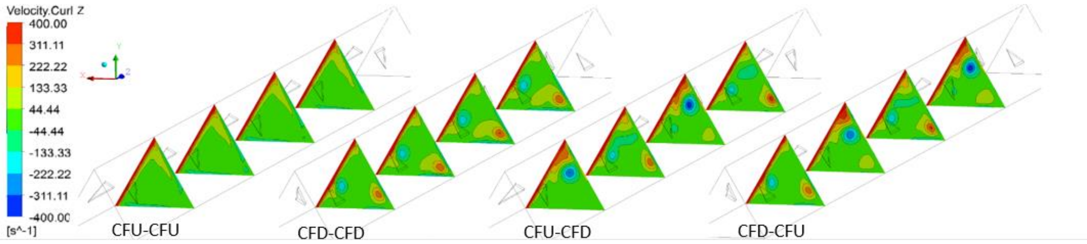

Figure 4.56 Time averaged vorticity contours obtained on Z=5.15D, Z=10.3D, Z=15.45D and Z=20.6 planes d/Lw=6 case.

In order to further investigate the effect of the streamwise distance between the VGs, time averaged vorticity contours obtained at Z=5.15D, Z=10.3D, Z=15.45D and Z=20.6 planes subsequently located in the streamwise direction are shown in Figure 4.52-Figure 4.56. As it is seen in Figure 4.52-Figure 4.55, at the former streamwise locations, there is no interaction of the vortices with the bottom surface of the duct and as the flow moves downstream, the centers of the vortices move towards the base of the duct, allowing good mixing in the lower part of the y-symmetry axis and at the base of the duct for the CFU-CFU configuration for d/Lw=0, d/Lw=0.5, d/Lw=1 and d/Lw=3 cases. This interaction becomes weaker as d/Lw is increased and becomes stronger as the flow moves downstream. For the specified streamwise distances, the vortices are found attached on the duct side walls at the former streamwise positions but as the flow moves to the downstream, these attached vortices starts to move away from the wall and their centers shift towards the center of the duct (Figure 4.52-Figure 4.55). This indicates that mixing of hot and cold fluids is not good for this configuration. No vortices are formed for d/Lw=6 case for the CFU-CFU configuration as can be seen in Figure 4.56.

At the latter streamwise locations, the interaction between the vortices with the base of the duct is found better compared with the former streamwise locations and the vortex formation area is concentrated in the lower part of the y-symmetry axis for each case for the CFD-CFD configuration. Therefore, it can be concluded that the flow mixing is better in the lower part of the y-symmetry axis with this configuration. (Figure 4.52-Figure 4.56).

For the CFU-CFD and CFD-CFU configurations, it can be seen that the vortices are in small scale and are attached on the side walls of the duct at each of the streamwise locations. This form of the vortices is able to allow a better mixing characteristic between the side walls and the inner part of the duct. Therefore, the interaction of vortices with the main flow may be more dominant with these 2 configurations. Like in the other configurations, the vortices become weaker as the distance between the VGs is increased (Figure 4.52-Figure 4.56).

As a conclusion, at each case and at each streamwise distance, the size of the vortices is always bigger for the CFU-CFU and CFD-CFD configurations compared with the CFU-CFD and CFD-CFU configurations. Considering the above-discussed vortex location area, CFU-CFD and CFD-CFU configurations may allow a better mixing characteristic since the vortices are of small scale and remains attached to the duct walls allowing more heat is transferred from the side walls towards the inner part of the duct. The vortices are stronger for d/Lw=0, d/Lw=0.5 cases and the vortex strength is much lower and mixing becomes worse as d/Lw increases as shown in Figure 4.52-Figure 4.56.

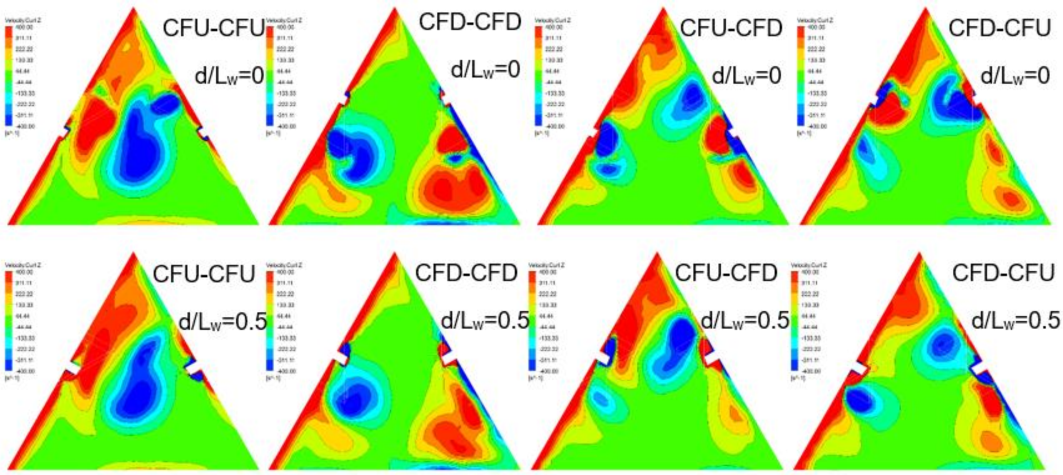

Figure 4.57 Time averaged vorticity contours obtained on Z=7.2D plane.

Because the most concentrated vortices are formed for d/Lw=0 and d/Lw=0.5 cases for the 4 VG configurations, the vorticity contours obtained on different sections of the flow domain are investigated more deeply to find the best case and configuration in terms of vortex interaction. The obtained results on Z=7.2D plane are presented in Figure 4.57. At this streamwise plane, it is seen that the size of the vortices are much bigger for the CFU-CFU and CFD-CFD configurations comparing to the CFU-CFD and CFD-CFU configurations for each of the d/Lw cases. The strongest interaction with the vortices located at the bottom of the duct is the CFD-CFD configuration for each of the d/Lw cases. But a dead flow zone appears in the upper part of the y-symmetry axis for the CFD-CFD configuration. For d/Lw=0 case, the number of vortices formed in the specified plane is more for the CFU-CFD and CFD-CFU configurations, compared with the other ones. The vortices are mostly concentrated in the vicinity of the side walls and in the apex region of the duct for the CFU-CFD and CFD-CFU configurations and in the lower part of the y-symmetry axis for the CFD-CFD configuration. The convection of the concentrated vortices from the side walls towards the bottom surface of the duct is found better for the CFD-CFD and CFD-CFU configurations for each cases studied which is an indication of stronger local fluid mixing can occur with these configurations. Below figures, clearly seen that the vorticity contours obtained at further downstream locations.

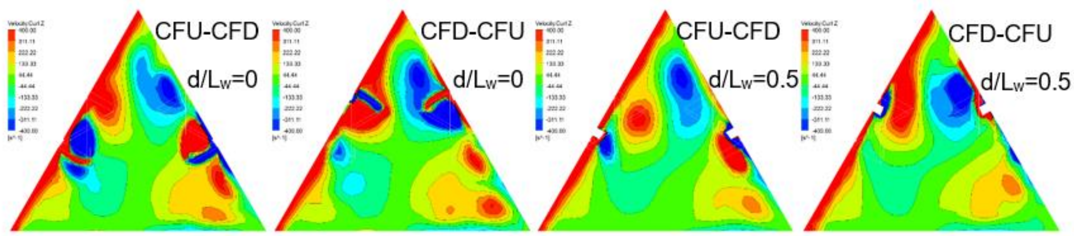

Figure 4.58 Time averaged vorticity contours obtained on Z=10.82D plane.

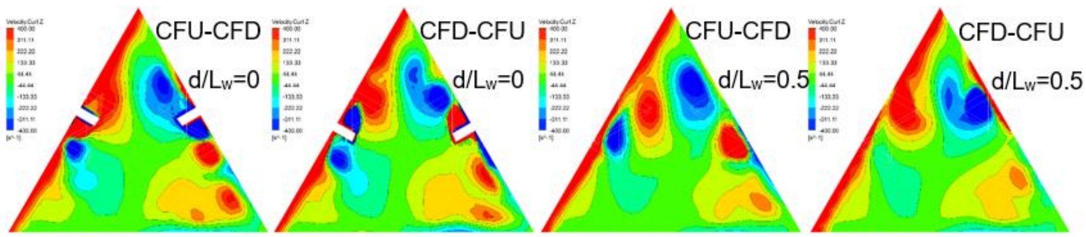

Figure 4.59 Time averaged vorticity contours obtained on Z=18.61D plane.

Figure 4.58-Figure 4.59 show time averaged vorticity contours obtained on Z=10.82D and Z=18.61 planes, respectively, for d/Lw=0 and d/Lw=0.5 cases. At this further streamwise locations, the vortex interaction is found stronger than the former location shown in Figure 4.58 at each case. However, in these local planes, d/Lw=0 case seems better than the d/Lw=0.5 case in terms of larger area of the vorticity concentration and a better interaction between the vortices especially in the lower part of the y-symmetry axis and at the base of the duct.

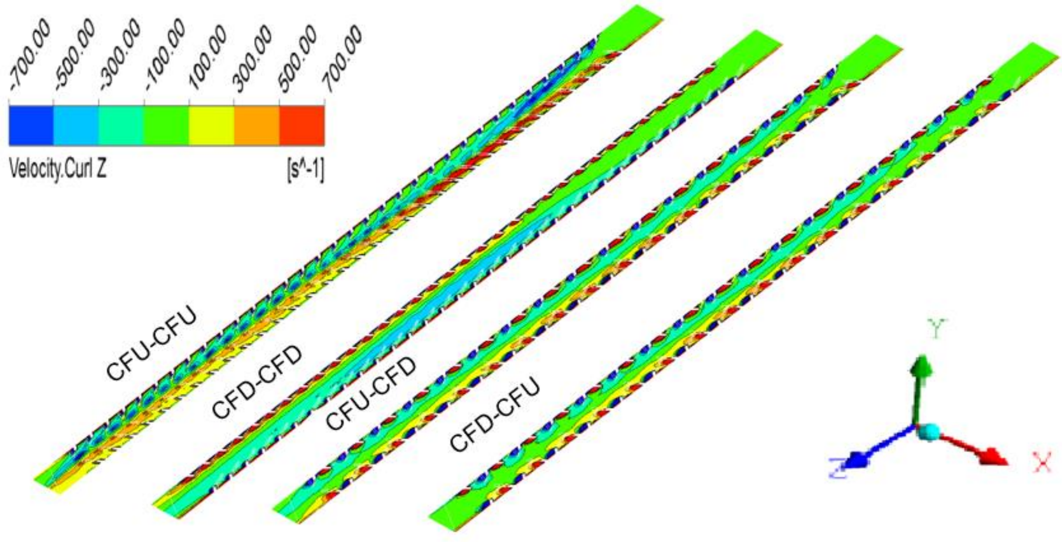

Figure 4.60 Time averaged vorticity contours obtained on Y=0.77D plane for d/Lw=0 case.

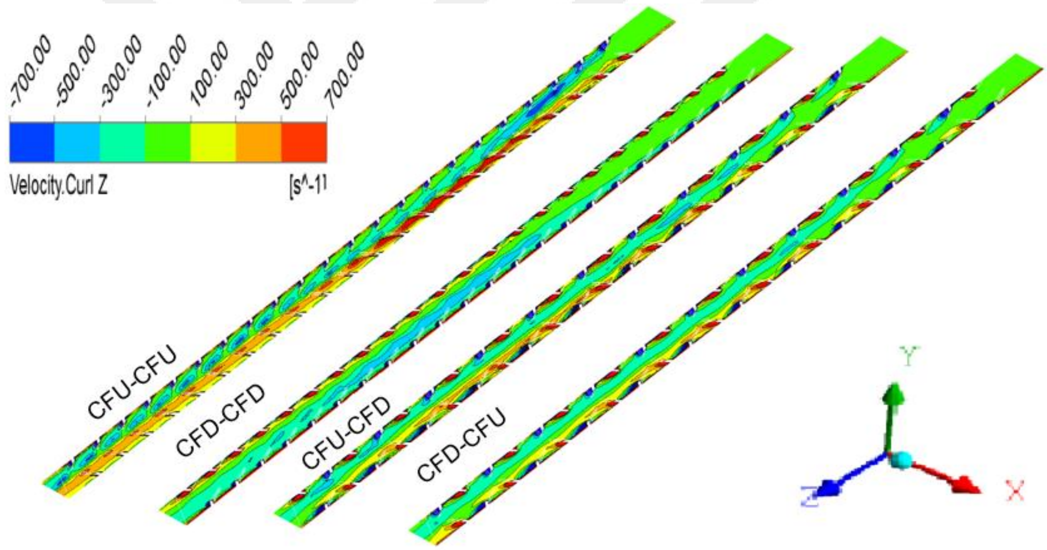

Figure 4.61 Time averaged vorticity contours obtained on Y=0.77D plane for d/Lw=0.5 case.

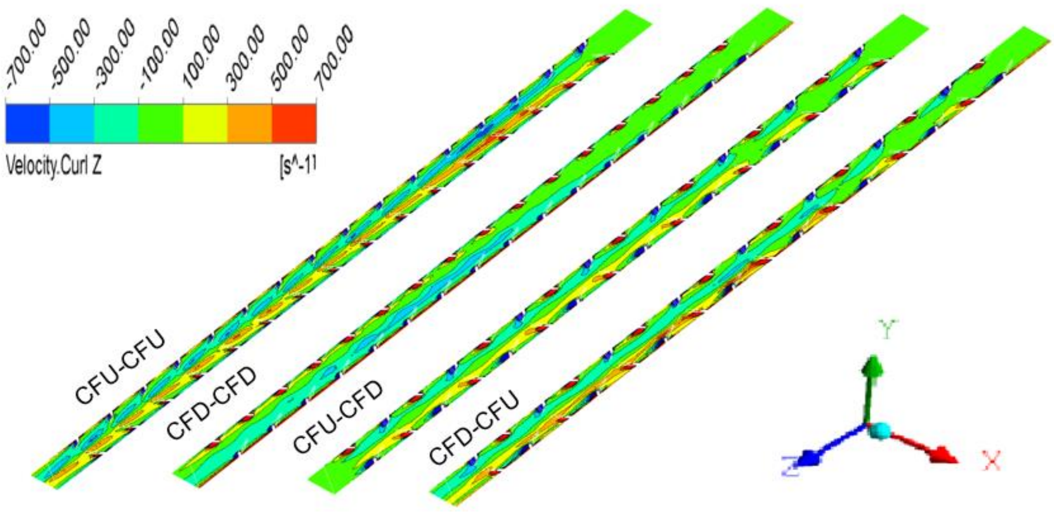

Figure 4.62 Time averaged vorticity contours obtained on Y=0.77D plane for d/Lw=1 case.

In addition to the investigated local streamwise planes, the vorticity distributions obtained along the duct are shown below. Figure 4.60-Figure 4.62 show the vorticity contours obtained in the middle of the duct, on Y=0.77D plane for d/Lw=0, d/Lw=0.5 and d/Lw=1 cases, respectively. The flow is in the z-direction. As the flow moves downstream, the strength of the vortices decreases and the concentrated vortices move towards the central region of the duct for each d/Lw cases for the CFU-CFU configuration as shown in Figure 4.60-Figure 4.62. Note that the sizes of the vortices are very small and the vortices are located just next to the side walls of the duct without showing any movement in each d/Lw cases for the CFD-CFD configuration as shown in Figure 4.60-Figure 4.62. However, the vortices are stronger and the vortex interaction with the main flow is better for the CFU-CFD and CFD-CFU configurations as shown in Figure 4.60-Figure 4.62. The strength of the vortices and the vortex interaction with the main flow becomes better for d/Lw=0 and d/Lw=0.5 cases.

Following the above discussions, it can be concluded that CFU-CFD and CFD-CFU configurations are better than the CFU-CFU and CFD-CFD configurations in terms of vortex formation area, vortex strength and vortex interaction which means that a stronger mixing and therefore, better heat transfer characteristics can be obtained with the former configurations. In terms of vortex strength and both global local mixing ability of the generated vortices with the cases studied, it is found that d/Lw=0 and d/Lw=0.5 cases has more advantages than the other cases.

4.6.3 The Time Averaged Turbulence Kinetic Energy

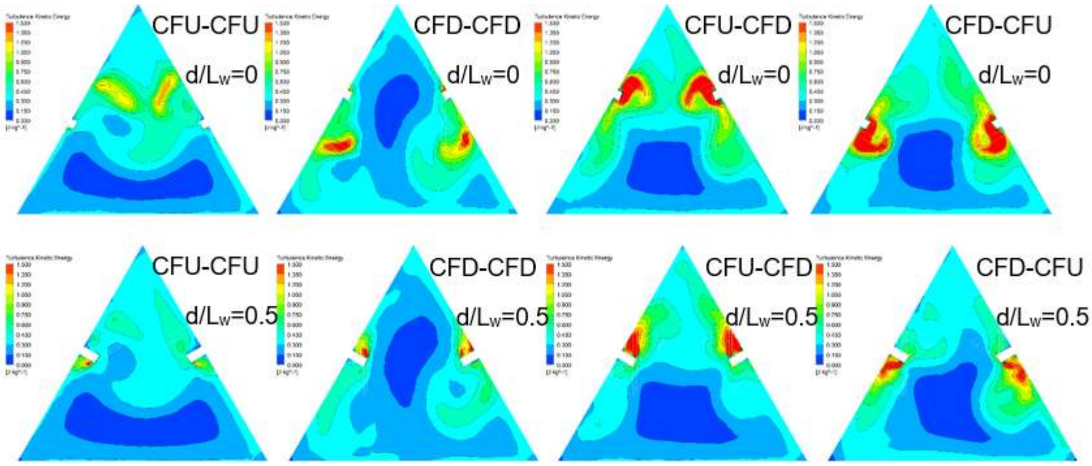

Figure 4.63 Time averaged turbulence kinetic energy contours obtained on Z=5.15D plane for d/Lw=0 and d/Lw=0.5 cases for CFU-CFD and CFD-CFU configurations.

To help finding the better configuration and case, Turbulance Kinetic Energy (TKE) distributions obtained on Z=5.15D plane are illustrated in Figure 4.63. As can be clearly seen from Figure 4.63, the highest values of TKE are concentrated in the vicinity of the side walls, behind each VG pair. The highest TKE contours are obtained for the CFU-CFD and CFD-CFU configurations compared with CFU-CFU and CFD-CFD configurations. The CFU-CFU configuration with d/Lw=0 case is able to generate some increase in the TKE values towards the inner part of the duct above the y-symmetry axis but below this axis the TKE levels are much less. For the CFD-CFD configuration the lowest TKE contours are located in the inner region of the duct and high TKE region is only seen next to the slant walls. These results confirm the results obtained in Figure 4.60-Figure 4.62 since the vorticity concentration moves towards the inner section of the duct for the CFU-CFU configuration and remains attached on the duct walls for the CFD-CFD configuration. Among the 4 configurations, the highest TKE contours are obtained for the CFU-CFD and CFD-CFU configurations. Comparison of the latter two configurations reveals that the minimum TKE values (blue region) cover a smaller portion of the duct and also TKE is higher at the base of the duct for the CFD-CFU configuration compared with the CFU-CFD configuration for both d/Lw=0 case and d/Lw=0.5 cases. Since the locations of high TKE area correspond to the enhanced flow mixing regions, therefore it can be concluded that the CFD-CFU configuration is better than the other cases.

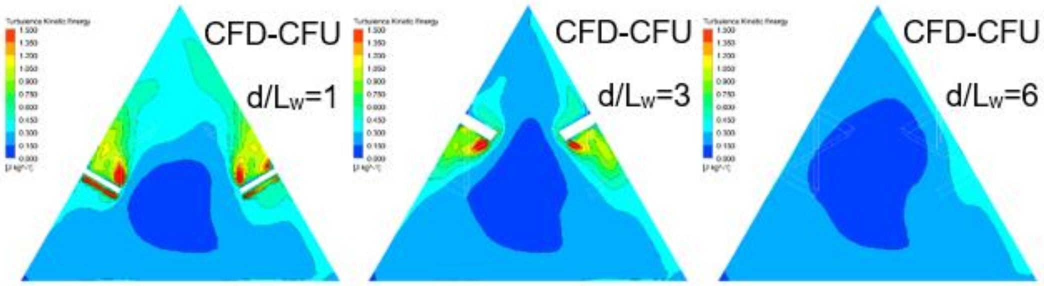

Figure 4.64 Time averaged turbulence kinetic energy contours obtained on Z=5.15D plane for d/Lw=1, 3 and 6 cases for the CFD-CFU configurations.

To investigate the effect of d/Lw on the TKE distribution, TKE contours obtained for d/Lw=1, d/Lw=3 and d/Lw=6 cases for the CFD-CFU configuration is illustrated in Figure 4.64. Since the formation of low region of TKE increases with an increase in d/Lw, then it is clear that increasing the non-dimensional streamwise distance lowers the ability of flow mixing and as a result decreasing the heat transfer.

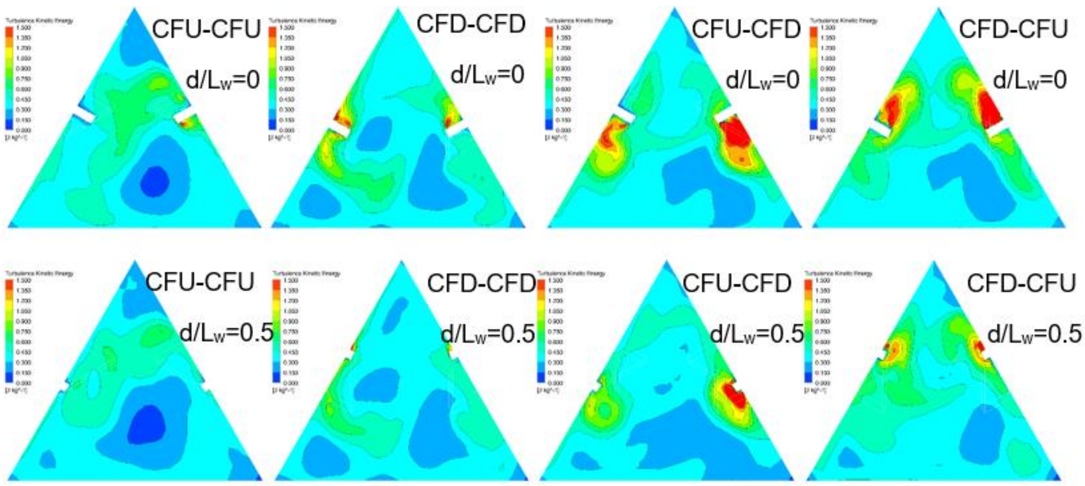

Figure 4.65 Time averaged turbulence kinetic energy contours obtained on Z=10.3D plane.

Above discussion demonstrates that d/Lw=0 and d/Lw=0.5 cases have the ability of better mixing and as a result a better heat transfer. Therefore, in order to select the best configuration and the best distance between the VGs, TKE distribution obtained for the 4 configurations for d/Lw=0 and d/Lw=0.5 cases are shown in Figure 4.65 at a further downstream location, at Z=10.3D plane. It is obvious from this figure that CFU-CFD and CFD-CFU configurations with d/Lw=0 and d/Lw=0.5 cases have better ability in terms of turbulence generation than the other cases. Also note that the minimum contour levels (blue region) becomes much less for CFD-CFU configuration with d/Lw=0.5 case and therefore this case is the best one compared with the other cases studied in this local plane. This best combination is still having the best ability of mixing at a further downstream location, on Z=15.45D plane, as shown in Figure 4.66.

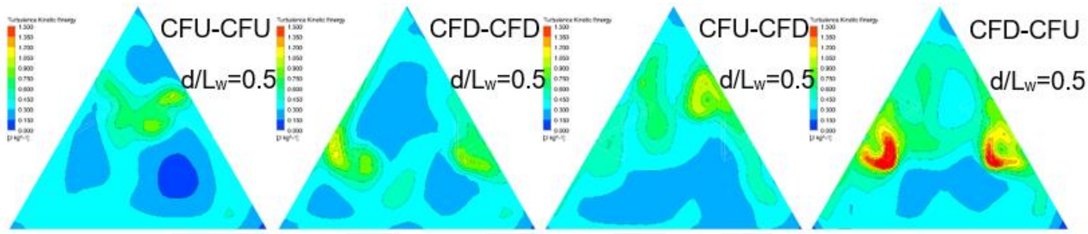

Figure 4.66 Time averaged turbulence kinetic energy contours obtained on Z=15.45D plane.

In order to broaden our discussion on selection of the best configuration and case, time averaged TKE contours on Y=0.77D plane for d/Lw=0, d/Lw=0.5 and d/Lw=1 cases are shown in Figure 4.67-Figure 4.69. The flow is perpendicular to plane (z-direction).

For d/Lw=0 case, the TKE values are small between the inlet and the middle of the duct and it slightly increases towards the end of the duct for the CFU-CFU configuration. The CFD-CFD configuration is the worst configuration in terms of TKE generation. The TKE generation is again better for the CFU-CFD and CFD-CFU cases. However, the CFD-CFU configuration is better since it has smaller low region of TKE as shown in Figure 4.67.

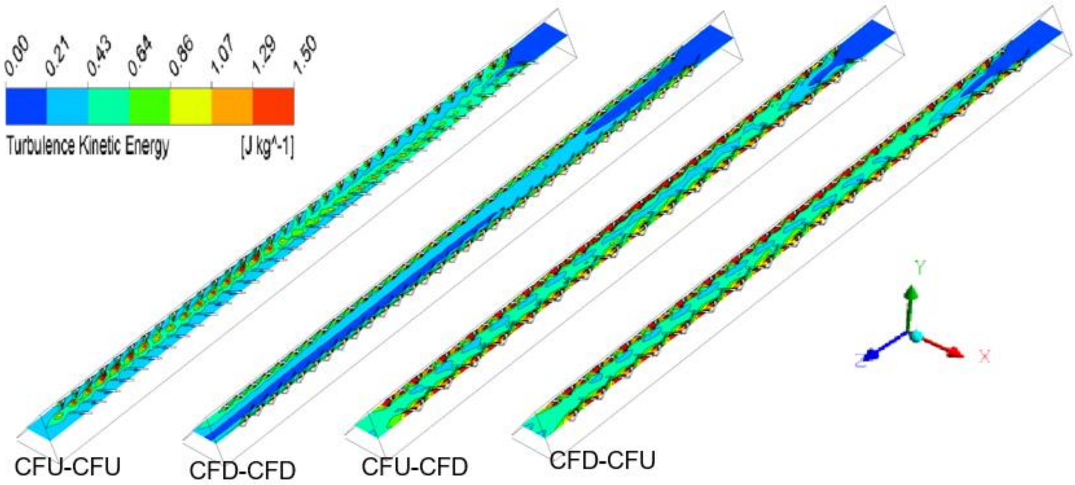

Figure 4.67 Time averaged turbulence kinetic energy contours obtained on Y=0.77D plane, for d/Lw=0 case.

The mixing characteristics become better for d/Lw=0.5 case for each configuration as shown in Figure 4.68. Again, the worst configuration is the CFD-CFD configuration. It is observed that high TKE regions are mostly concentrated along the side walls of the duct for the CFU-CFD configuration. However, high TKE regions are distributed towards the center of the duct instead of remaining attached to the side walls, which allows a better mixing between the side walls and inner section, for the CFD-CFU configuration.

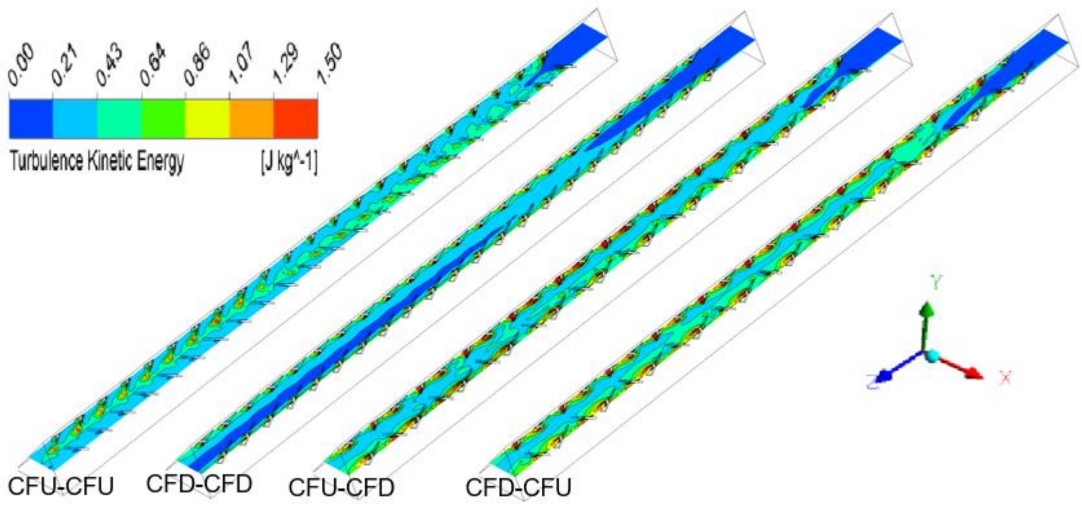

Figure 4.68 Time averaged turbulence kinetic energy contours obtained on Y=0.77D plane for d/Lw=0.5 case.

As the distance between the VGs is increased to a value of d/Lw=1, the fluid mixing between the hot side walls and the inner section of the duct becomes worse as it is clearly seen in Figure 4.69 and therefore, d/Lw=1 case is not recommended.

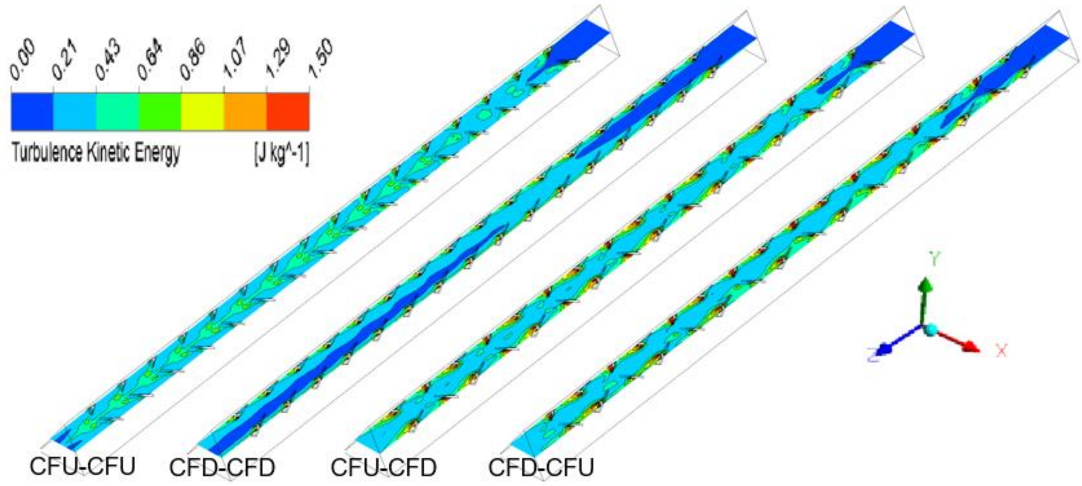

Figure 4.69 Time averaged turbulence kinetic energy contours obtained on Y=0.77D plane for d/Lw=1 case.

In addition to the local planes and at the middle of the duct, it is thought to investigate TKE distribution on the duct base for d/Lw=0, d/Lw=0.5 and d/Lw=1 cases. Figure 4.70 and Figure 4.72 shows the time averaged turbulence kinetic energy contours obtained on the base of the duct for the 4 configurations. The kinetic energy level in the duct base is higher for the CFU-CFU and CFD-CFD configurations compared with the CFU-CFD and CFD-CFU configurations for d/Lw=0 case (Figure 4.70). But it decreases significantly as the flow moves to the downstream direction. The kinetic energy distribution is significantly altered as d/Lw is increased from 0 to 1 as shown in Figure 4.70 and Figure 4.72. It can be said that the highest TKE level is obviously obtained for the CFD-CFU configuration for d/Lw=0.5 case (Figure 4.71). The TKE distribution becomes worse for d/Lw=1 case for each configuration (Figure 4.72).

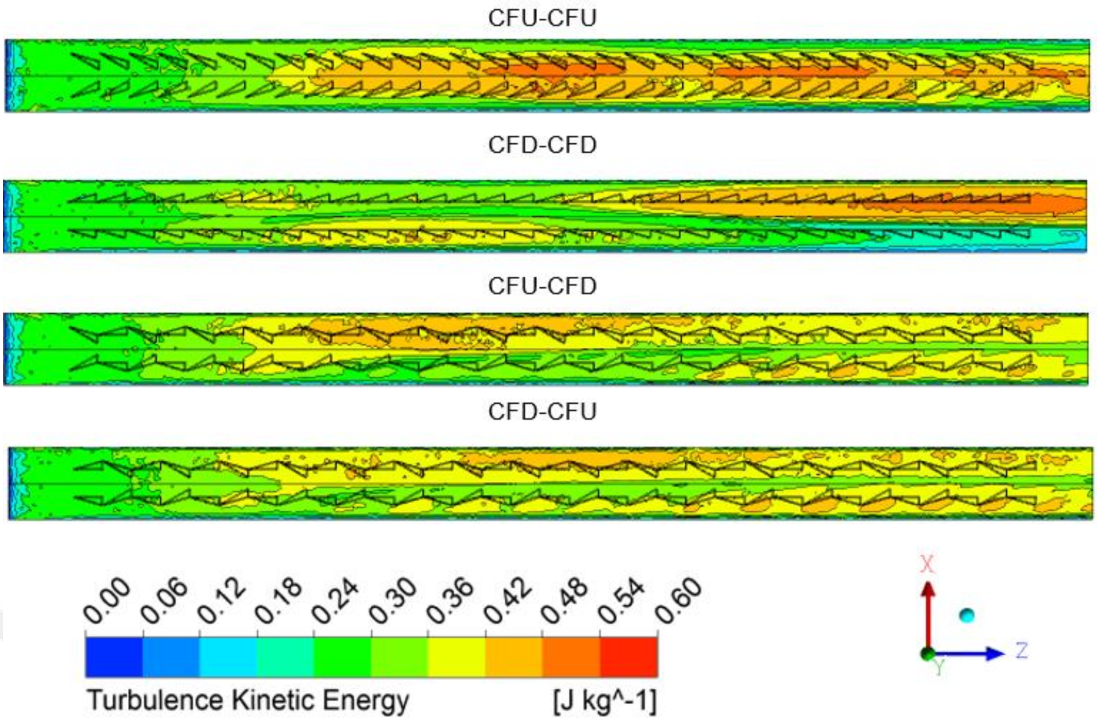

Figure 4.70 Time averaged turbulence kinetic energy contours obtained on the duct base for d/Lw=0 case.

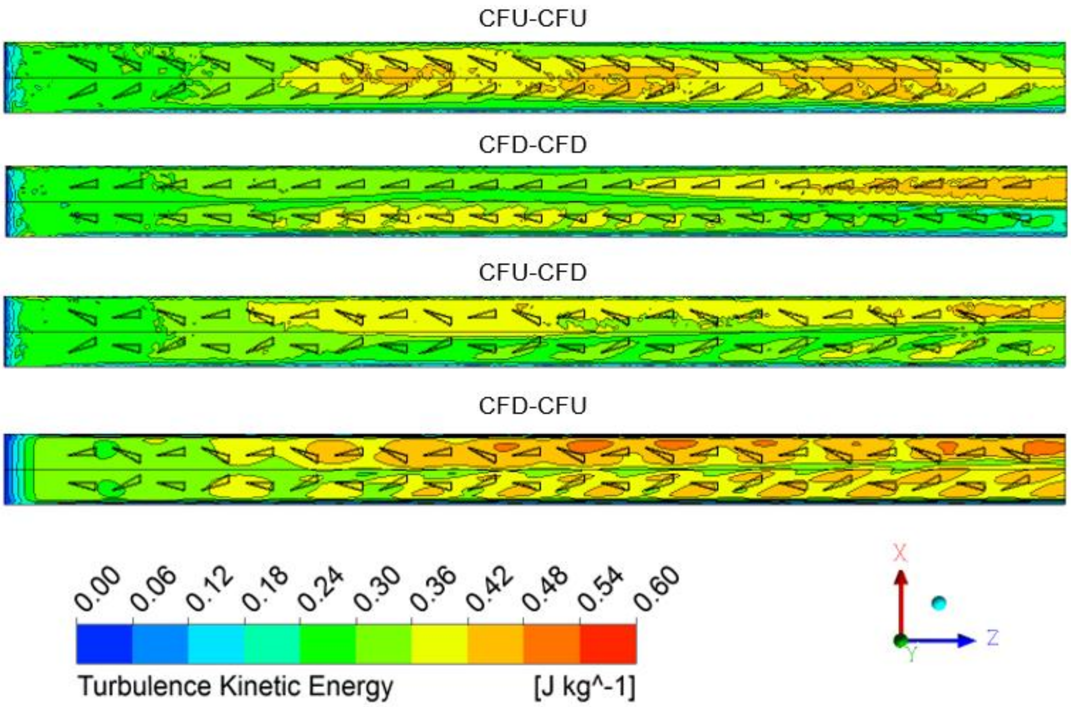

Figure 4.71 Time averaged turbulence kinetic energy contours obtained on duct base for d/Lw=0.5 case.

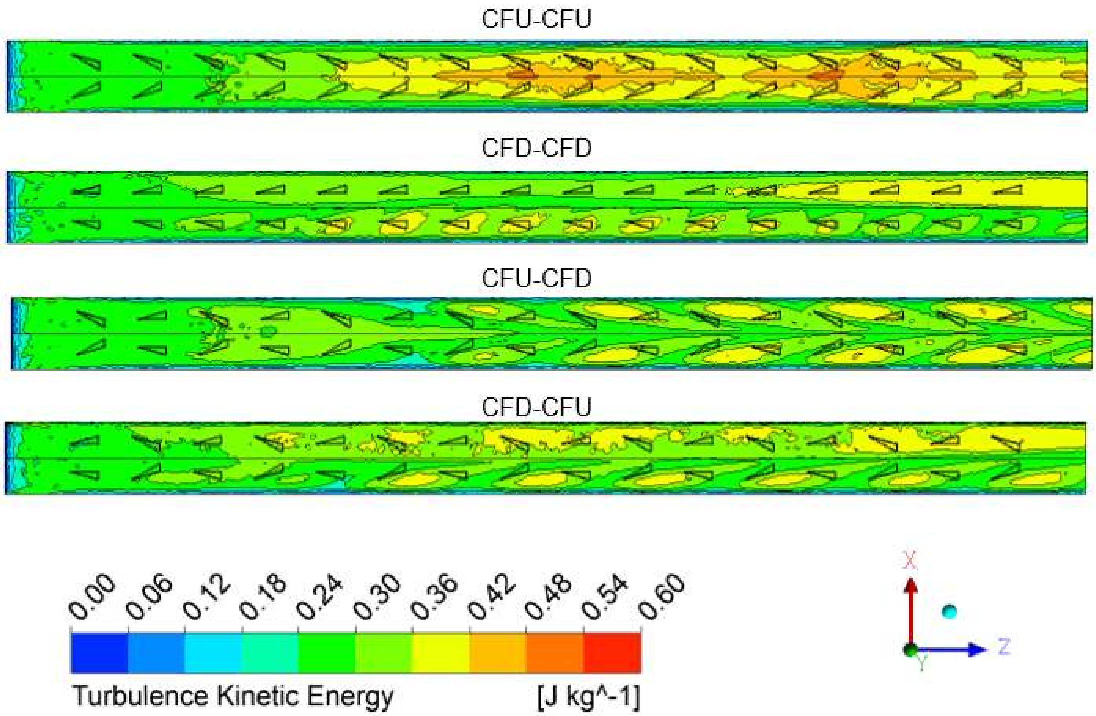

Figure 4.72 Time averaged turbulence kinetic energy contours obtained on the duct base for d/Lw=1 cases.

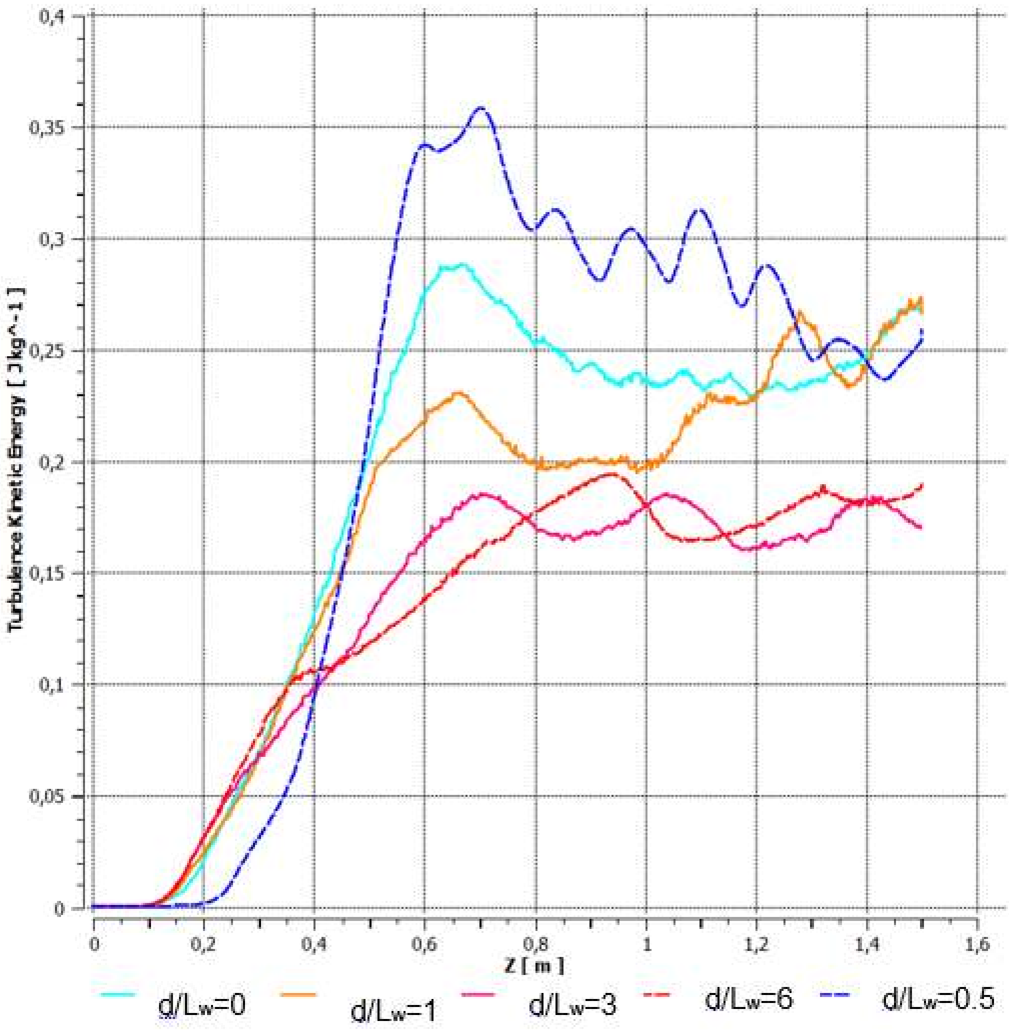

Figure 4.73 Turbulence kinetic energy distribution along the z-axis on line L1 (X=0.86D, Y=0.34D) for the CFD-CFU configuration.

Figure 4.73 shows turbulence kinetic energy distribution along the z-axis on line L1 for the CFD-CFU configuration. Line L1 is located at X=0.86D, Y=0.34D. It is observed that TKE is equal to zero near the inlet section of the duct for all the cases studied. Between 0.2 m $\leq$ Z $\leq$ 0.4 m all the TKE values are approximately equal to each other except d/Lw=0.5 case. This case has the lowest TKE values compared with the other cases between 0.2 m $\leq$ Z $\leq$ 0.4 m. After Z=0.4 m, the behavior of TKE for each case differs and TKE becomes maximum for d/Lw=0.5 case. It is obvious that the fluid mixing effect becomes weaker as d/Lw decreases and mixing effect is the best for the d/Lw=0.5 case.

4.6.4 The Time Averaged Velocity Swirling Strength

It is known that the mixing ability is strongly related to the velocity swirling strength. The distribution of swirling strength helps understanding of vertical flow pattern, vortex population and vortex motion development and size and strength of the vortices formed. Figure 4.74-Figure 4.76 show the time averaged velocity swirling strength contours obtained on Z=5.15 D, Z=10.3 D and Z=15.45 D planes, respectively. In each of these figures, it is obvious that both configuration and distance between the VGs affect the swirling strength in the flow domain and the maximum peak in the velocity swirling strength occurs in the vicinity of the VGs. At the same time, the vortex population is farther for the CFU-CFD and CFD-CFU configurations for d/Lw=0 and d/Lw=0.5 cases compared with the other configurations, see Figure 4.74 and Figure 4.75. In addition, vortex motion is found better for the CFU-CFD and CFD-CFU configurations than the CFU-CFU and CFD-CFD configurations as shown in Figure 4.74 and Figure 4.75. Even if the size of the vortices is smaller for the former configurations, they are obviously stronger, and their effective area is much larger than the latter cases as clearly seen in Figure 4.74 and Figure 4.75. The vortices still conserve their strength and population density as the flow moves further downstream (Figure 4.76). At Z=15.45 D location, the vortex population decreases for the CFU-CFD configuration. However, both the strength of the vortices and the vortex population is still better for the CFD-CFU configuration at this farther downstream location.

Summarizing the above discussions, it can be said that the population density, size and swirling strength of the vortices depends strongly to the distance between the VGs as well as the VG configuration and there is a strong foresight about the optimum case to be the CFD-CFU configuration for d/Lw=0.5 case since the maximum swirling strength and maximum population density of the vortices are obtained for this case and configuration, even at farther downstream locations.

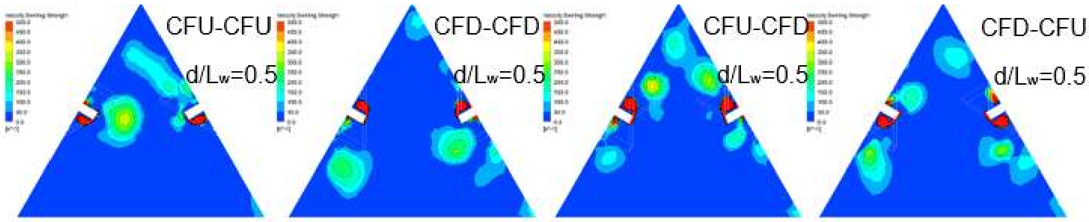

Figure 4.74 Time averaged velocity swirling strength contours obtained on Z=5.15D plane

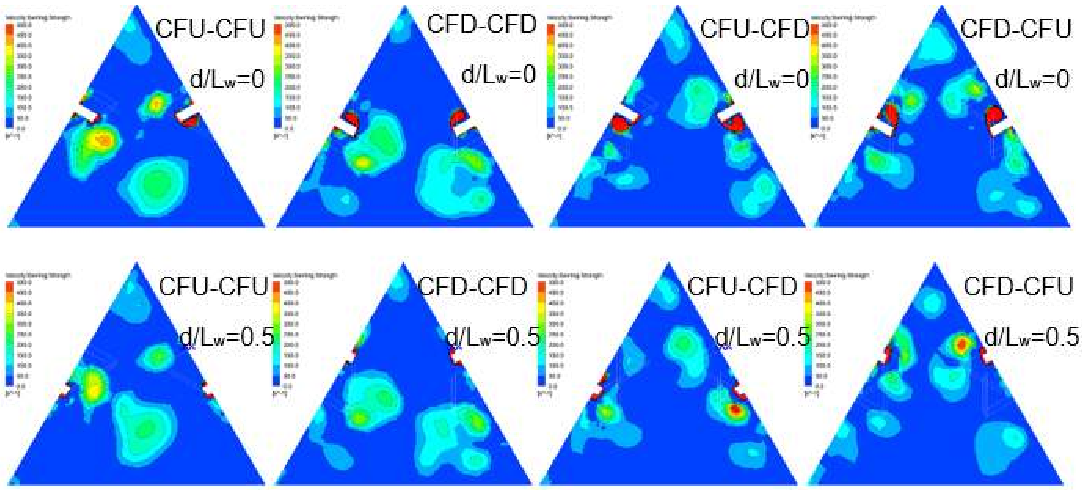

Figure 4.75 Time averaged velocity swirling strength contours obtained on Z=10.3D plane.

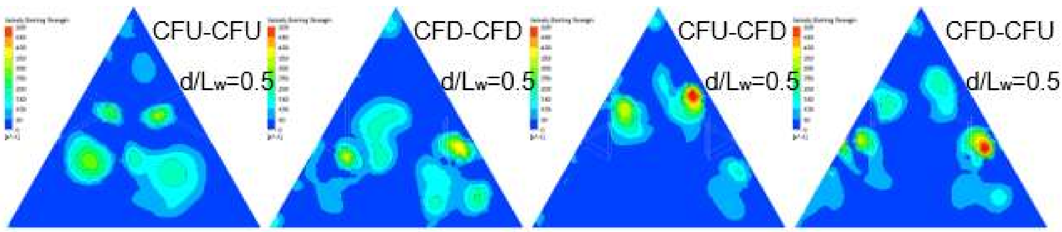

Figure 4.76 Time averaged velocity swirling strength contours obtained on Z=15.45D plane.

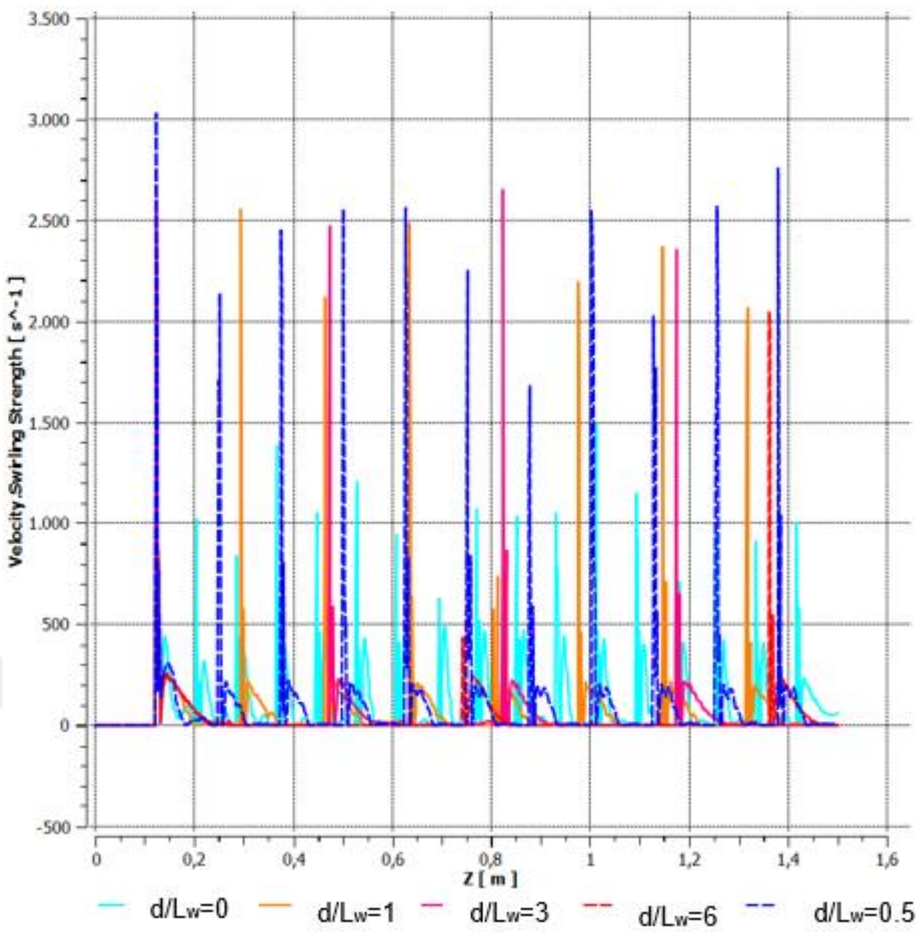

Figure 4.77 Velocity swirling strength distribution along the z-axis on line L2 (X=0.86D, Y=0.83D) for the CFD-CFU case.

In order to broaden the above discussion, velocity swirling strength obtained on line L2 is shown in Figure 4.77. The main objective is to examine the effect of d/Lw on the vortex structure and strength of the vertical motion. Each d/Lw case generates large and small peaks, indicating a vortex, on the specified location. Each generated peak is associated with the presence of a VG pairs. It can be said that the population density, size and swirling strength of the vortices depends strongly to the distance between the VGs, as shown in Figure 4.77. As the flow reaches the location aligned with the leading edge of VG pairs, swirling strength increases sharply and a maximum peak is obtained at this location. Then as the flow encounters the location aligned with the trailing edge of VG pairs, swirling strength sharply decreases. After that a second peak in the swirling strength appears as the flow reaches the location aligned with the leading edge of the oncoming VG pairs. The swirling strength takes its lowest value on the location, just in-between the VG pairs. As the VG pairs are periodically located in the flow domain, this behavior of the vortices periodically reproduces itself along the specified line.

The velocity swirling strength describes the strength of the local swirling motion inside the vortex as well as the inner structure of the vortex and it is used to determine local intensity and the vortex trajectory of the swirling motion. It is interesting to note that d/Lw=0 case was chosen as the best case in some of the above discussions. However, the strength of the vortices generated with this case is very small and in some locations it is even smaller than all the cases studied. Even if the population density of vortices is obtained as the highest for d/Lw=0 case, as a result of the largest number of VGs used in this case, however, with this case, the strength of the vortices formed is smaller than the other cases. The most striking difference between cases studied is that; d/Lw=0.5 case shows better characteristics in terms of strength of the vortices generated since a number of maximum peaks are obtained up to 3000 s^{-1} for d/Lw=0.5 case. Summarizing the above discussions, it can be said that the population density, size and swirling strength of the vortices depend strongly to the distance between the VGs and there is a strong foresight about the optimum case to be d/Lw=0.5 case since the maximum swirling strength is obtained for this case.

4.6.5 The Time Averaged Pressure Distribution

Above examinations focused on various flow data including streamlines, vorticity contours, velocity swirling strength, turbulence kinetic energy obtained in the flow domain. In Figure 4.78, pressure distribution obtained on Z=5.15D plane for d/Lw= 0, d/Lw= 0.5 and d/Lw=1 cases for the 4 configurations studied is shown. Note that the pressure strongly depends on both the VG configuration and on the streamwise distance between the VGs. The highest pressure contours are obtained for the CFU-CFD and CFD-CFU configurations for d/Lw=0 case and the lowest pressure contours are obtained for the CFU-CFU configuration for each cases studied. It is observed that the pressure distribution becomes smaller as d/Lw decreases for each configuration. The high pressure values are always concentrated in the vicinity of the VG pairs except for d/Lw=1 case. Since high pressure values lead to an increase the pressure drop between the inlet and outlet sections of the domain, then it has a significant effect on the thermo-hydraulic performance of the system and therefore in this respect high pressure is not recommended. It is obviously seen that the high pressure is caused by increasing the number of the VGs as the maximum number of VGs applies for d/Lw=0 case. Comparison between pressure and TKE contours obtained on Z=5.15D plane reveals that the locations of the maximum TKE correspond to the locations of minimum pressure (Figure 4.78 and Figure 4.63).

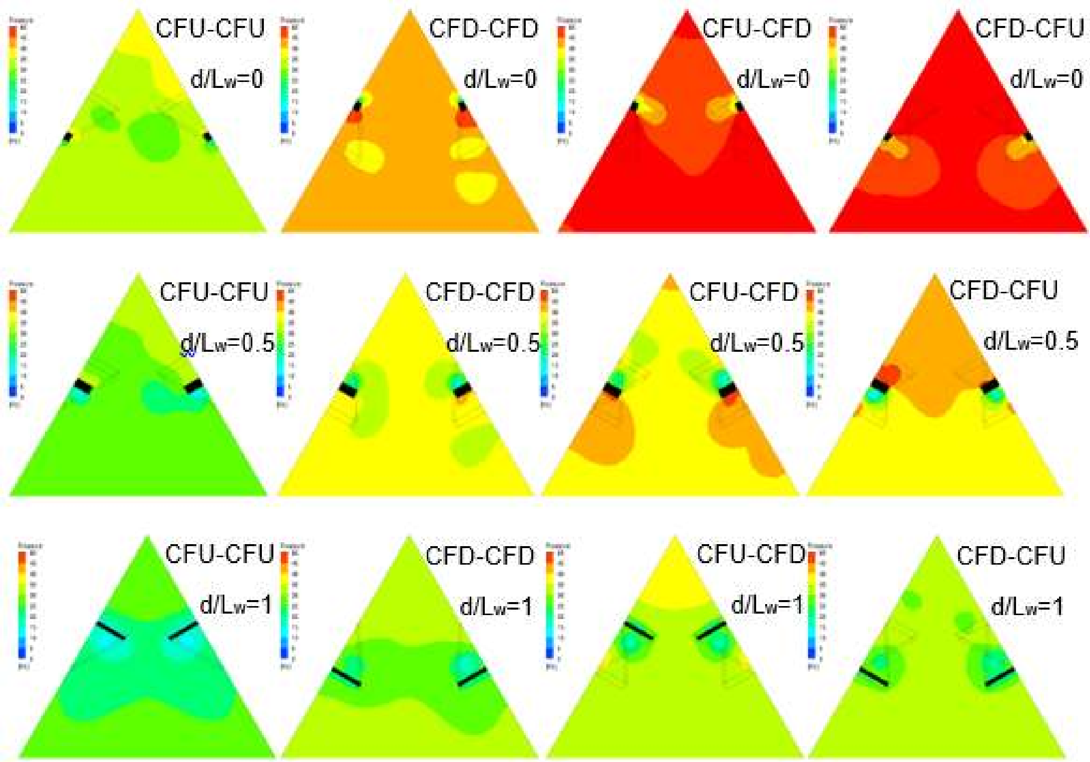

Figure 4.78 Time averaged pressure contours obtained on Z=5.15D plane.

4.6.6 The Time Averaged Heat Transfer, Temperature and Wall Shear Data

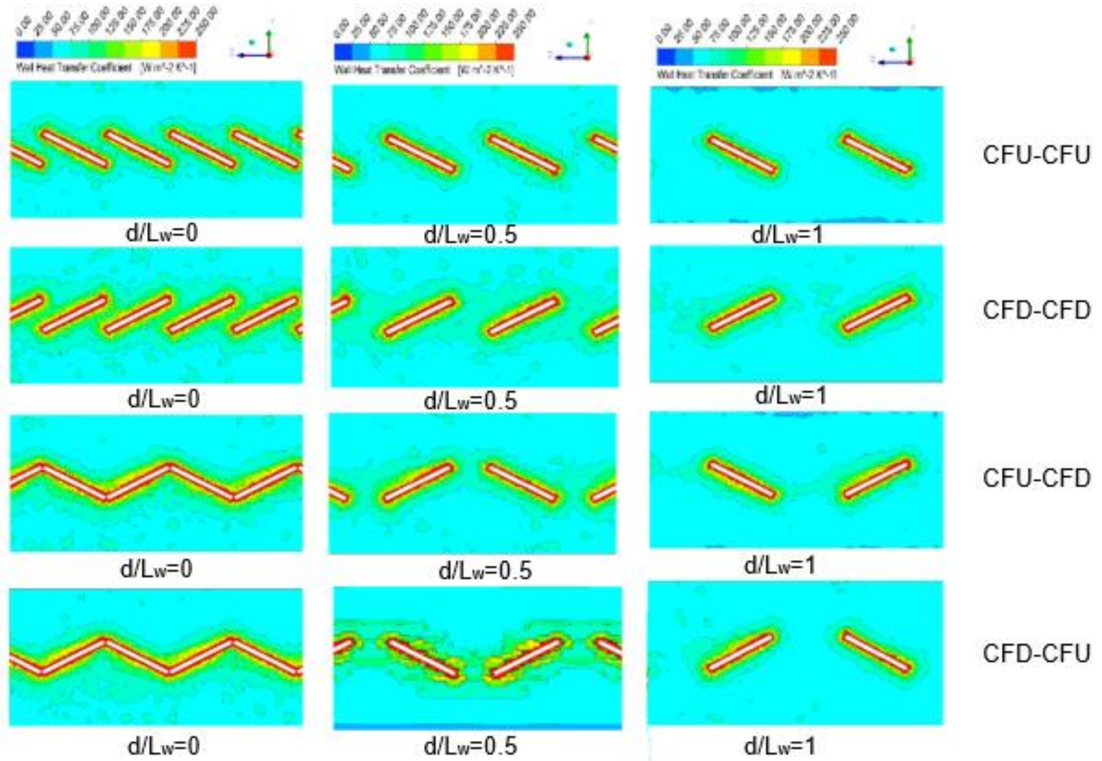

Figure 4.79 Time averaged wall heat transfer coefficient distribution obtained on the slant surface between Z=20.6D-24.02D streamwise location.

Figure 4.79 shows the time averaged wall heat transfer coefficient distribution obtained on one of the slant surfaces of the duct between Z=20.6D-24.02D streamwise position. It is observed that the heat transfer coefficient is higher in the vicinity of the VGs. It is clearly seen that as the distance between the VGs is increased, high heat transfer coefficient area decreases. This is associated with the increase or decrease in the number of VGs used in flow domain. High heat transfer area indicates where the flow mixing is strong and therefore, in terms of heat transfer, it is better to use much VGs in the domain to get a better mixing between hot and cold fluids. However, this causes a further pressure drop, as discussed in the previous section, which is not recommended. Therefore, the selection of the optimum case to obtain the minimum pressure drop and the highest heat transfer coefficient is mandatory in order to get the best thermal and flow characteristics.

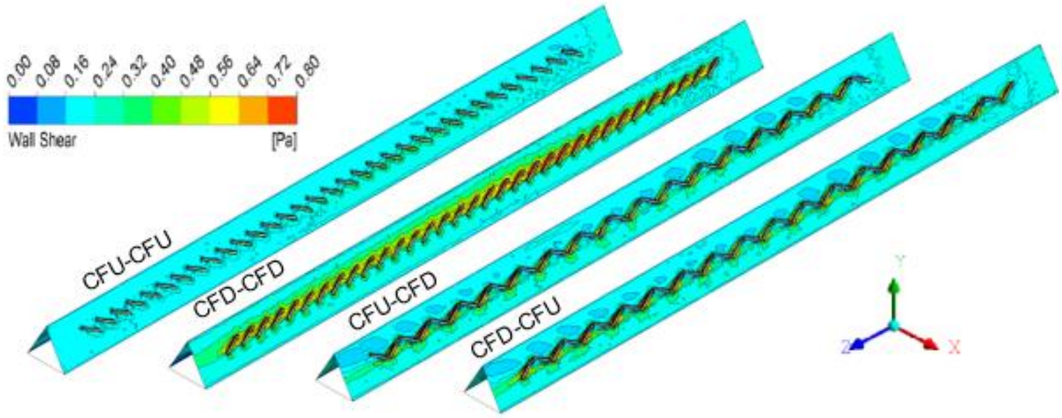

Figure 4.80 Time averaged wall shear distribution obtained on the slant surfaces of the duct for d/Lw=0 case

Figure 4.80 illustrates the time averaged wall shear distribution obtained on the slant surfaces of the duct for d/Lw=0 case. High wall shear distribution corresponds to strong TKE values and enhanced mixing between hot and cold fluids. The wall shear is the highest for the CFD-CFD configuration for d/Lw=0 case as it is clearly seen in Figure 4.80. The worst configuration is the CFU-CFU configuration. As the highest wall shear distribution is concentrated in the vicinity of the VGs, therefore a better mixing and the strongest TKE and therefore enhanced heat transfer is expected to occur in the vicinity of the VGs.

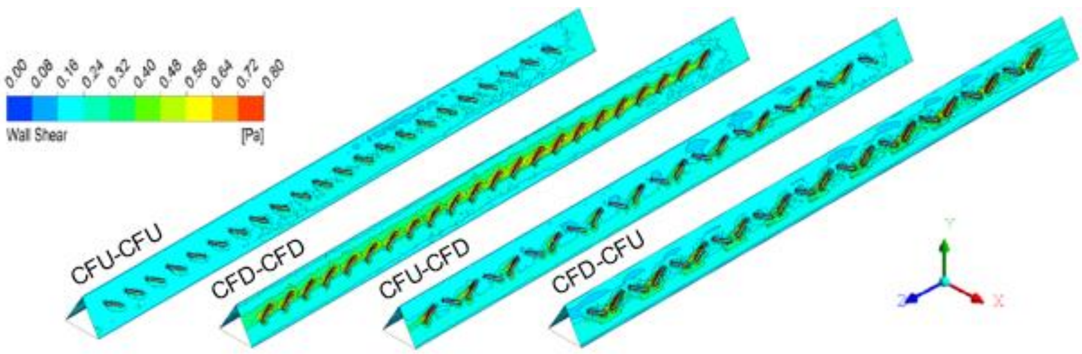

Figure 4.81 Time averaged wall shear distribution obtained on the slant surfaces of the duct for d/Lw=0.5 cases.

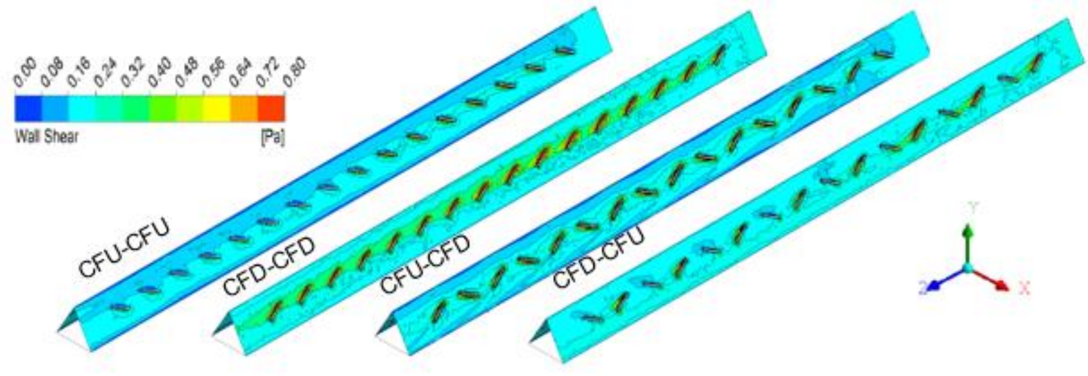

Figure 4.82 Time averaged wall shear distribution obtained on the slant surfaces of the duct for d/Lw=1 cases.

Figure 4.81-Figure 4.82 illustrate the time averaged wall shear distribution obtained on the slant surfaces of the duct for d/Lw=0.5 and d/Lw=1 cases, respectively. Wall shear distribution is again the highest for the CFD-CFD configuration. Remember that the time averaged vorticity (Figure 4.60-Figure 4.62) and TKE (Figure 4.67-Figure 4.69) contours obtained along the duct reveal that the vorticity and the TKE contours remain attached on the duct wall for the CFD-CFD configuration. The present result confirms the former results since the highest wall shear contours are obtained with this configuration. However, this behavior prevents the flow mixing between the hot side walls and the inner part of the duct. Also note that wall shear is distributed from the VGs towards the apex and the base of the duct in the spanwise direction for the CFU-CFD and for the CFD-CFU configurations which can cause a better mixing ability. If a comparison among Figure 4.80-Figure 4.82 is made, it can be concluded that wall shear decreases as the distance between the VGs is increased.

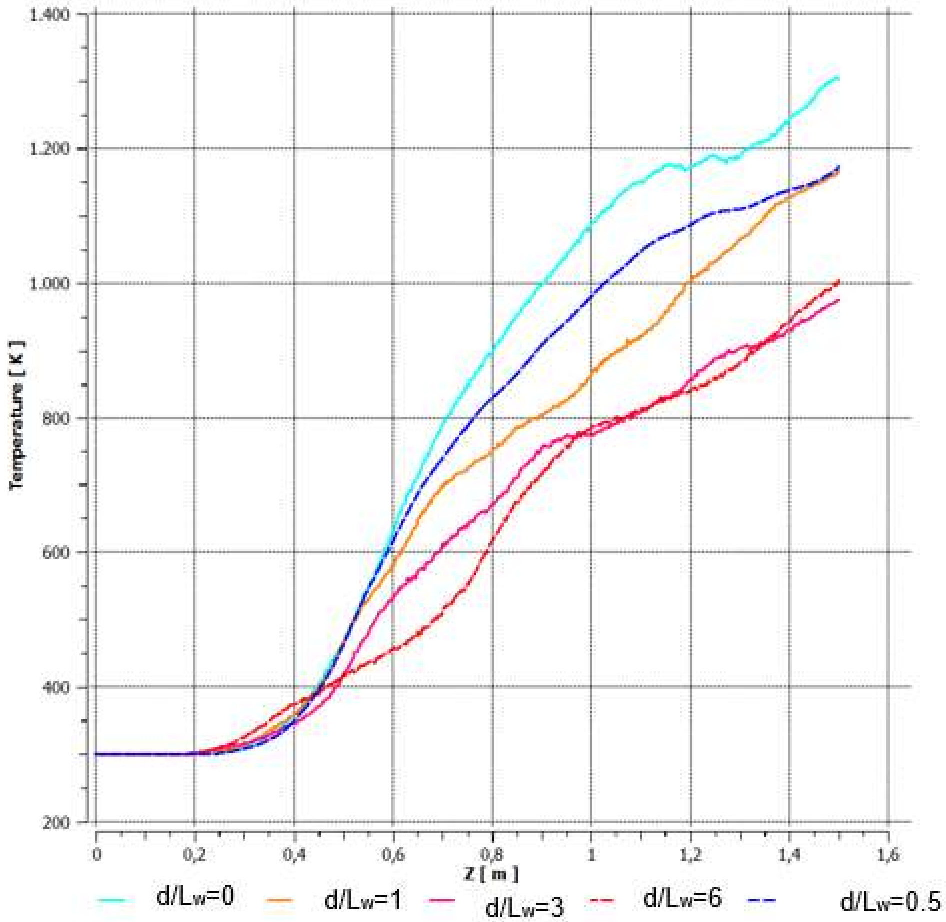

Figure 4.83 Temperature distribution along the z-axis on line L2 (X=0.86D, Y=0.83D) for the CFD-CFU case.

Temperature distribution along the z-axis on line L2 (X=0.86D, Y=0.83D) for the CFD-CFU case is illustrated in Figure 4.83. It is clearly seen that temperature decreases as d/Lw is increased as the flow moves towards the exit of the duct and maximum temperature is obtained for the d/Lw=0 case among the other cases.

4.6.7 Thermal-Hydraulic Performance

In the present investigation, thermal-hydraulic performance is calculated by using the following equation :

$$\text{THP} = \frac{Nu/Nu_s}{(f/f_s)^{1/3}}$$

In the above equation, average Nusselt number is calculated as $Nu = h\,.L/k$. In this expression, average heat transfer coefficient is calculated as follows:

$$h = \frac{\dot{m}.\, c_p.\, (T_{out}\text{-}T_{in})}{A_{\mathrm{HT}}.(T_w\text{-}T_{ave})}$$

Temperature at the outlet section of the duct (T_{out}) is taken as the mass-weighted-average values of the temperature obtained from the present numerical simulations. In Eq. 2, average temperature and heat transfer surface area are calculated as $T_{ave} = (T_{in} + T_{out})/2$ and $A_{\mathrm{HT}} = A_{\mathrm{HW}} + A_{\mathrm{VG}}$, respectively. The friction factor is calculated as

$$f = \frac{2\,.\,\Delta P}{(\rho.W_\infty{}^2)}\left(\frac{D}{L}\right)$$

where $\Delta P = P_{in} - P_{out}$ and $D = 4.A_c/p$

4.6.8 Overall Friction Factor, Nusselt Number and Thermo-Hydraulic Data

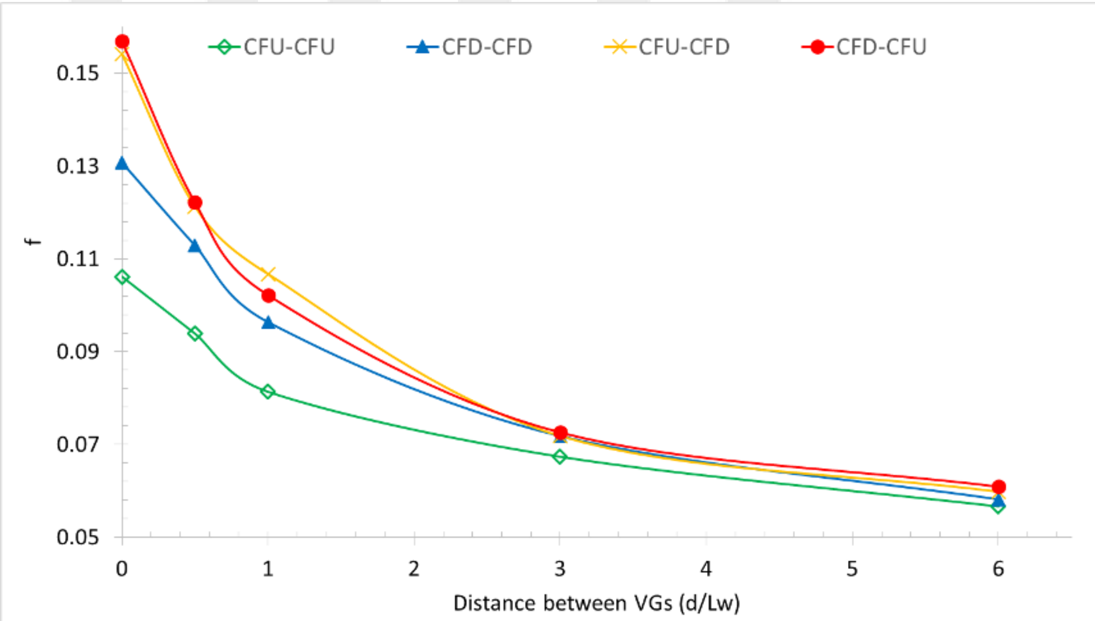

Figure 4.84 Friction factor distribution as a function of distance between VGs arranged in different configurations.

The friction factor distribution as a function of distance between VGs arranged in different configurations is shown in Figure 4.84. For each configuration, the calculated f values decrease as the distance between VGs is increased. As it is clearly seen from the figure, the pressure drop becomes maximum when the distance between VGs is minimum. This is because of the fact that the flow separation occurs as the flow reaches each VG pair causing a pressure drop. The highest pressure drop is obtained for d/Lw=0 case for each configurations studied and as the distance between the VGs is increased, the pressure drop decreases as well, which means that the pressure difference between the inlet and outlet sections of the domain becomes less as a result of the less amount of VGs used in the flow domain, and the flow separation becomes less as well. Comparing to all cases studied, the calculated values of f are higher for the CFU-CFD and CFD-CFU configurations compared with the CFU-CFU and CFD-CFD configurations. The minimum pressure drop is obtained for the CFU-CFU case for all d/Lw values compared with other cases and therefore it can be said that CFU-CFU case is the best case since it generates less pressure drop between the inlet and outlet sections of the duct comparing to the other cases.

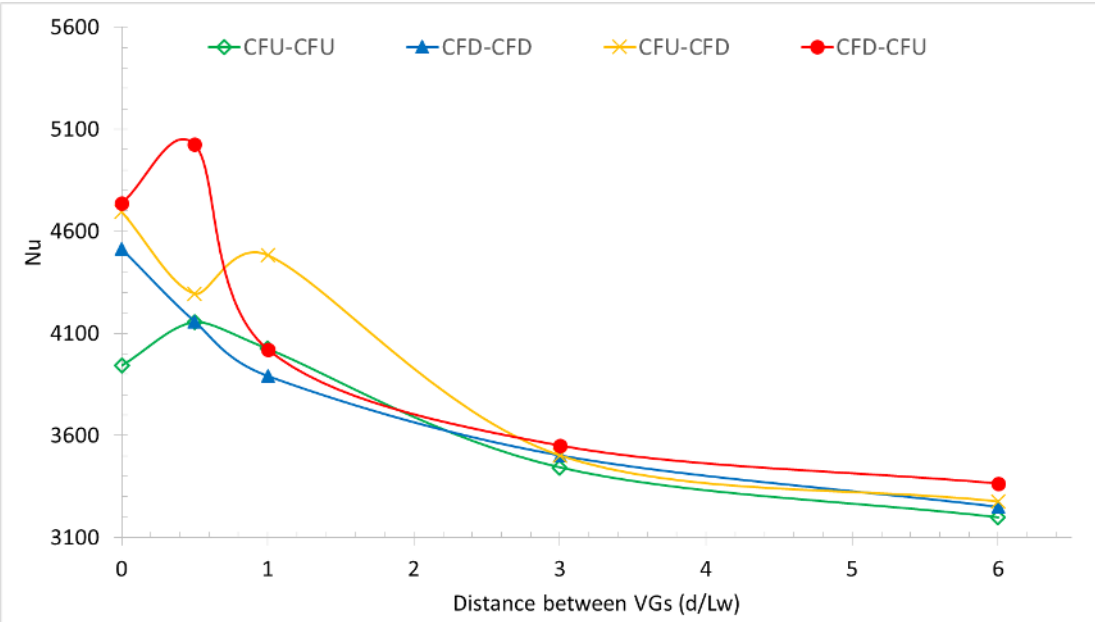

Figure 4.85 Average Nusselt number distribution as a function of distance between VGs arranged in different configurations.

Figure 4.85 illustrates average Nusselt number distribution as a function of distance between VGs (d/Lw). Overall comparison between the cases studied states that the convective heat transfer is enhanced as the distance between VGs becomes less. This is mainly due to the increase in the number of VGs used in the flow domain. Each configuration generates a peak in the Nusselt number except the CFD-CFD configuration. This peak is located at d/Lw=0.5 for the CFD-CFU and CFU-CFU configurations and at d/Lw=1 for the CFU-CFD configuration. After this peak, Nusselt number continuously decreases as d/Lw is increased. As the maximum peak is obtained for the CFD-CFU configuration for d/Lw=0.5 case, therefore, it can be said that this case is the best case in terms of the best convective heat transfer characteristics.

To better understand the combined effects of heat transfer and pressure drop relation throughout the flow domain and to help selection of the best VG configuration and d/Lw value, the thermo-hydraulic performance (THP) is evaluated for each case and the calculated results are presented in Figure 4.86.

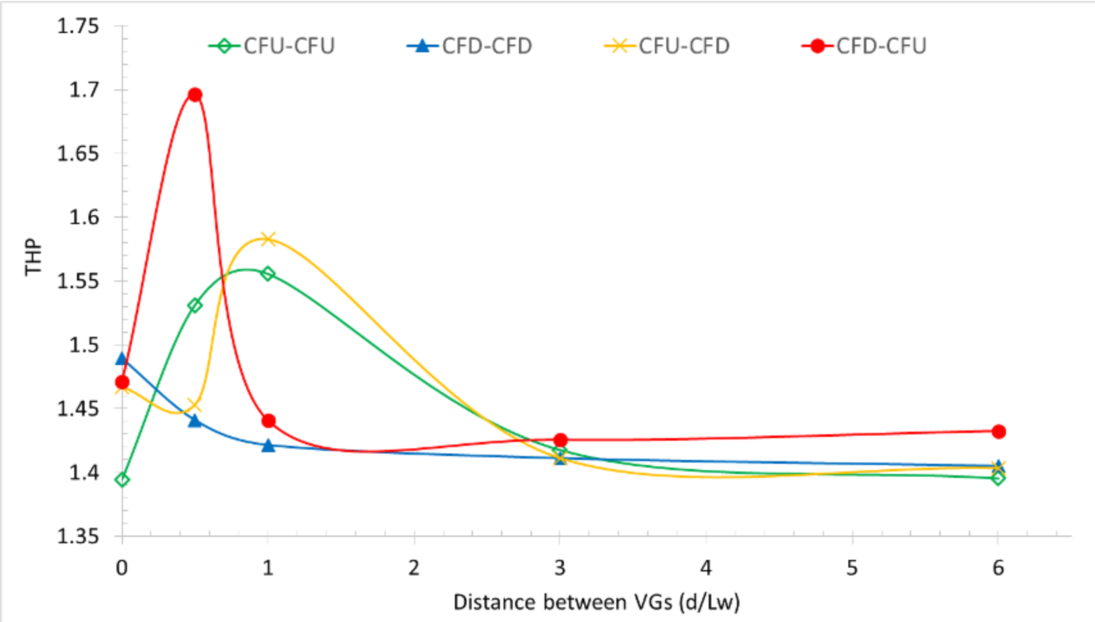

Figure 4.86 Calculated values of THP as a function of distance between VGs arranged in different configurations.

As shown in Figure 4.86, THP sharply increases and decreases between 0≤d/Lw≤0.5 and between 0.5≤d/Lw≤1, respectively, takes its highest value at d/Lw=0.5 and then becomes nearly constant between 1≤d/Lw≤6 for the CFD-CFU configuration. The similar trend is obtained for the CFU-CFU configuration but the maximum value of THP is located at d/Lw around 1. THP value takes its minimum and maximum at d/Lw=6 and d/Lw=1, respectively CFU-CFD configuration. No peak is observed in the calculated values of THP for the CFD-CFD configuration. Among the all cases studied, THP becomes maximum for the CFD-CFU configuration at d/Lw=0.5. Considering the dependence of THP on Nusselt number and friction factor, the convective heat transfer (h) becomes maximum, although pressure drop (ΔP) higher for mostly cases, it is obviously optimum case is the CFD-CFU configuration at d/Lw=0.5.

All of the discussions above show that there must be a certain distance between the VGs in order to allow interaction of local vortices generated by the VGs with the main flow and thus to allow mixing of hot and cold fluids but with a minimum pressure drop. In some of the discussions sometimes CFU-CFD configuration and sometimes d/Lw=0 case showed better results. However, the last discussion on THP helps us to determine the best case and configuration which is CFD-CFU configuration with d/Lw=0.5 case since this combination has a better thermal and hydraulic performance and therefore is considered to be the optimum case.

In the following section, the discussions are concentrated on the effect of the spanwise distance between the VGs to find the best configuration.

4.7 Effects of the Spanwise Distance between the VGs

Since the best combination is selected as the CFD-CFU configuration with d/Lw=0.5 case, therefore, the following discussion is built up with this best case for determining the best spanwise distance between the VGs. In this best case, the distance between the VG pairs and the duct base were equal (Hy=Hy1=Hy2=0.65D=37.895mm). Hy1 designates the minimum distance between the closest point of the CFD type VGs and the duct base in the y-direction. Similarly, Hy2 designates the minimum distance between the closest point of the CFU type VGs and the duct base in the y-direction (Figure 4.87). In this section, 16 simulations are performed to determine the optimum values of Hy1 and Hy2. The tested spanwise distance between the VGs are shown in the below Table 4.1 and Table 4.2.

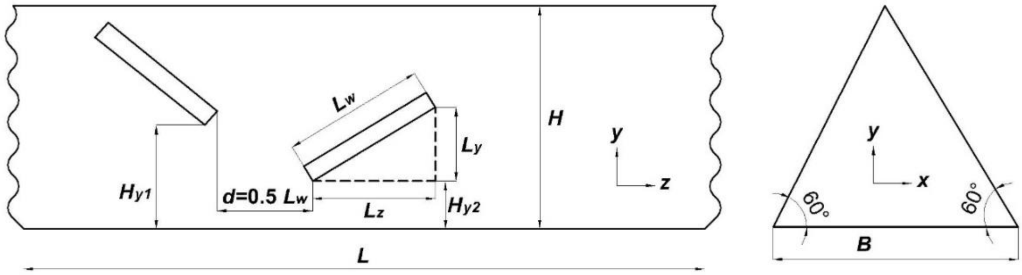

Figure 4.87 Illustration of distance between the duct base and the CFD and CFU type VGs in the y-direction, H_{y1} ve H_{y2}.

Table 4.1 THP, Nu, f results of CFD-CFU geometries, d=0.5Lw for first 8 cases.

H_{y1} H_{y2}	20 mm 10 mm	30 mm 10 mm	30 mm 20 mm	40 mm 10 mm	40 mm 20 mm	40 mm 30 mm	50 mm 10 mm	50 mm 20 mm
f/f_s	2.042	2.351	2.246	2.728	2.413	2.274	2.961	2.836
Nu/Nu_s	1.971	2.1049	2.2459	2.4392	2.2530	2.2041	2.5243	2.428
f	0.0846	0.0974	0.0924	0.1096	0.1042	0.0915	0.1096	0.1093
Nu	4020	4360	4630	4990	4734	4522	5041	4913
THP	1.5573	1.5875	1.7154	1.7463	1.6847	1.6807	1.7643	1.7213

Table 4.2 THP, Nu, f results of CFD-CFU geometries, d=0.5Lw for last 8 cases.

H_{y1} H_{y2}	50 mm 30 mm	50 mm 40 mm	60 mm 10 mm	60 mm 20 mm	60 mm 30 mm	60 mm 40 mm	60 mm 50 mm	37.9mm 37.9mm
f/f_s	2.395	2.136	3.024	2.874	2.77	2.218	1.891	2.949
Nu/Nu_s	2.1251	1.9613	2.3212	2.417	2.243	2.036	1.8347	2.4235
f	0.0993	0.0892	0.1247	0.1039	0.1142	0.0915	0.0779	0.1222
Nu	4346	4001	4805	4789	4625	4178	3785	5025
THP	1.5931	1.523	1.6058	1.706	1.6026	1.5653	1.4868	1.6961

4.7.1 Time Averaged Streamline Patterns

Figure 4.88 shows time averaged streamline patterns obtained on Z=7.2 D plane for the CFD-CFU configuration with d/Lw=0.5 case. On this local plane, each case is able to create large and small scale foci as shown in the figure. The flow mixing is better above the y-symmetry axis for the 30-10 (Hy1=30 mm, Hy2=10 mm), 30-20mm cases, and it is better below the y-symmetry axis for the 40-10mm, 40-20mm, 50-10mm, 50-20mm, 60-20mm cases. However, the considering the whole plane, 40-30mm, case is better in terms of flow mixing as the foci are distributed in the whole domain.

37.895mm-37.895mm case shows the weakest mixing characteristics since the foci formed in this local plane are found very weak.

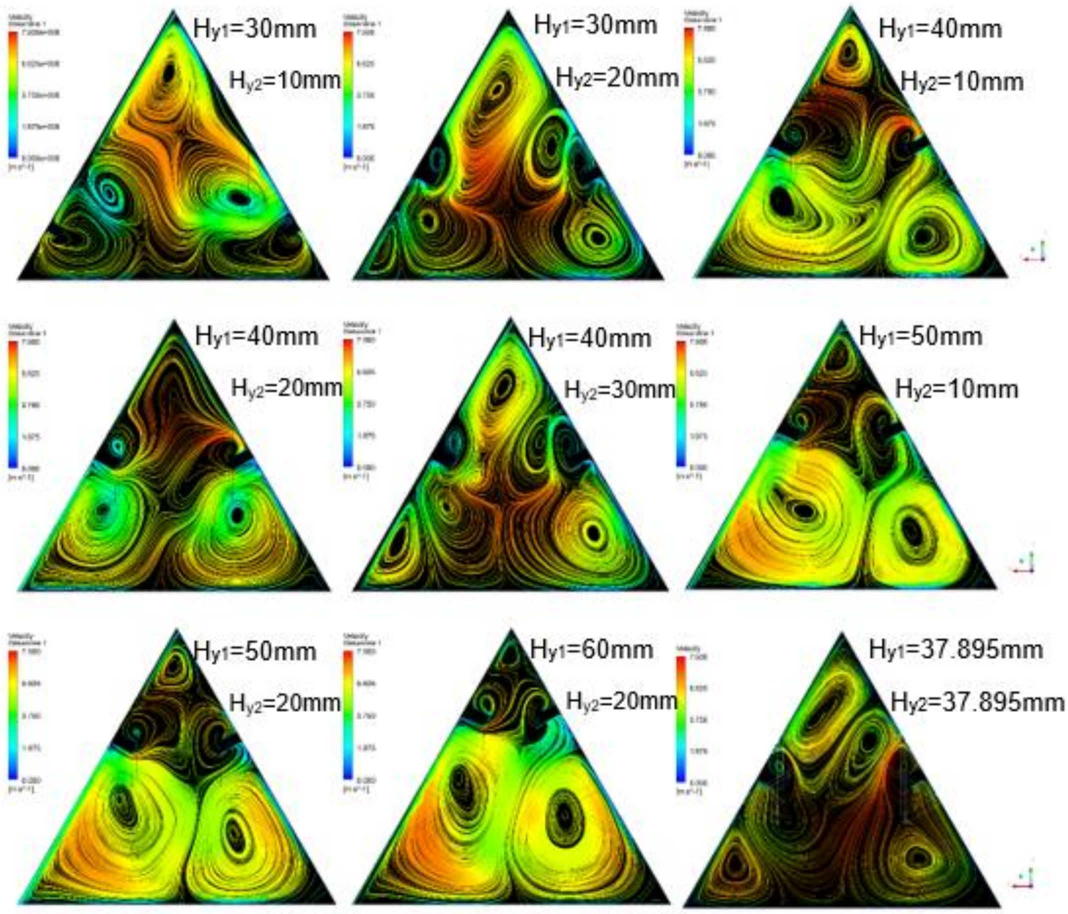

Figure 4.88 Time averaged streamline patterns obtained on Z=7.2 D.

Figure 4.89 shows time averaged streamline patterns obtained on Z=8.41 D plane for the CFD-CFU configuration with d/Lw=0.5 case. In this farther downstream position, flow mixing is found the best for the 40-10mm, 40-20mm, 40-30mm, 50-10mm, 50-20mm cases as the number of foci is much more than the other cases. The weakest mixing property is again obtained for the 30-10mm and 37.895-37.895mm cases.

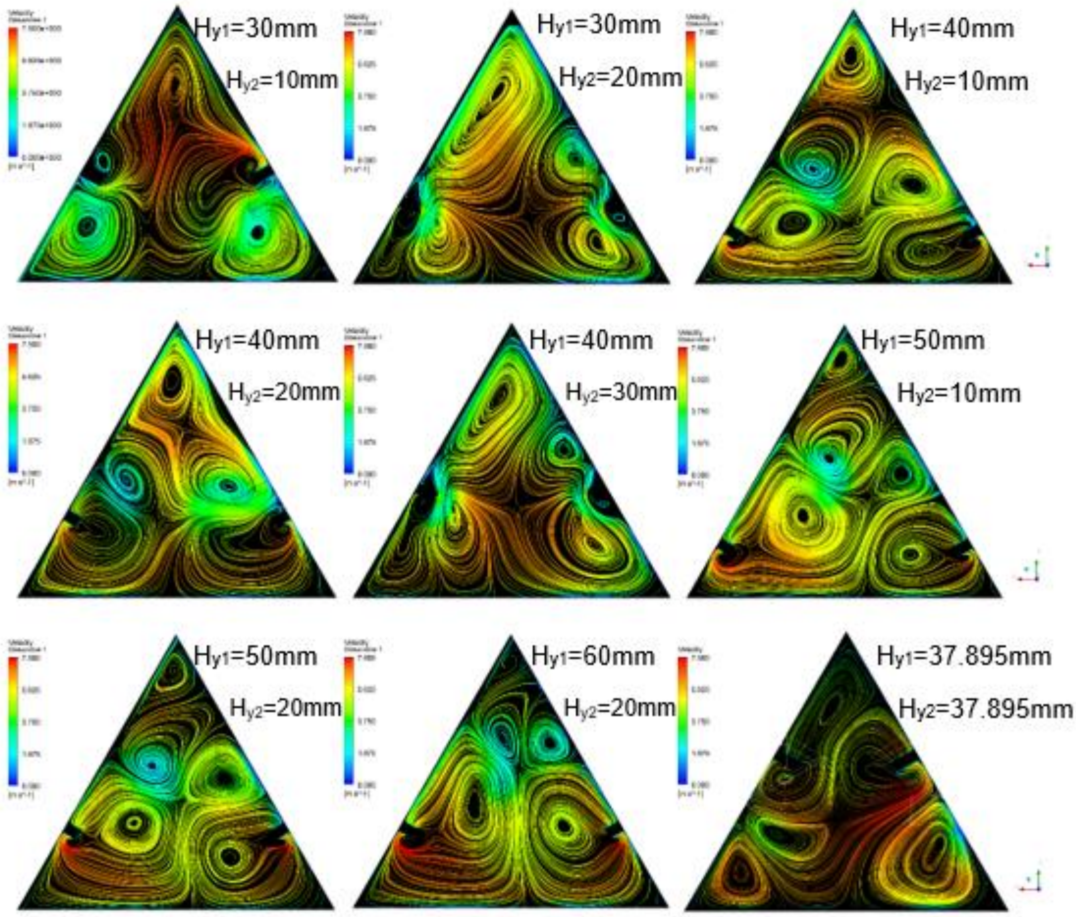

Figure 4.89 Time averaged streamline patterns obtained on Z=8.41 D.

4.7.2 Time Averaged Vorticity Contours

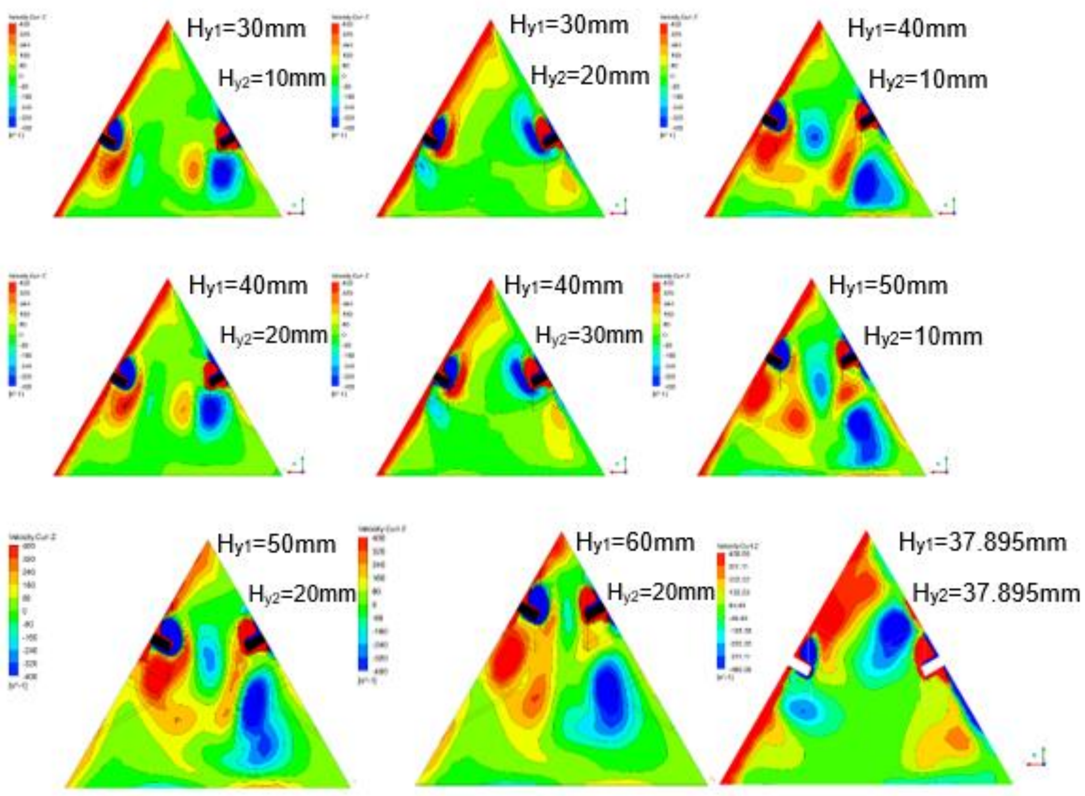

Figure 4.90 Time averaged vorticity contours obtained on Z=8.41 D.

Figure 4.90 shows time averaged vorticity contours obtained on Z=8.41D plane for the CFD-CFU configuration with d/Lw=0.5 case. The vortex interaction as well as the population density of the vortices formed are found better for the 40-10mm, 50-10mm, 50-20mm and 60-20mm cases.

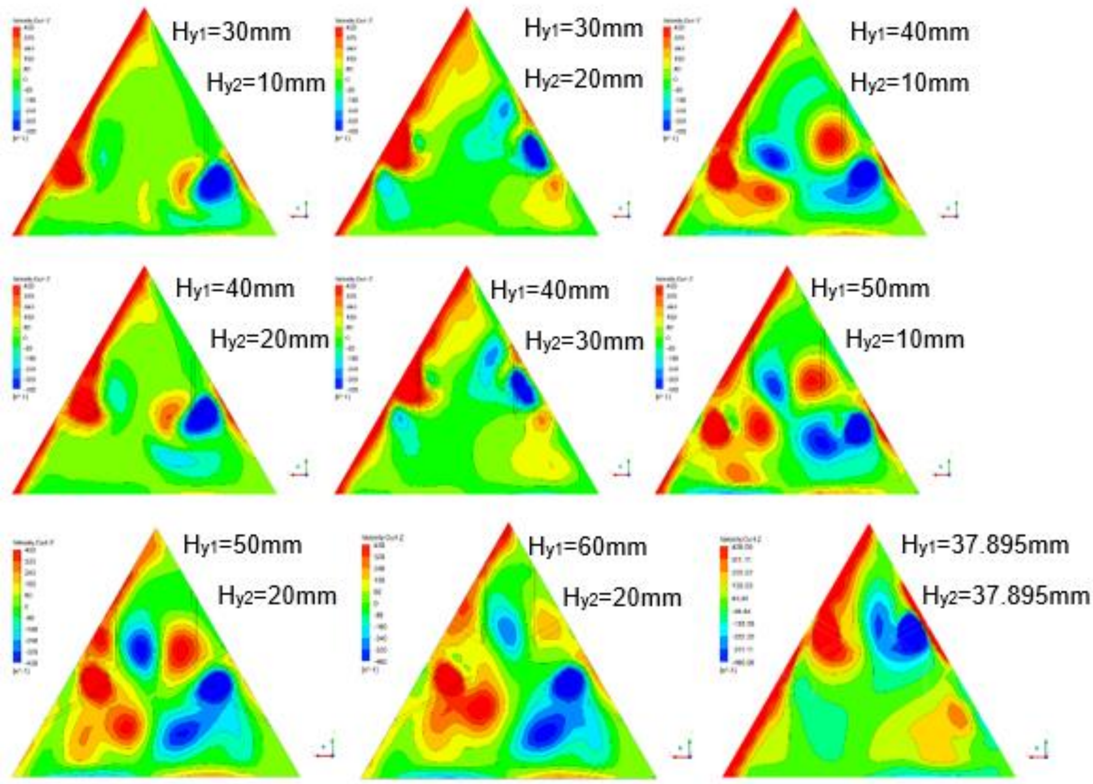

Figure 4.91 Time averaged vorticity contours obtained on Z=18.61D.

Figure 4.91 illustrates time averaged vorticity contours obtained on Z=18.61D plane for the CFD-CFU configuration with d/Lw=0.5 case. On this streamwise plane, the interaction and the population density of vortices are found better for the 50-10mm, 50-20mm and 60-20 mm cases. Vorticity concentrations are also very strong with these cases. Among them, 50-10 mm shows a better flow interaction between the side walls, inner section of the duct and the duct base.

Since the flow characteristics change continuously in the flow domain and examination of the results obtained from the local streamwise planes is difficult to find the best case, flow and heat transfer data such as temperature, turbulent kinetic energy and velocity swirling strength distributions along the duct are illustrated in the following section.

4.7.3 Flow and Heat Transfer Data along the Duct

Comparison of the cases studied in terms of temperature profile obtained on line Lu (X=0.86 D, Y= 1.23 D) is shown in Figure 4.92. Note that temperature increases along the main flow direction for each of the cases studied. Along the duct, temperature values for the 30-10mm, 40-20mm, 40-10mm, and 50-10mm cases are found lower than the 40-30, 37.895-37.895mm, 30-20mm, 60-20mm and 50-20mm cases. Since the duct and the VG surfaces are at high temperature than the inner section of the duct, then, the cases created higher temperature at the inner section of the duct are preferable since the main objective is to get the highest temperatures inside the duct. Therefore, the cases created lower temperature distribution is better than the cases created higher temperature distribution inside the duct along the main flow direction.

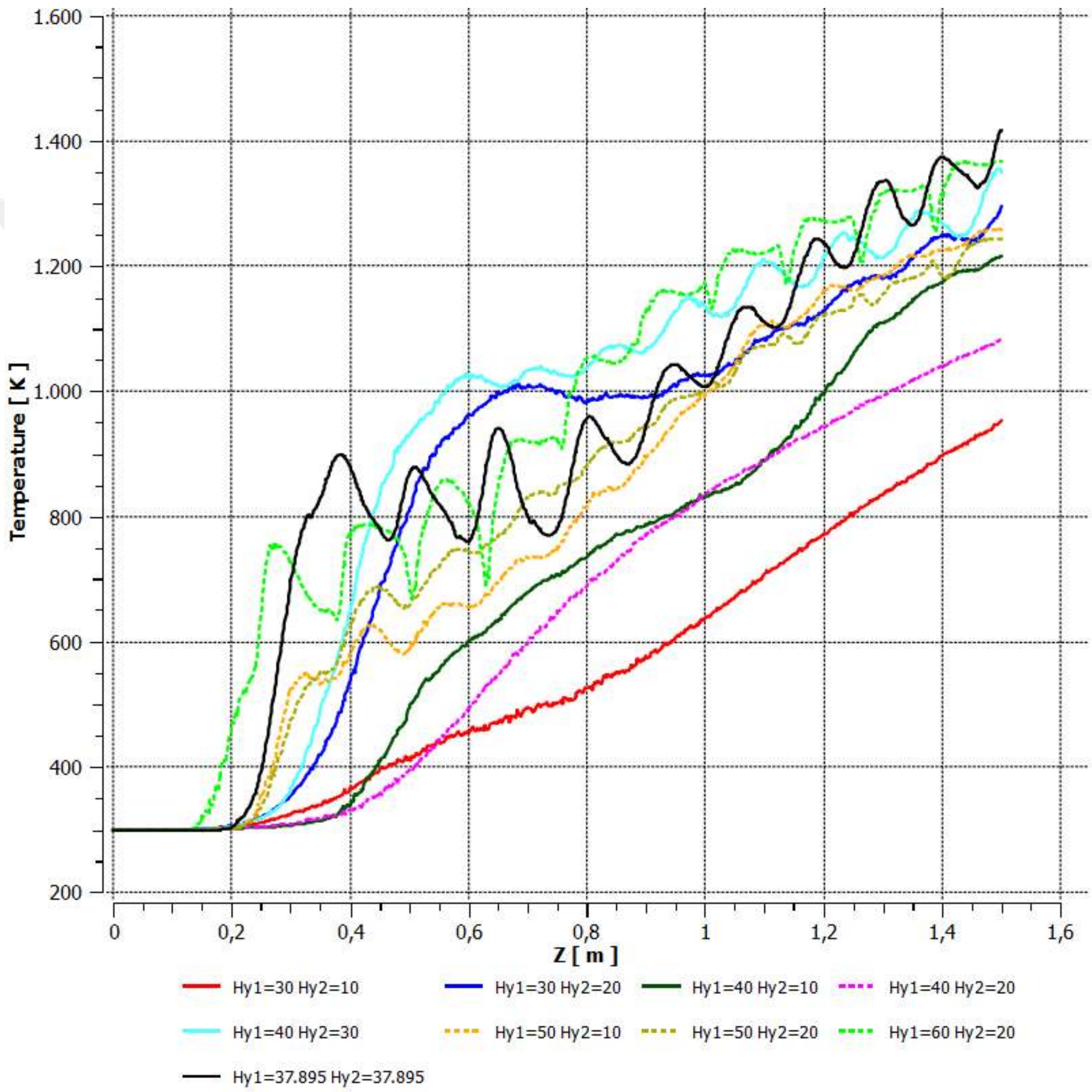

Figure 4.92 Comparison of the cases studied in terms of temperature profile obtained on line Lu (X=0.86 D, Y= 1.23 D).

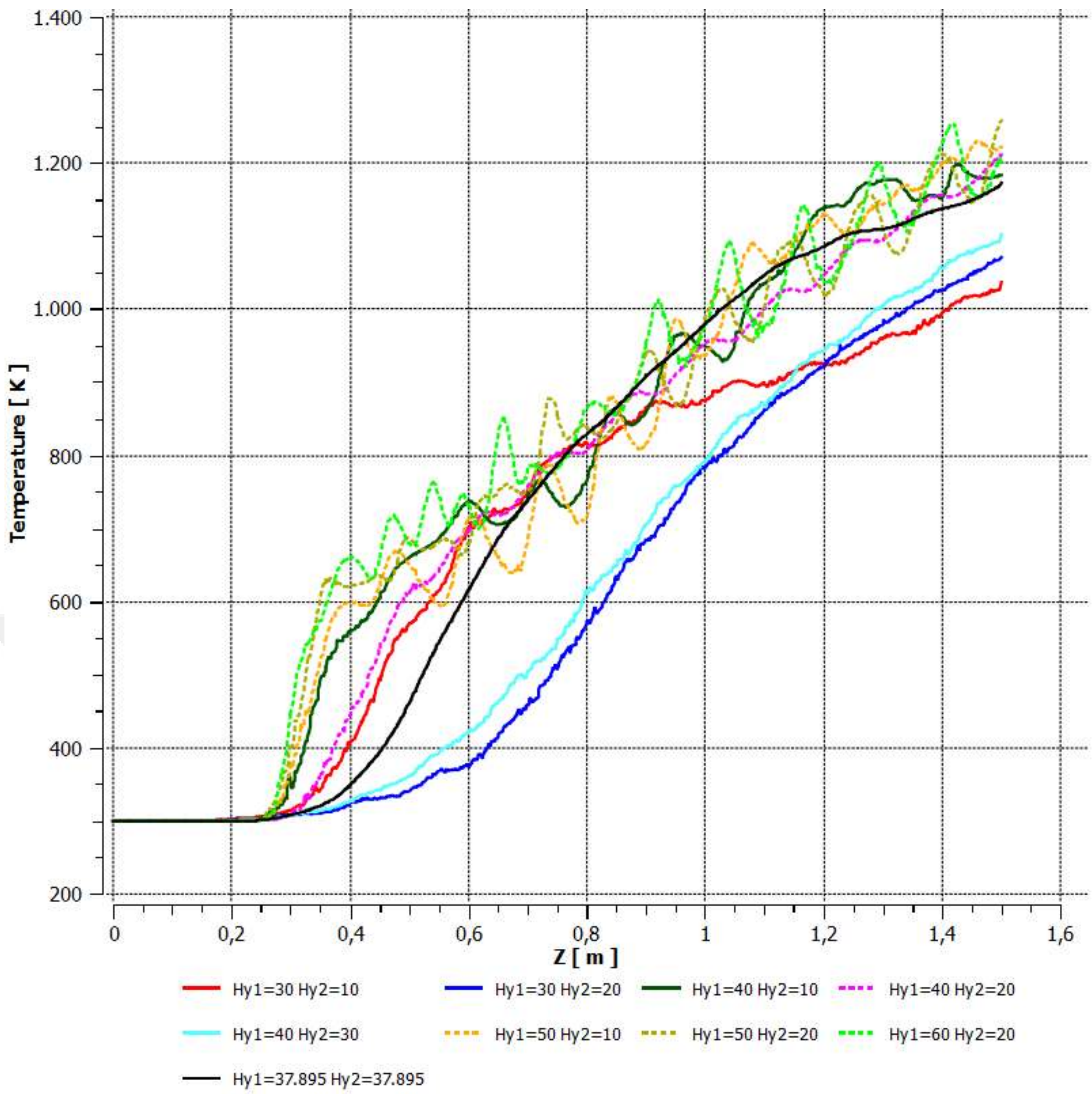

Figure 4.93 Comparison of the cases studied in terms of temperature profile obtained on line La (X=0.86 D, Y= 0.41 D).

Comparison of the cases studied in terms of temperature profile obtained on line La is shown in Figure 4.93. Temperature starts to increase after about Z=0.3 m for each cases studied. The lowest temperature profile is obtained for the 40-30mm and 30-20mm cases as clearly seen in the figure. Even if most of the cases show small or big variation or oscillation along the line La (X=0.86 D, Y= 0.41 D), only 37.895-37.895mm case show no oscillation while the flow moves in the downstream position. The highest temperatures are obtained for 60-20mm and 50-10mm cases on this line.

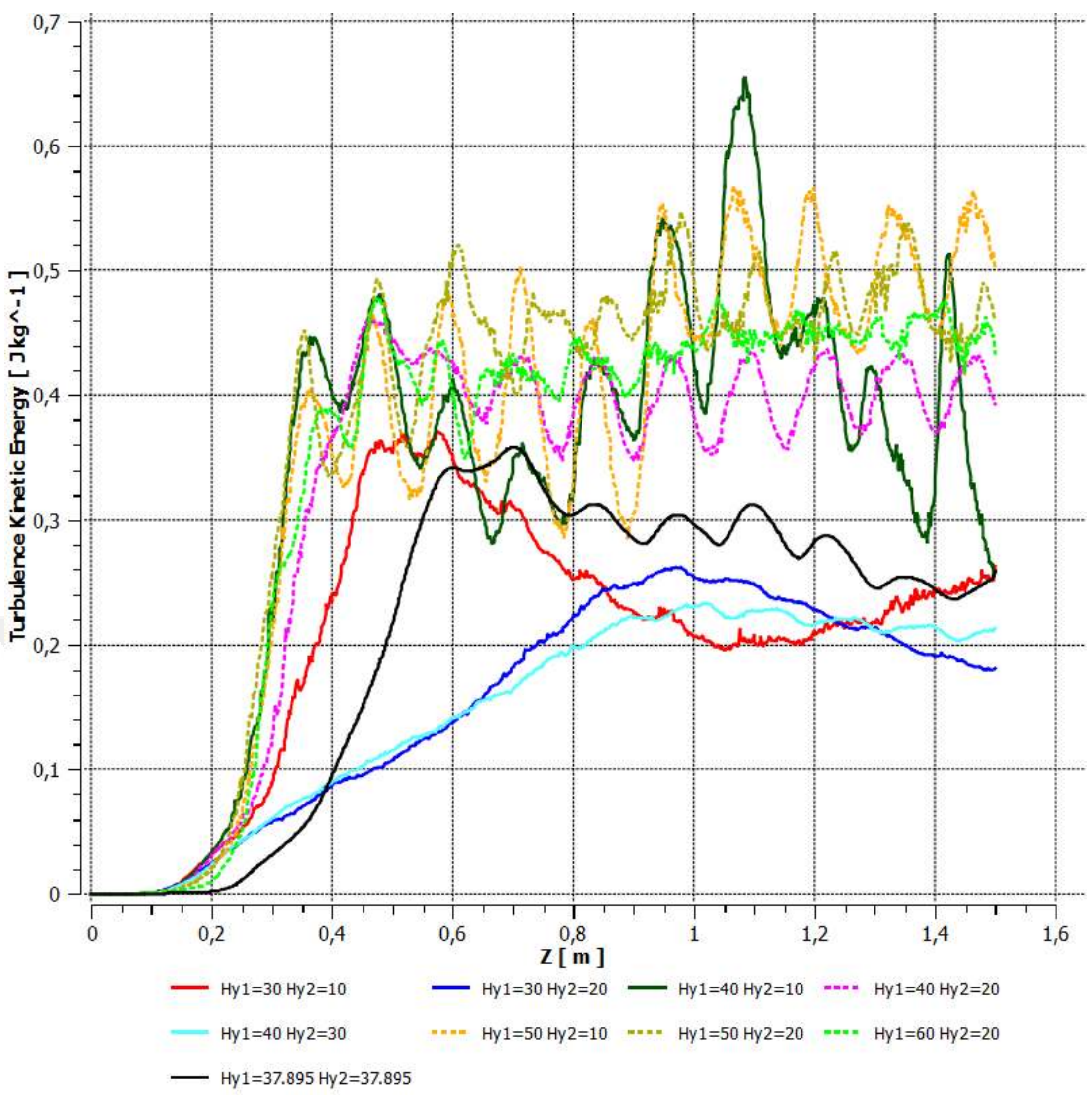

Figure 4.94 Comparison of the cases studied in terms of TKE distribution obtained on line Lu.

Figure 4.94 shows variation of TKE obtained on line Lu for all the cases studied. Since there is no VGs and as a result no flow mixing at the inlet section of the duct, TKE is equal to zero near the inlet section of the duct for all the cases studied. After around Z=0.15 m, TKE starts to increase for all the cases. Some cases show a sudden increase in the TKE where the first VG pair is reached. Several peaks correspond to the location of the VG pairs. Fluid mixing becomes better at the locations where the maximum TKE occurs. As can be seen from the figure, the mixing effect is not good for the 37.895-37.895mm, 30-20mm, 30-10mm, 40-30mm cases. The best mixing effect is obtained for the 50-10mm and 50-20mm cases. The 40-10mm case shows a maximum peak at Z=1.1 m, but TKE values generally do not exceed the peak values obtained from the 50-10mm and the 50-20mm cases. The maximum peaks towards the exit section of the duct are obtained for the 50-10mm case.

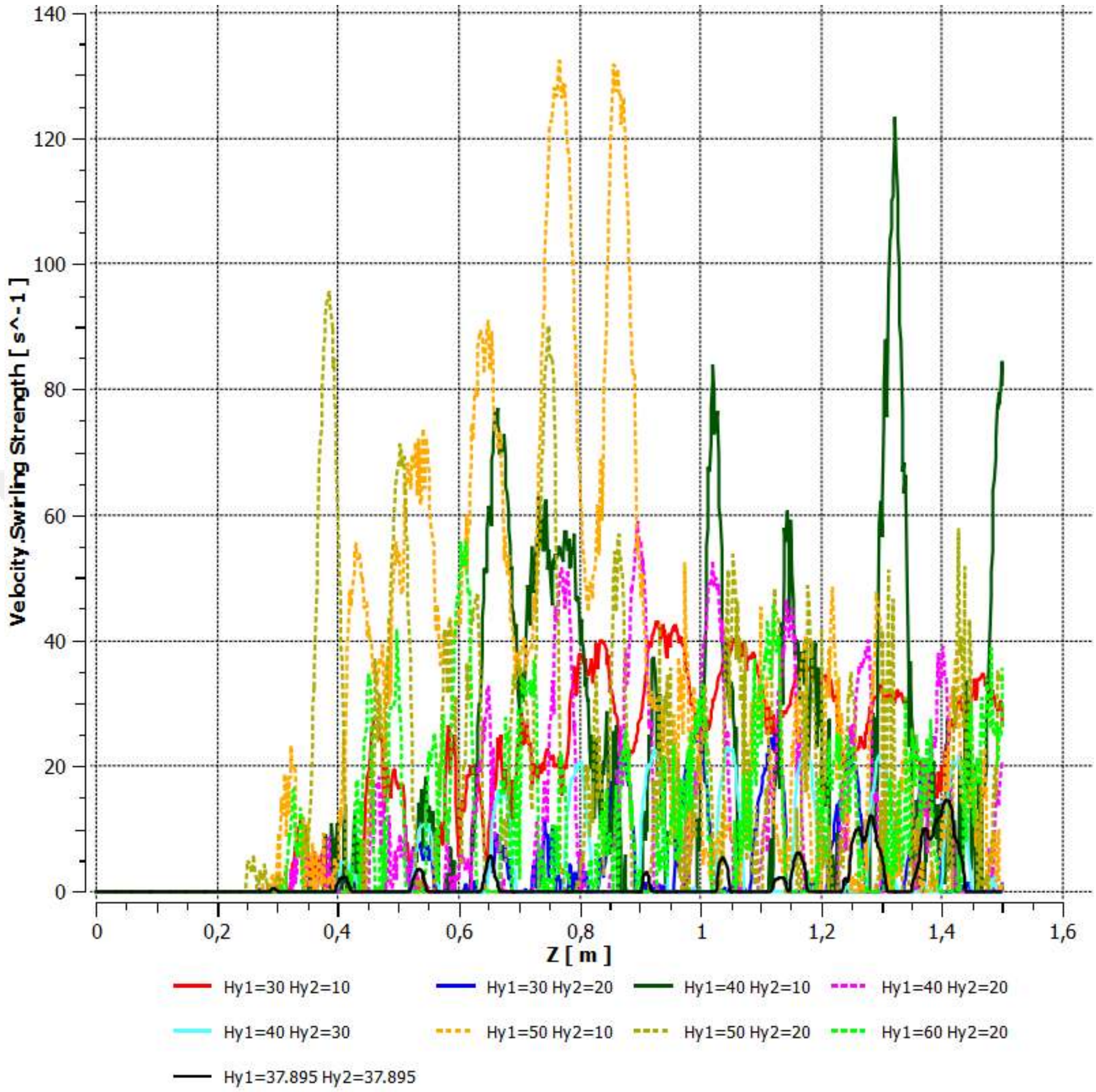

Figure 4.95 Comparison of the cases studied in terms of velocity swirling strength distribution obtained on line Lu.

Velocity swirling strength distribution obtained on line Lu is presented in Figure 4.95. The swirling strength becomes weaker for the most cases as it is clearly seen in the figure. As this value describes the strength of the vertical motion, it is observed that the best case in terms of swirling strength of the vortices is 50-10mm case since the maximum peaks are obtained from this case especially at the former section of the duct. For this case, towards the latter section of the duct, the values of velocity swirling strength becomes moderate but they are still better than the most cases. Towards the exit section of the duct, the maximum peaks are obtained for the 40-10mm case, but the number of peaks is low and is just equal to 3.

Like in the other section, f, Nu and THP data are evaluated for the present cases studied as this way of evaluation is the best way since the calculated values represent the values in whole domain beginning from the inlet to the outlet section of the duct. Calculated values of friction factor as a function of spanwise distance between the VGs for the cases studied is shown in Figure 4.96. As a reminder, friction factor represents the pressure drop between the inlet and the outlet section of the duct. As shown from the figure, the best case is the 40-30mm case since it produces the minimum pressure drop throughout the domain. This is flowed by 30-20mm and 30-10mm cases, respectively. The worst case is the 37.895-37.895mm case since the maximum value of the pressure drop is obtained from with this case.

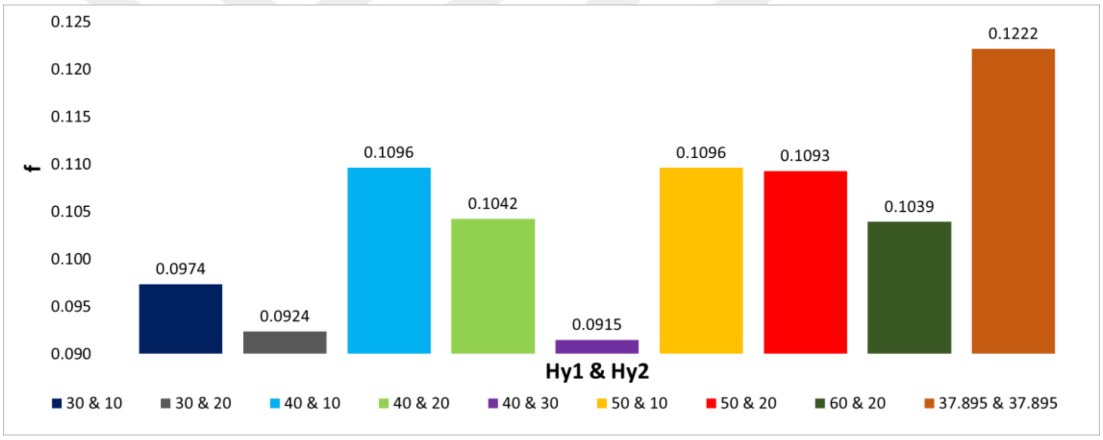

Figure 4.96 Calculated values of friction factor as a function of spanwise distance between the VGs for the cases studied.

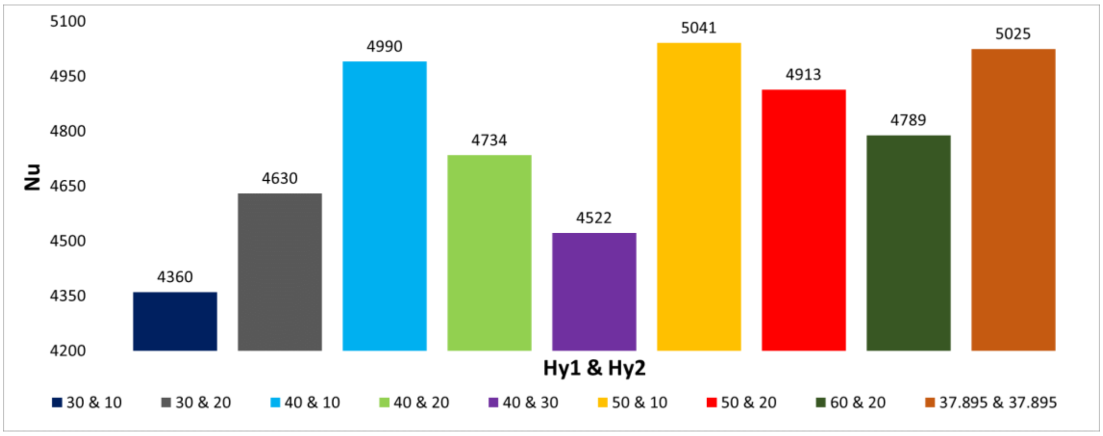

Figure 4.97 Calculated values of Nusselt number as a function of spanwise distance between the VGs for the cases studied.

Nusselt number results are seen in Figure 4.97. The best case (40-30mm) selected according to the friction factor in the previous section shows low value of Nusselt number. As the Nusselt number is directly related to the convective heat transfer, the best convective heat transfer is obtained for the 50-10mm, 37.895-37.895mm, 40-10mm cases. Amon these three cases, the maximum Nu is obtained for the 50-10mm case as shown in Figure 4.97.

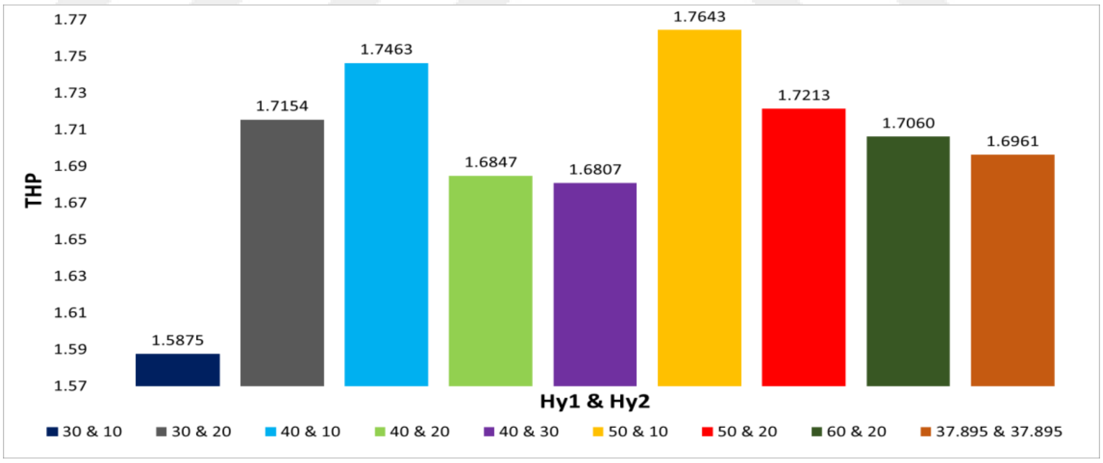

Figure 4.98 Calculated values of THP as a function of spanwise distance between the VGs for the cases studied.

The calculated values of THP are presented in Figure 4.98. As it is clearly seen, the minimum THP is obtained for the 30-10mm case and therefore this case is the worst case in terms of both thermal and hydraulic characteristics. It is obviously seen that the maximum THP is obtained for the 50-10mm case. This is followed with the 40-

10mm and 50-20mm cases, respectively. Therefore, the maximum heat transfer characteristics with minimum pressure drop is obtained by the 50-10mm case.

CHAPTER 5

CONCLUSION

In the present numerical study, flow and heat transfer characteristics of 3-D triangular vortex generators (VGs) located in a triangular duct representing internal cooling channel of a gas turbine blade are investigated deeply to find the best VG type and the best streamwise and spanwise distances between the VGs and the duct base in the context of thermal and hydrodynamic properties. The investigated VG types are periodically located inside the triangular duct in either smooth or in alternating directions and they are oriented as CFU-CFU, CFD-CFD, CFU-CFD configurations. The investigated flow data include streamline patterns, time averaged vorticity contours, turbulence kinetic energy distributions, pressure, velocity swirling strength, wall shear data, heat transfer coefficient, friction factor and finally thermo-hydraulic performance parameter. The flow Reynolds number is fixed to 20,000, and inlet and wall temperatures are fixed to 20° C and 1760° C, respectively. The rotation number is 0.488. The obtained results are as follows:

The time averaged streamline patterns obtained for the cases studied reveal that as the streamwise distance between the VGs (d/Lw) is increased, the flow mixing becomes worse, interaction between the foci formed at each plane weakens and the secondary flow formation almost disappears for each configuration as d/Lw increases. There is almost no interaction between the foci for the CFU-CFU configuration. CFD-CFD configuration may be better than the CFU-CFU configuration in terms of number and size of the foci formed for each d/Lw case. The strongest secondary flow formation is observed for d/Lw=0 and 0.5 cases for both CFU-CFD and CFD-CFU configurations. The flow mixing becomes better as the distance between the VGs is increased from 0 to 0.5 for the CFU-CFD and CFD-CFU configurations. If a comparison made between the CFU-CFD and CFD-CFU configurations for d/Lw=0.5 case, it can be said that both cases are able to generate secondary flow which causes further enhancement in heat transfer. The flow mixing is obviously better for the CFD-CFU configuration compared with the CFU-CFD configuration. Therefore, more heat can be convected from the hot side walls towards the center and towards the upper corner of the duct for the CFD-CFU configuration.

It is found that increasing the non-dimensional streamwise distance between the VGs lowers the ability of flow mixing, vortex strength and as a result decreasing the heat transfer for each configuration. It is concluded that CFU-CFD and CFD-CFU configurations are better than the CFU-CFU and CFD-CFD configurations in terms of vortex formation area, vortex strength and vortex interaction which means that a stronger mixing and therefore better heat transfer characteristics can be obtained with the former configurations. In terms of vortex strength and local and global mixing ability of the generated vortices with the cases studied, it is found that d/Lw=0 and 0.5 cases has more advantages than the other cases.

The population density, size and swirling strength of the vortices depend strongly to the distance between the VGs as well as the VG configuration and there is a strong foresight about the optimum case to be the CFD-CFU configuration with d/Lw=0.5 case since the maximum swirling strength and maximum population density of the vortices are obtained for this case and configuration, even at farther downstream locations.

In terms of heat transfer enhancement, it is found that the more the number of VGs used in the domain, the more the heat transfer enhancement. However, in terms of pressure drop, increasing the number of VGs used in the domain causes more pressure drop which is not recommended in terms of economic considerations. Therefore, the best case is chosen as d/Lw=0 in terms of heat transfer data but this case is the worst case in terms of pressure drop since it causes a further pressure drop. Therefore, the selection of the optimum case to obtain the minimum pressure drop and the highest heat transfer coefficient is mandatory in order to get the best thermal and flow characteristics. When the thermal and hydrodynamic characteristics (THP) are considered together, the best case and best configuration are determined as CFD-CFU configuration with d/Lw=0.5 case since this combination has a better thermal and hydraulic performance and therefore is considered to be the optimum combination.

After selection of the optimum streamwise distance between the VGs and the best configuration, the best spanwise distance between the VGs and the duct base is also investigated in terms of thermo-hydraulic properties, vortex formation, swirling strength of the generated vortices and turbulence kinetic energy. At the end of the study, the best conditions are achieved when the spanwise distance between the VGs and the duct base is equal to 0.0222 and 0.222 times the VG length, for the CFD and CFU configurations, respectively.

As a conclusion, the best cooling performance for the leading edge of the gas turbine blades is obtained for the CFD-CFU configuration and for the streamwise distance between the VGs is equal to the 0.5 times the VG length and the best spanwise distance between the VGs and the duct base is equal to Hy1 (CFD distance to duct base) =50 mm and Hy2 (CFU distance to duct base) =10 mm the VG length, for the CFD and CFU configurations, respectively.

REFERENCES

[1] Chang, S. W., Morris, W. D. (2003). Heat transfer in a radially rotating square duct fitted with in-line transverse ribs. *International Journal of Thermal Sciences*. **42(3),** 267-282.

[2] Moritz, N., Kusterer, K., Bohn, D., Sugimoto, T., Tanaka, R., and Taniguchi, T. (2003). Conjugate calculation of a film-cooled blade for improvement of the leading edge cooling configuration. *Propulsion and Power Research*..**2(1)**, 1-9.

[3] Akçayoglu, A., Nazli, C. (2016). Thermal enhancement of triangular fins based on spanwise distance of vortex generators. *Proceedings of the Institution of Mechanical Engineers, Part C: Journal of Mechanical Engineering Science*, **231(13),** 2554-2566.

[4] Wang, W., Gao, J., Xu, L., Shi, X. (2012). Flow and heat transfer characteristics in rotating two-pass channels cooled by superheated steam. *Chinese J. Aeronaut.***25(4),** 524-532.

[5] Chu, P., He, Y. L., Lei, Y. G., Tian, L. T., Li, R. (2009). Three-dimensional numerical study on fin-and-oval-tube heat exchanger with longitudinal vortex generators. *Applied Thermal Engineering*, **29(5–6)**, 859–876.

[6] Sahin, A. Z. (1988). Irreversibilities in various duct geometries with constant wall heat flux and laminar flow. Energy, **23(6)**, 165–473.

[7] Zhao, T. S. Liao, Q. (2002). Theoretical analysis of film condensation heat transfer inside vertical mini triangular channels. *International Journal of Heat and Mass Transfer*, **45(13)**, 2829–2842.

[8] Gupta, R., Geyer, P. E., Fletcher, D. F., Haynes, B. S. (2008). Thermohydraulic performance of a periodic trapezoidal channel with a triangular cross-section, *International Journal of Heat and Mass Transfer*. **51(11-12)**, 2925–2929.

[9] Leung, C. W., Chen, S., Wong, T. T., & Probert, S. D. (2000). Forced convection and pressure drop in a horizontal triangular-sectional duct with V-grooved (i.e. orthogonal to the mean flow) inner surfaces. *Applied Energy.* **66,** 199-211.

[10] Shah, R. K., London, A. L. 1978. Laminar Flow Forced Convection in Ducts.

[11] Zhang, L. (2007). Laminar flow and heat transfer in plate-fin triangular ducts in thermally developing entry region. *International Journal of Heat and Mass Transfer*. **50**, 1637–1640.

[12] Nasiruddin, M. H. Siddiqui, K. (2006). Heat transfer augmentation in a heat exchanger tube using a baffle, *International Journal of Heat and Fluid Flow*. **28**, 318–328.

[13] Sirovich, L., Karlsson, S. (1997). Turbulent drag reduction by passive mechanisms. *Nature*, **388**, 753–755.

[14] Ferrouillat, S., Tochon, P., Garnier, C., Peerhossaini, H. (2006). Intensification of heat-transfer and mixing in multifunctional heat exchangers by artificially generated streamwise vorticity. *Applied Thermal Engineering***. 26**, 1820–1829.

[15] Chang, S. W., Liou, T. M., & Lee, T. H. (2012). Thermal performance comparison between radially rotating ribbed parallelogram channels with and without dimples. *International Journal of Heat and Mass Transfer*, 5**5(13–14)**, 3541–3559.

[16] Jacobi, A. M., Shah, R. K. (1995). Heat transfer surface enhancement through the use of longitudinal vortices: A review of recent progress. *Experimental Thermal and Fluid Science*, **11(3)**, 295–309.

[17] Wang, W., Gao, J., Xu, L., Shi, X. (2012). Flow and heat transfer characteristics in rotating two-pass channels cooled by superheated steam. Chinese Journal of Aeronautics. *Nuclear Engineering and Design.***25(4)**, 524–532.

[18] Sohankar, A. (2007). Heat transfer augmentation in a rectangular channel with a vee-shaped vortex generator. *International Journal of Heat and Fluid Flow*. **28,** 306–317.

[19] Ahn, J., Choi, H., Lee, J. S. (2007). Large eddy simulation of flow and heat transfer in a rotating ribbed channel. *International Journal of Heat and Mass Transfer*, **50(25–26),** 4937–4947.

[20] Viswanathan, A. K., Tafti, D. K. (2006). Detached eddy simulation of turbulent flow and heat transfer in a two-pass internal cooling duct. *International Journal of Heat and Fluid Flow*, **27(1),** 1–20.

[21] Viswanathan, A.K.,Squires, K.D., Forsythe, J.R. (2008). Detached-eddy simulation around a forebody with rotary motion. *AIAA Journal.* **46(9),** 2191-2201.

[22] Dhanasekaran, T. S., Wang, T. (2013). Computational analysis of mist/air cooling in a two-pass rectangular rotating channel with 45-deg angled rib turbulators. *International Journal of Heat and Mass Transfer*. **61(1)**, 554–564.

[23] Promvonge, P., Changcharoen, W., Kwankaomeng, S., Thianpong, C. (2011). Numerical heat transfer study of turbulent square-duct flow through inline V-shaped discrete ribs. *International Communications in Heat and Mass Transfer*. **38(10),** 1392–1399.

[24] Xie, G., Zhang, W., Sunden, B. (2012). Computational analysis of the influences of guide ribs/vanes on enhanced heat transfer of a turbine blade tip-wall. *International Journal of Thermal Sciences*. **51(1),** 184–194.

[25] Xie, G., Liu, J., M. Ligrani, P., Sunden, B. (2014). Flow structure and heat transfer in a square passage with offset mid-truncated ribs. *International Journal of Heat and Mass Transfer*. **71,** 44–56.

[26] Amro, M., Weigand, B., Poser, R., & Schnieder, M. (2007). An experimental investigation of the heat transfer in a ribbed triangular cooling channel. *International Journal of Thermal Sciences*. **46(5)**, 491–500.

[27] Armellini, A., Casarsa, L., Mucignat, C. (2011). Flow field analysis inside a gas turbine trailing edge cooling channel under static and rotating conditions. *International Journal of Heat and Fluid Flow*. **32(6),** 1147–1159.

[28] Chang, S. W., Yang, T. L., Liou, T. M., Hong, G. F. (2009). Heat transfer of rotating rectangular duct with compound scaled roughness and V-ribs at high rotation numbers. *International Journal of Thermal Sciences*. **48(1),** 174–187.

[29] Chang, S. W., & Hu, Y. W. (2014). Endwall thermal performances of radially rotating rectangular channel with pin-fins on skewed rib lands. *International Journal of Heat and Mass Transfer*. **69,** 173–190.

[30] Chang, S. W., Liou, T. M., Lee, T. H. (2012). Thermal performance comparison between radially rotating ribbed parallelogram channels with and without dimples. *International Journal of Heat and Mass Transfer.* **55(13–14),** 3541–3559.

[31] Chang, S. W., Liou, T. M., Lee, T. H. (2012b). Thermal performance of developing flow in a radially rotating parallelogram channel with 45° ribs. *International Journal of Thermal Sciences.* **52(1),** 186–204.

[32] Choi, E. Y., Choi, Y. D., Lee, W. S., Chung, J. T., Kwak, J. S. (2013). Heat transfer augmentation using a rib-dimple compound cooling technique. *Applied Thermal Engineering*. **51(1–2),** 435–441.

[33] Chyu, M. K., Ding, H., Downs, J. P., & Soechting, F. O. (1998). Determination of local heat transfer coefficient based on bulk mean temperature using a transient liquid crystals technique. *Experimental Thermal and Fluid Science*. **18(2),** 142–149.

[34] Lengani, D., Simoni, D., Ubaldi, M., Zunino, P., & Bertini, F. (2011). Turbulent boundary layer separation control and loss evaluation of low profile vortex generators. *Experimental Thermal and Fluid Science*. **35(8),** 1505–1513.

[35] Gupta, A., SriHarsha, V., Prabhu, S. V., Vedula, R. P. (2008). Local heat transfer distribution in a square channel with 90° continuous, 90° saw tooth profiled and 60° broken ribs. *Experimental Thermal and Fluid Science.* **32(4),** 997–1010.

[36] Chang, S. W., Gao, J. Y. (2014). Heat transfer enhancement by skewed wavy sidewall for two-pass ribbed channels with different aspect ratios. *International Journal of Heat and Mass Transfer.* **73**, 217–230.

[37] Lawson, S. A., Thrift, A. A., Thole, K. A., Kohli, A. (2011). Heat transfer from multiple row arrays of low aspect ratio pin fins. *International Journal of Heat and Mass Transfer*. **54(17–18)**, 4099–4109.

[38] Lan, Y.-A., Chen, J. S., Yang, T. L., Chang, S. W., Liou, T.-M. (2009). Influence of channel aspect ratio on heat transfer in rotating rectangular ducts with skewed ribs at high rotation numbers. *International Journal of Heat and Mass Transfer,* **52(23–24),** 5309–5322.

[39] Liu, J., Gao, J., Gao, T., & Shi, X. (2013). Heat transfer characteristics in steam-cooled rectangular channels with two opposite rib-roughened walls. *Applied Thermal Engineering*. **50(1),** 104–111.

[40] Huisseune, H., Joen, C. T., Jaeger, P. De, Ameel, B., Schampheleire, S. De, Paepe, M. De. (2013). International Journal of Heat and Mass Transfer Performance enhancement of a louvered fin heat exchanger by using delta winglet vortex generators. *International Journal of Heat and Mass Transfer.* **56(1–2),** 475–487.

[41] Joardar, A., Jacobi, A. M. (2008). Heat transfer enhancement by winglet-type vortex generator arrays in compact plain-fin-and-tube heat exchangers. *International Journal of Refrigeration.* **31,** 87–97.

[42] Joardar, A., Jacobi, A. M. (2005). Impact of leading edge delta-wing vortex generators on the thermal performance of a flat tube, louvered-fin compact heat exchanger. *International Journal of Heat and Mass Transfer*. **48,** 1480–1493.

[43] Fiebig, M. (1988). Vortices , Generators And Heat Transfer, *Institution of Chemical Engineers*. **76(A),** 108-123.

[44] Sanders, P. A., & Thole, K. A. (2006). Effects of winglets to augment tube wall heat transfer in louvered fin heat exchangers. *International Journal of Heat and Mass Transfer.* **49,** 4058–4069.

[45] Akcayoglu, A. (2011). Flow past confined delta-wing type vortex generators. *Experimental Thermal and Fluid Science*. **35(1),** 112–120.

[46] Torii, K., Kwak, K. M., Nishino, K. (2002). Heat transfer enhancement accompanying pressure-loss reduction with winglet-type vortex generators for fin-tube heat exchangers. *International Journal of Heat and Mass Transfer.* **45,** 3795–3801.

[47] Allison, C. B., Dally, B. B. (2007). Effect of a delta-winglet vortex pair on the performance of a tube – fin heat exchanger. *International Journal of Heat and Mass Transfer*. **50,** 5065–5072.

[48] Kim, E., & Yang, J. S. (2002). An experimental study of heat transfer characteristics of a pair of longitudinal vortices using color capturing technique. *International Journal of Heat and Mass Transfer***. 45,** 3349–3356.

[49] Potter, M. 2009. Fluid Mechanics DeMystiFied. 1st Edition.

[50] Fay, A. J., Sonwalkar, N. 1996. A Fluid Mechanics Hypercourse.1st Edition.

[51] Vorticity. Univercity of Leeds in school of Mathematics. http://www1.maths.leeds.ac.uk/~kersale/2620/Notes/chapter_3.pdf. 15. 07. 2015.

[52] H. Poincare, H. (1890). Sur le probleme des trois corps et les equations de la dynarnique, *Acta Math*. **13,** 1-270.

[53] ANSYS Fluent Help. 2013.

[54] ANSYS FLUENT Theory Guide. 2011. 724–746.

[55] Yakhot, V., Smith, L. M. (1992). The Renormalization Group, The ε-Expansion and Derivation Of Turbulence Models. *Journal Of Scientific Computing*. **7(1),** 35-61.

[56] Yakhot, V., Orszag, S. A. (1986). Renormalization group analysis of turbulence. I. Basic theory. *Journal of Scientific Computing*. **1(1),** 3–51.

[57] Jayatilleke, C. L. V. (1969). The influence of Prandtl number and surface roughness on the resistance of the laminar sublayer to momentum and heat transfer. *Prog. Heat Mass Transfer*. 1, 193-198.

[58] Vasudevan, R., Eswaran, W., & Biswas, G. (2000). Winglet-Typ E Vortex Generators for Plate-Fin Heat Exchangers Using Triangular Fins. *Numerical Heat Transfer*. **58(A),** 533–555.

[59] Akcayoglu, A., Nazli, C. (2018). A Comprehensive Numerical Study on Thermohydraulic Performance of Fluid Flow in Triangular Ducts with Delta-Winglet Vortex Generators. *Heat Transfer Engineering*. **39(2),** 107-119.

PUBLICATIONS

Refereed International Journal Publications

[1] AKÇAYOĞLU AZİZE, ÖZGÜN CENAP, NAZLI CELAL, YILMAZ FUAT, PINARBAŞI ALİ (2014). Optimum Distance Between Vortex Generators Used in Modern Thermal Systems. European Scientific Journal

[2] AKÇAYOĞLU AZİZE, CEBECİ HALİL, NAZLI CELAL (2014). Thermo-hydraulic Performance Evaluation of Inclined Vortex Generators. Advanced Materials Research

[2] AKÇAYOĞLU AZİZE, NAZLI CELAL (2017). Thermal enhancement of triangular fins based on spanwise distance of vortex generators. Proceedings of the Institution of Mechanical Engineers, Part C: Journal of Mechanical Engineering Science

[4] AKÇAYOĞLU AZİZE, NAZLI CELAL (2018). A Comprehensive Numerical Study on Thermo-hydraulic Performance of Fluid Flow in Triangular Ducts with Delta-winglet Vortex Generators. Heat Transfer Engineering

International Conference Presentations with Proceedings

[1] AKÇAYOĞLU AZİZE, NAZLI CELAL, YILMAZ FUAT (2015). Gas Turbine Blade Leading Edge Cooling Effectiveness Based On the Distance of Turbulence Promoters. 1st International Conference on Engineering and Natural Sciences.

[2] NAZLI CELAL, AKÇAYOĞLU AZİZE, YILMAZ FUAT (2019). Computational Study of Vortex Generators on Gas Turbine Blade Internal Cooling Channel Using Efficient Heat Transfer Surfaces. 2nd International Conference on Life and Engineering Sciences.